Phase-Field Modeling for Self-Healing of Mineral-Based Materials

M.Sc. Sha Yang

Von dem Fachbereich für
Bau- und Umweltingenieurwissenschaften
der Technischen Universität Darmstadt
zur Erlangung des akademischen Grades eines
Doktor- Ingenieur (Dr.-Ing.)
genehmigte Dissertation

Referent: Prof.Dr.ir. Eddie Koenders

Korreferent: Prof.Dr. Tony Jefferson

Darmstadt 2021

Yang, Sha: Phase-Field Modeling for Self-Healing of Mineral-Based Materials

Darmstadt, Technische Universität Darmstadt

Jahr der Veröffentlichung der Dissertation auf TUprints: 2022

Tag der mündlichen Prüfung: 17.12.2021

Acknowledgements

My PhD period at the institute of construction and building materials at the TU Darmstadt has come to an end. I am very happy that I chose this challenging journey, from which I have learned a lot. When I look back on the years I feel very enriched, and I am especially grateful to those who accompanied me and helped me along the way.

First of all, a special thanks to my supervisor, Professor Eddie Koenders. His thorough approach, profound knowledge and innovative thinking has served me well throughout my academic life. His patience, support and encouragement helped me to overcome one obstacle after the other. I also like to thank Professor Yuan of Tongji University for his valuable guidance. He was always very kind to answer my research questions and gave me valuable advices. Moreover, I would like to thank my colleagues Dr. Antonio Caggiano and Dr. Neven Ukrainczyk. They have given me many valuable comments and great support throughout my research. They have taught me how to think/write critical and logical, and how to be an independent researcher.

I would also like to give special thanks to my dear office colleague, Kira Weise, for sharing these wonderful years with me. I would like to thank my dear Aysen Cevik for always caring for me, looking after me and supporting me along the way. And to my dear colleagues, Dr. Christoph Mankel, Adrian Zimmermann, Shifan Zhang, Conrad Ballschmiede, Felix Berger, Maximilian Löher, Mona Nazari Sam and Oliver Vogt, for their care and support. It has been a privilege to work with so many outstanding researchers. A special thanks to Yangyiwei Yang for his generous academic help. Every meeting and conversation with him was inspiring and helpful. Very special thanks to Dr. Ingo Rüter for his continuous encouragement and guidance.

I would also like to express my sincere thanks to my best friend Meiling Shi who has accompanied me for more than ten years. My deepest gratitude will be dedicated to my relatives in my home town for their endless and unconditional love and support. In particular, I would like to dedicate my deepest gratitude to my dear parents. May they always have a long and healthy life. My husband, Dr. Christian Adams, thank you for letting me become a better person. My dear Adams family, who made me feel at home in Germany.

Abstract

Concrete is the most widely used building material in the world. The low raw materials cost, its high compressive strength and the simplicity of the production process makes it an enormous attractive and easy to apply material for the construction and building sector. However, when applied, concrete suffers from cracks, which are inevitable and are the result of various environmental and loading impacts such as traffic load, freeze-thaw cycles, but it also depends on the construction quality. These cracks provide harmful elements such as chloride, carbon dioxide or sulphur ions a pathway, which may induce steel corrosion of reinforced concrete structures. It is a mechanism that will seriously threaten the service life of a concrete structure, while causing significant maintenance costs. Mitigating this phenomenon has led to a worldwide development on self-healing methods for crack closure.

In the last few years, research efforts on self-healing methods have mainly concentrated on experimental work, where only a limited number of numerical models have been reported in literature. These models treat the boundaries, i.e. interfaces, between different the surfaces of components with a zero thickness. In fact, such interface describes the kinetics of a phase transformation from a non-equilibrium to an equilibrium state. This problem requires the diffusion equations to be solved at the interface under moving boundary conditions, which, although feasible for the evolution of simple geometries, becomes rather impossible for higher-dimensional systems and/or complicated interfaces.

For a more accurate description of the above problem, this PhD study presents a novel approach for self-healing of cementitious materials by means of a phase-field (PF) method. Unlike the traditional sharp interface models, a PF method provides a convenient way to numerically deal with free moving boundaries, where the interface is implicitly expressed as a time- and space-dependent function, representing the phase state, and is defined over the entire domain.

In this work, the diffusion-controlled isotropic dissolution of minerals is first investigated from a mesoscale phase transition point of view. Based on earlier formulations by Kim and co-workers [1], an expression of interface mobility under diffusion-controlled conditions is proposed. Using sodium chloride dissolution as an example, the results of their PF method are compared with that of analytical models and experiments, while extending the application of a PF method to the field of mineral dissolution. Based on this, the evolution of a carbonation front, which separates the dissolution zone from the carbonation fraction, is modelled on a thermodynamic basis, while mimicking the self-healing carbonation reaction in cementitious materials. Physical-chemical aspects are used to construct the free energy functions for incorporating dissolution and precipitation systems. Moreover, the dissolution model determines the local concentration fields of the active species in the PF. The model parameters were experimentally calibrated on a single mineral, i.e. the carbonation of calcium hydroxide. As a novel feature, the evolution of multiple interfaces is investigated and demonstrated by an experimental case of self-healing with

calcium hydroxide carbonation. Good qualitative agreement was achieved between the model results and the experimental data and the evolution of the crack morphology was demonstrated. This PhD study showed the potential of a PF method as a predictive tool to estimate self-healing in cementitious materials.

Zusammenfassung

Beton ist das weltweit am häufigsten verwendete Baumaterial. Die niedrigen Rohstoffkosten, seine hohe Druckfestigkeit und die Einfachheit des Herstellungsprozesses machen ihn zu einem äußerst attraktiven und leicht zu verarbeitenden Material für den Bau- und Gebäudesektor. Der Beton reißt im Laufe der Nutzungsdauer, was unvermeidlich ist und auf verschiedene Umwelteinflüsse und Belastungen wie Verkehrsbelastung, Frost-Tau-Zyklen, aber auch auf die Betonqualität zurückzuführen ist. Diese Risse bieten Substanzen wie Chloridionen, Kohlenstoffdioxid oder Schwefelionen einen Weg, bei Stahlbetonkonstruktionen Korrosion hervorzurufen. Durch diese Mechanismen wird die Lebensdauer einer Betonstruktur ernsthaft gefährdet und verursacht gleichzeitig erhebliche Instandhaltungskosten. Daher werden Selbstheilungsmethoden zum Schließen von Rissen in Beton entwickelt.

In den letzten Jahren haben sich die Forschungsarbeiten zu Selbstheilungsmethoden hauptsächlich auf experimentelle Arbeiten konzentriert, während in der Literatur nur wenige numerische Modelle beschrieben werden. Diese Modelle setzen die Dicke von Rändern oder Grenzflächen zwischen verschiedenen Oberflächen zu Null. Eine solche Grenzfläche beschreibt die Kinetik einer Phasenumwandlung von einem Nicht-Gleichgewichtszustand in einen Gleichgewichtszustand. Dieses Problem erfordert, dass die Diffusionsgleichung an den Grenzflächen unter beweglichen Randbedingungen gelöst werden muss, was zwar für die Entwicklung einfacher Geometrien machbar ist, aber für höherdimensionale Systeme oder kompliziert geformte Grenzflächen nicht zielführend ist.

Für eine genauere Beschreibung des oben genannten Problems wird in dieser Dissertation ein neuartiger Ansatz für die Selbstheilung von zementbasierten Materialien mithilfe der Phasenfeldmethode (PF-Methode) vorgestellt. Im Gegensatz zu den traditionellen scharfen Grenzflächenmodellen bietet die PF-Methode eine bequeme Möglichkeit, mit frei beweglichen Grenzflächen endlicher Dicke numerisch umzugehen. Hierbei wird die Grenzfläche implizit als zeit- und raumabhängige Funktion ausgedrückt, die den Phasenzustand darstellt und über dem gesamten Berechnungsgebiet definiert ist.

In dieser Arbeit wird die diffusionskontrollierte isotrope Auflösung von Mineralien zunächst unter dem Gesichtspunkt des mesoskaligen Phasenübergangs untersucht. Auf der Grundlage früherer Formulierungen von Kim et al. [1] wird die Grenzflächenmobilität unter diffusionskontrollierten Bedingungen hergeleitet. Am Beispiel der Solvatation von Natriumchlorid in Wasser werden zunächst die Ergebnisse der PF-Methode mit denen von analytischen Modellen und Experimenten verglichen, wobei die PF-Methode zur Auflösung von Mineralien angewendet wird. Anschließend wird die PF-Methode zur thermodynamischen Simulation der Präzipitation von mineralischen Substanzen verwendet. Es zeigt sich, dass die Karbonatisierungsfront die Auflösungszone und den Karbonatisierungsfortschritt unterscheidet. Physikalisch-chemische Aspekte werden genutzt, um die Funktionen der freien Energie für die Auflösungs- und Ausfällungssysteme zu konstru-

ieren. Darüber hinaus bestimmt das Solvatationsmodell die lokalen Konzentrationsfelder der aktiven Bestandteile im Phasenfeldmodell. Die Modellparameter werden experimentell anhand der Karbonatisierung des Minerals Calciumhydroxid ermittelt. Neu ist, dass die Entwicklung mehrerer Grenzflächen beschrieben und durch experimentelle Untersuchungen validiert werden kann. Hierbei wird die Selbstheilung durch die Karbonatisierung von Kalziumhydroxid betrachtet. Die Modellergebnisse und die experimentellen Daten stimmen gut überein. Außerdem wird die Entwicklung der Rissmorphologie nachgewiesen. Diese Dissertation zeigt das Potenzial der PF-Methode als Vorhersageinstrument zur Abschätzung der Selbstheilung in zementbasierten Materialien.

Contents

Index of Abbreviations and Symbols

Abbreviation	Full name and/or chemical formula
PF	phase field
OP	order parameter
FEM	finite element method
FGM	fixed grid method
VSSM	variable space-step method
VTSM	variable time-step method
VGM	variable grid method
VTSSM	variable time- and space-step method
EDS	energy-dispersive X-ray spectroscopy
ESEM	environmental scanning electron microscopy
GJ	gigajoule
SCA	smeared-crack approach
DCA	discrete crack approach
$Ca(OH)_2$	calcium hydroxide, portlandit
$CaCO_3$	calcium carbonate
Ca^{2+}	calcium ion
CO_3^{2-}	carbonate ion
CO_2	carbon dioxide
H_2O	water

Symbol	Description	Unit
c	solute concentration	mol/m^3
c_s	saturation concentrationc	mol/m^3
c_{min}	minimum supersaturation concentration	mol/m^3
c_{max}	ultimate supersaturation concentration	mol/m^3
ϕ	order parameter	-
A	curvature of the free energy density function	J/m^3
L	interface mobility	m^3/(Js)
ω	height of the double well potential	J/m^3
κ	gradient energy coefficient	J/m
D	diffusion coefficient	m^2/s
f	local free energy	J/m^3
ΔG	gibbs free energy	J/m^3
ΔG^a	activation energy	J/m^3
$\mathscr{L}$	total free energy	J/m^3
σ	interfacial energy	J/m^3
t	time	s
R	gas constant	J/(Kmol)
T	ambient temperature	kelvin
l_o	initial thickness of the diffuse interface	m

- The units of the symbols are given according to the International System of Units (SI).
- An unspecified unit is indicated by "-".

1 Introduction

1.1 Research background

Concrete is the most used man-made construction material of today and is used in massive quantities in countless infrastructure applications around the world. More than 12 billion tons of concrete are used in global construction each year [2]. Once applied, it is subjected to a combination of mechanical loads and environmental loads (e.g. freezing and thawing [3]), causing volumetric instabilities (e.g. creep and shrinkage [4]), which may lead to bigger and smaller cracks. Although smaller cracks, micro-cracks, do not directly cause structural failure, they may influence the rate of deterioration of a concrete structure.

Maintenance of buildings and infrastructures is a worldwide problem, causing every year significant human, financial and resource investments. In the United States, the annual economic impact associated with concrete structures undergoing inspection, repair, and/or replacement is estimated at $18-21 billion [5]. The maintenance cost for bridges only amounts $5.2 billion [6]. The indirect loss of time and productivity of the general public due to delays and disruptions caused by maintenance activities is estimated to be more than 10 times the direct cost. In Europe more than half of the annual construction budget is spent on the maintenance and repair [7]. In China, the total cost from the maintenance of roads and bridges due to concrete and rebar corrosion is more than $9.65 billion, equivalent to 4.0% of the total industry investments [8].

Maintenance of concrete structures, using cement-based repair materials, may also have a significant impact on the environment, as the cement production is energy-intensive. The production of 1 tonne (t) of cement requires about 3.2 gigajoule (GJ) to 6.3 GJ of energy and 1.7 t of raw materials (mainly limestone) [9]. Due to the enormous amounts cement produced annually, the share to the world's total carbon dioxide emission is up to 7% [10]. It is expected that, with the current growth of the economy, population, and the current service life expectation of concrete structures, the annual cement production will increase from about 3.3 billion tonnes (bt) now to 4.8 bt in 2030 [11]. The resulting ecological degradation will be significant.

Confronted with this, there is an urgent need in both academia and industry to find innovative solutions for enhancing the long-term performance of concrete structures. Over the past few decades, concrete has shown to have the intrinsic ability to heal the crack less than 150 µm in width [12]. Inspired by nature, various self-healing mechanisms have been developed for cracks with widths larger than 300 µm [13]. According to the definition of RILEM TC-221-SHC [14], the self-healing mechanicm of cement-based materials can be divided into two categories: autogenous and autonomous self-healing. The autogenous self-healing process only involves the remaining reactivity of the original components in the material, regardless of the effect of other additives. These original components may undergo chemical reactions under appropriate environmental

conditions while promoting crack healing. Autonomous self-healing processes are always depending on aid of healing additives, such as micro-capsules containing healing agents or bacterial spores.

So far, in self-healing developments experiment-based solutions have received a lot of attention, while optimizations based on numerical simulations were mostly disregarded. The limited number of numerical methods published in the literature are mainly used to simulate: (1) crack healing due to chemical reactions driven by carbonation, hydration and precipitation accompanied by transport effects; (2) continuous damage and mechanical strength recovery of structures, which usually follow the Smeared-Crack Approach (SCA) and the Discrete Crack Approach (DCA). In these models, the solid-liquid interface is usually assumed to be regular sharp or directly simplified to one-dimension, while quantifying only the healing efficiency. While the ion diffusion and the chemical reactions in solution are simulated, the microscopic morphological variations of cracks due to a soluble mineral dissolution and precipitation mechanism are completely ignored. However, changes in crack morphology directly affect the concentration distribution of aqueous substances in solution, which in turn, may act on the chemical reaction and mechanical effect at the interface.

Therefore, a novel and reliable numerical model is needed that combines these defects. Moreover, this numerical model should be able to make reasonable predictions of autogenous crack healing while providing excellent solutions for enhancing the durability and structural safety of cementitious materials. A Phase-Field (PF) method, emerged in recent years, turned out to be a powerful tool for handling mobile interfaces induced by phase transitions, and are widely used in solidification problems [15]. The advantage of a PF method over other competitive numerical methods lies in its ability to capture interface motions without introducing any additional special techniques and/or remeshing strategy. This provides a powerful and innovative approach to study the microstructural migration caused by the phase transition during a self-healing process.

1.2 Research objectives

The main objective of this research is to develop a numerical model using a PF approach for self-healing of cementitious materials based on the dissolution and precipitation mechanism from a phase transformation perspective. For this, the following three key aspects are addressed, which are considered to be crucial to understand and design a successful PF model for self-healing of cementitious materials. Firstly, understand and verify the feasibility of the PF method for the moving boundary problem of mineral dissolution. From an experimental point of view, the dissolution reaction is the first step in activating the self-healing mechanism. From a modeling point of view, this sequence helps to better understand and disentangle the complex self-healing mechanism based on nonequilibrium thermodynamics. Secondly, simulate the healing behavior of the single component minerals based on the physical parameters provided by experimental results, while focusing on the interface evolution during phase transformation. An innovative multi-phase multi-interfaces PF model for dissolution and precipitation should be based on the PF dissolution model validated in the first step. Finally, practical examples of cementitious materials are numerically implemented and analysed. In this thesis, these three key issues are taken as research questions and addressed by the numerical modeling techniques using a finite element method (FEM) platform. The main objectives are listed as follows:

- Comparison of a classical binary PF model with an analytical model for a general diffusion-controlled dissolution process and validation with experimental results for a congruent dissolu-

tion case.

- Development of a multi-phase PF model for precipitation/dissolution based self-healing. Prediction of healing kinetics under multiple factors.
- Implementation of carbonation experiments of calcium hydroxide. Experimental quantification of the amount of reaction products formed in cracks as a function of time. Analysing the boundary evolution and investigation of kinetic parameters of the multi-phase PF model.
- Simulation of the self-healing of actual irregular shaped cracks of cementitious materials and comparison with experimental results.

1.3 Research scope

The scope of this research comprises the following:

- The present study focuses only on the self-healing reaction based on the dissolution/precipitation mechanism.
- In the study of the carbonation reaction, only the end product, i.e. calcium carbonate ($CaCO_3$), is considered without other intermediate substances.
- When applying the PF model to the cementitious materials, the diffusion and precipitation of all aqueous species are represented by a single ionic concentration. The self-healing product phase does not distinguish between calcium–silicate–hydrates (C–S–H) and calcium hydroxide ($Ca(OH)_2$)) or other secondary hydration products.

1.4 Outline

This dissertation is composed as a cumulative one, which includes 4 chapters (Figure 1.1). Chapter 1 gives a brief introduction of the research background, objectives and corresponding scopes. Chapter 2 provides a review of most relevant fundamentals, self-healing mechanisms and the underlying theory of PF methods. Chapter 3 includes the three-following peer-reviewed publications:

publication 1
title: A Review on Cementitious Self-Healing and the Potential of Phase-Field Methods for Modeling Crack-Closing and Fracture Recovery [16]
journal: Materials, MDPI

publication 2
title: Numerical Phase-Field Model Validation for Dissolution of Minerals [17]
journal: Applied Sciences, MDPI

publication 3
title: A Phase-Field Approach for Portlandite Carbonation and Application to Self-Healing Cementitious Materials [18]
journal: Materials and Structures, Springer

Finally, in chapter 4 the conclusions and outlook of this thesis are reported.

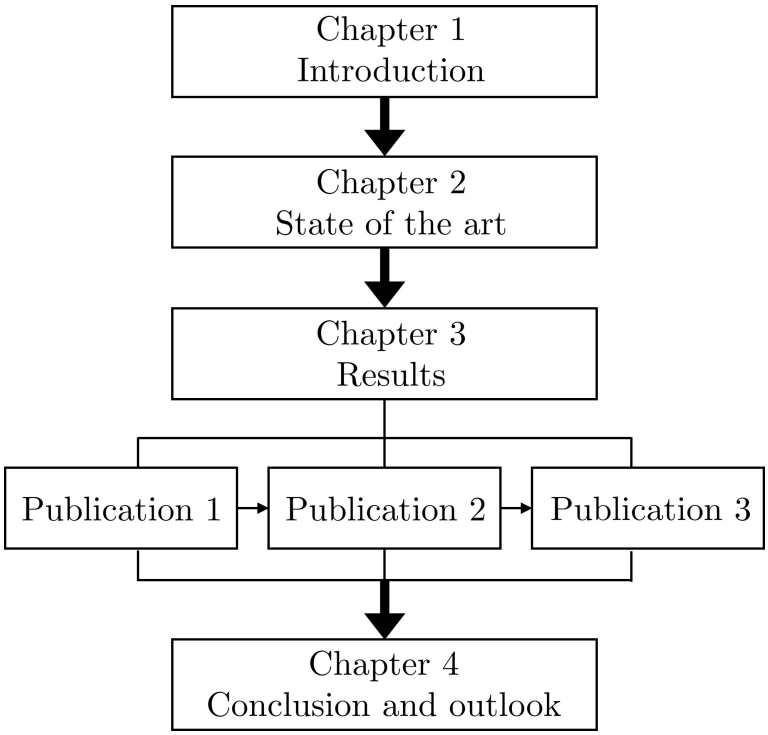

Figure 1.1. Outline of this thesis.

2 State of the art

2.1 Fundamental

2.1.1 Diffusion

Diffusion is a physical process in which molecules of a substance migrate from high to low concentration areas until they are evenly distributed [19]. Diffusion can take place in gases, liquids, or solids [19]. The driving force of diffusion are chemical potential, concentration and/or stress gradient. In 1855, Adolf Fick [20] developed the first law of diffusion, which is based on the analogy to heat conduction. In one-dimension x, the flux J of diffusing substances is proportional to the concentration gradient $\partial c/\partial x$

$$J = -D\frac{\partial c}{\partial x}, \tag{2.1}$$

where, D is the diffusion coefficient; the negative sign indicates the direction of diffusion from high to low concentration areas.

A combination of Eq.(2.1) with the conservation equation yields Fick's second law. It describes the variation of concentration with time t

$$\frac{\partial c(x,t)}{\partial t} = -\frac{\partial J}{\partial x} = D\frac{\partial^2 c(x,t)}{\partial x^2} \tag{2.2}$$

For the case of diffusion in two dimensions or more and D is a constant, Fick's second law is expressed as

$$\frac{\partial c(x,t)}{\partial t} = D\nabla^2 c(x,t) \tag{2.3}$$

where, ∇ is the vector differential operator.

2.1.2 Dissolution

Dissolution is the process by which a solute (solid and/or gas) is uniformly dispersed in a solution (liquid). The dissolution of solid particles in a liquid involves two main steps: 1) the detachment of molecule or ion from the surface of the solid to form a hydrated molecule with the liquid (the reaction-controlled dissolution), and 2) the mass transfer from the solid-liquid interface to the bulk solution (the diffusion-controlled dissolution) [21]. The equation for the diffusion-controlled dissolution is already proposed by Noyes and Whitney [22] in 1897, where the dissolution rate R_d is proportional to the difference between the solubility and the bulk concentration

$$R_\mathrm{d} = \kappa_\mathrm{d}(c_\mathrm{s} - c_\mathrm{b}), \tag{2.4}$$

where, c_s is the solubility; c_b is the bulk solution concentration, and κ_d is the dissolution rate constant, which is related to the transport property of the solute.

The equation for the reaction-controlled dissolution rate R_r is [23]

$$R_r = \kappa_s \left(1 - \frac{c}{c_{eq}}\right), \tag{2.5}$$

where, κ_s is the effective transport coefficient and c_{eq} is the equilibrium concentration.

2.1.3 Precipitation

Precipitation is the process of converting dissolved substances from a supersaturated solution into insoluble solids [24]. When the concentration of the dissolved solute in the solution is higher than the solubility, the solution is supersaturated. At this state, the solute particles agglomerate with each other to form insoluble solids, which then precipitate out of the solution. When the solute concentration in the solution decreases until the solution equilibrium is established, i.e., the migration rate of substances between the solid and solution phases is equal to each other, the solution reaches a saturation state. The precipitation process can be divided into the following steps: nucleation, growth, ripening, and recrystallization [25]. The equilibrium constant for the dissolution and precipitation of a slightly soluble ionic solid is called the solubility product K_{sp}. For a heterogeneous equilibrium involving the solid A_mB_n and its ions mA^{n+} and nB^{m-}

$$A_mB_n(s) \rightleftharpoons mA^{n+}(aq) + nB^{m-}(aq), \tag{2.6}$$

where, “s” and “aq” refer to species in the solid and aqueous states, respectively.

The solubility product is expressed as

$$K_{sp} = \left\{A^{n+}\right\}^m \left\{B^{m-}\right\}^n, \tag{2.7}$$

where $\left\{A^{n+}\right\}$ and $\left\{B^{m-}\right\}$ are the ionic activities; the right-hand side of Eq.(2.7) is referred to as the ion activity product (IAP), which can be used to estimate the saturation of a solution for a particular substance by estimating the saturation index (SI)

$$\mathrm{SI} = \log_{10}\left(\frac{\mathrm{IAP}}{K_{sp}}\right). \tag{2.8}$$

If SI<1, the solution is unsaturated and the dissolution process continues; if SI>1, the solution is supersaturated and the precipitation begins; if SI=1, the solution is in the equilibrium state.

Thermodynamically, the precipitation is accompanied by changes in the solute concentration and the free energy. Lamer and Dinegar [26] used sulfur nucleation as an example to illustrate the change in the solute concentration from soluble monomer particles to colloidal clusters (Figure 2.1 (a)). Firstly, soluble monomers are gradually formed in the solution and their concentration increases (Stage I). Soluble monomers nucleate from the solution when their concentration is higher than the critical supersaturation level c_{min} (the minimum supersaturation for the nucleation). The nucleation phase ends when the concentration of soluble monomers reaches the supersaturation level c_{max} (ultimate supersaturation) (Stage II). When the supersaturation concentration is lower than c_{min} but higher than the saturation concentration c_s (solubility of soluble monomers), the

stable nuclei in solution continue to grow by diffusion. Cluster growth ends when the concentration of monomeric species drops to the solubility level of the bulk solid (Stage III).

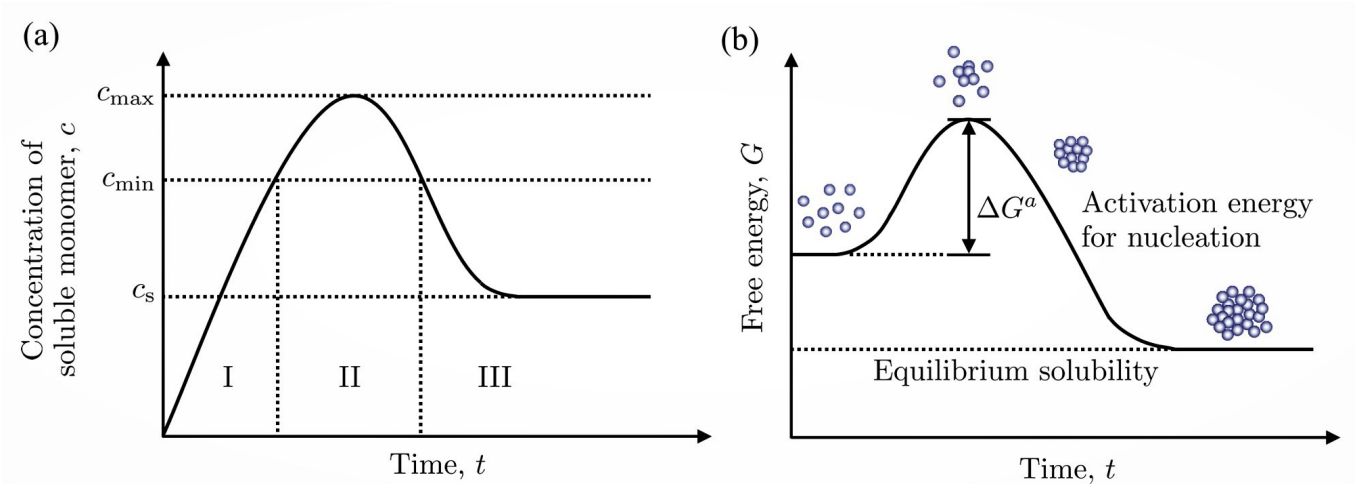

Figure 2.1. Schematic illustration of variation in solute concentration and free energy during precipitation. (a) The concentration of molecules before and after nucleation as a function of time. Reproduced with permission from [26]. Copyright 1950 American Chemical Society. (b) The variation of the free energy as a function of particle size. Reproduced with permission from [27]. Copyright 2013 Elsevier.

Patel and Anderson [27] elucidated the variation of free energy of the precipitate nucleation (Figure 2.1 (b)). Initial nucleation requires overcoming the activation energy ΔG^a and then generating a critical nuclei. The critical nuclei gradually grow in the region of the metastable supersaturated state, forming larger particles. A solution in a supersaturated state is thermodynamically unstable, thus it tends to reach a steady state by lowering the free energy of through precipitation. Eventually, the nuclei size reaches its maximum at the equilibrium solubility and particles precipitate out of the solution.

2.2 Self-healing in cementitious materials

Cementitious materials are known as brittle materials with a low tensile strength and fracture toughness. Microcracks occur inevitably during the construction and service life period. If microcracks are not timely repaired, cracking will exacerbate the structural damage, thus affecting the durability of the structure. Over the past decades, tremendous efforts have been made to develop self-healing techniques for various types of cementitious materials from both experimental and simulation perspectives. This chapter gives an overview on the various mechanisms of self-healing (in Section 2.2.1), followed by a synthesis of existing analytical and numerical simulation methods (in Section 2.2.2).

2.2.1 Self-healing mechanisms

The RILEM Committee TC-221 SHC and the Technical Committee TC-075B of the Japan Concrete Institute (JCI) have classified self-healing mechanisms into autogenous and autonomous [14, 28].

Table 2.1. A taxonomy for research in self-healing mechanisms

Category	Crack width	Mechanisms		Reference
Autogenous	100–150 µm	Further hydration of unhydrated cement clinker		[29–33]
		Carbonation of portlandite, precipitation of calcite		[29, 34–37]
		Recrystallization of portlandite leached from the bulk paste		[14, 31, 38–40]
Autonomous	≥300 µm	Mineral admixtures	Expansion term	[41, 42]
			Swelling term	[43–45]
			Crystalline term	[43, 46]
		Bacteria	Direct application	[47, 48]
			With encapsulation	[49–52]
		Adhesive agents	One-component	[53, 54]
			Multi-component	[55, 56]

The autogenous self-healing process involves only the efficacy of the original components in the material, regardless of the effects of other additives. These original components can react chemically under appropriate environmental conditions to foster crack healing. The autogenous healing is capable of repairing cracks up to a width of 100-150 µm [13]. In contrast, autonomous healing can heal cracks up to 300 µm [13, 47]. However, the autonomous self-healing process must be accomplished with the help of healing agents such as micro-capsules containing healing agents or bacterial spores. The classification of self-healing mechanisms and corresponding crack healing widths are summarized in Table 2.1. The principles of each self-healing mechanism are described in detail in Section 2.2.1.1 and 2.2.1.2.

2.2.1.1 Autogenous self-healing

Autogenous self-healing comprises of three main chemical reactions: a further hydration of the unhydrated cement clinker generating additional Calcium Silicate Hydrates ($\mathrm{C{-}S{-}Hs}$), precipitation of calcite, and recrystallization of portlandite. There are some secondary mechanisms, including volume expansion due to water absorption by the cement matrix and mechanical filling cracks caused by the accumulation of mineral debris in solution [14]. These mechanisms are not considered in this thesis.

(1) Further hydration of unhydrated cement clinker

For young concrete the further hydration of the unhydrated cementitious clinker is the main mechanism of self-healing [37]. Unhydrated cement clinker of cracked surfaces inside a cement

matrix begin to dissolve once they are in contact with water, where Ca^{2+} ions and silicates diffuse from the anhydrates [57]. When the concentration of the various ions in the solution reaches the equilibrium criteria for precipitation, further hydration products are formed in the crack solution [31]. As further hydration products form on the crack surface, the rate of further hydration slows down and the self-healing changes from a chemical reaction-controlled process to a diffusion-controlled one [32].

The strength of the hydration products formed by further hydration is similar to that of the primary $C-S-H$ gels, which may be effective in restoring the mechanical properties of the cementitious composite. The content of $Ca(OH)_2$ (CH) in the self-healing products is higher than that of the $C-S-Hs$ and differs significantly from the composition of hydration products in bulk cement paste [31]. In addition, the nucleation and growth of the hydration products formed at the crack surface also differ from those in the bulk cement paste.

There are two reasons for that: 1) The amount of water provided for further hydration at the crack surface is much more abundant than that in the bulk cement paste (w/c>0.3), which ensures that the cement clinker is fully hydrated, resulting in larger sized crystal-like products [40]. However, further hydration in the cracks will stop when the water in the cracks is completely absorbed due to the capillary effect of the concrete matrix; 2) the space provided for the nucleation and growth of hydration products at the crack surface is much larger than that in the hydrated cement paste [13]. Thus, the distribution of hydration products generated at the crack surface is more dispersed than that in the bulk cement matrix.

(2) Carbonation of portlandite, precipitation of calcite

Crystallization of calcium carbonate $CaCO_3$ is proved to be the main mechanism for autogenous self-healing [29, 34]. The chemical reaction process could be described as follows

$$\begin{cases} Ca(OH)_2(s) \xrightarrow{H_2O} Ca^{2+}(aq) + 2OH^-(aq), \\ CO_2(g \rightarrow aq) + H_2O \longrightarrow CO_3^{2-}(aq) + 2H^+(aq), \\ Ca^{2+}(aq) + CO_3^{2-}(aq) \longrightarrow CaCO_3(s), \end{cases} \tag{2.9}$$

where, “aq”, “g” and “s” refer to species in an aqueous, gaseous and solid state, respectively.

Initially when the cracks are filled with water, portlandite and unhydrated cement clinker dissolves, releasing Ca^{2+} ions. The Ca^{2+} ions transported from the cement matrix react with carbonate CO_3^{2-} ions from the atmospheric carbon dioxide dissolved in water and form $CaCO_3$ precipitates [40]. This stage is reaction controlled. Once an initial calcite layer on the crack surface has formed, the amount of Ca^{2+} ions supplied by the concrete matrix will reduce including a transition to a diffusion-controlled precipitation. Ca^{2+} ions from the cementitous matrix can only reach the crack surface by diffusion through the calcite layer to form the healing products.

The carbonation reaction is often limited by an insufficient supply of Ca^{2+} and CO_3^{2-} ions [29]. On the one hand this is due to the fact that a certain portion of the portlandite (the main source of Ca^{2+} ions) is used in the pozzolanic reaction for $C-S-Hs$ development [58]. On the other hand, that CO_3^{2-} ions are difficult to transport to the deeper crack regions. Thus $CaCO_3$ is often experimentally observed to form mainly at the surface near the crack openings, as the sufficiently high Ca^{2+} and CO_3^{2-} ions content in this area is available for the $CaCO_3$ precipitation [13, 58].

(3) Recrystallization of portlandite leached from the bulk paste

CH is quantitatively an important hydration product of Portland cement clinker, which is able to fill cracks by recrystallisation [59]. Solid particles of CH are first dissolved in the form of solute ions, which diffuse into the depths of cracks and then precipitate in a supersaturated state [60] according to

$$\mathrm{Ca(OH)_2\ (s)} \xrightarrow{\mathrm{H_2O}} \mathrm{Ca^{2+}\ (ion) + 2OH^-\ (ion)} \xrightarrow{\mathrm{H_2O}} \mathrm{Ca(OH)_2\ (s)}, \tag{2.10}$$

where, "ion" refers to species which are in an ionic state.

Compared to the autogenous self-healings mentioned above, CH recrystallization is less efficient, since the solubility of CH is 100 times higher than that of $CaCO_3$ polycrystals [61, 62]. In addition, solid CH in the cementitious matrix first dissolve in the unsaturated solution. However, Ca^{2+} ions are continuously consumed by the carbonation reaction, making it difficult for the CH recrystallization [59]. The diffusion rate of solute ions and degree of supersaturation of CH are important factors affecting its recrystallisation rate [63]. In addition, the results in [39, 59] showed that a number of CH was found as large, well-formed crystals in deep cracks with a very high moisture content, since carbonation was inhibited in this region, giving a suitable condition for CH recrystallization.

2.2.1.2 Autonomous self-healing

Due to the limited effectiveness of autogenous self-healing, many attempts have been made in concrete engineering to improve the crack healing performance by artificially adding additional ingredients (healing agents), either encapsulated or non-encapsulated. Healing agents are available in a variety of compositions such as minerals, bacteria, and polymers. The healing mechanism of each additive is described in detail below:

(1) Mineral Admixtures

Mineral admixtures filled in the cementitous materials can react with water when cracks appear so that the cracks are healed with reaction products [43]. According to the type of reaction, mineral admixtures can be divided into three categories: expansive, swelling and crystalline admixtures.

The expansive admixture works on the principle of using the increase in volume of the reaction products to fill the cracks [42, 58]. Commonly used are calcium sulfoaluminate (CSA) based expansive agents [64]. Due to the rapid hydration of CSA in 2 to 24 hours the dense product can heal the cracks in a short time [65–67]. Geomaterial-based additives consisting of silicon dioxide, sodium aluminum silicate hydroxide, and bentonite clay can heal cracks by swelling [43–45]. The main mineral component of crystalline admixture is tricalcium silicate (C_3S), which reacts with water producing $\mathrm{C-S-H}$ crystals [68, 69].

(2) Bacteria Admixtures

The main mechanism of bacteria based self-healing is that the bacteria themselves act as catalysts, converting precursor compounds into suitable filler materials. Bacteria containing calcium nutrient sources are added to cementitous materials at the time of mixing [70]. At this point, the bacteria are inactivated in the form of spores [71]. When cracks appear, water enters

the interior of the structure and activates the bacteria [72]. Through their metabolism, $CaCO_3$ deposits are produced to fill the cracks. So far, two types of bacterial metabolic pathways have been used to increase the crack healing potential of cementitous materials:

Metabolism of aerobic alkalophilic bacteria [71, 73]

Aerobic alkalophilic bacteria can convert calcium lactate $Ca(CH_3COO)_2$ into $CaCO_3$ precipitate, which is the direct ability of microbially enhanced crack healing

$$\mathrm{Ca(CH_3COO)_2(aq) + 4O_2(aq) \rightarrow CaCO_3(s) + 3CO_2(aq) + 3H_2O(aq).} \tag{2.11}$$

The indirect ability is manifested by the reaction of metabolically generated CO_2 molecules with $Ca(OH)_2$ minerals present in the cement matrix to produce additional $CaCO_3$ precipitates. Wiktor and Jonkers showed that this method can lead to complete healing of cracks up to 460 µm in width within 100 days [72]. A two-component biochemical self-healing agent consisting of a mixture of bacterial spores and calcium lactate, can promote the healing of cracks with a width of more than 900 µm [72]. However, the main disadvantage of the aerobic respiration pathway is that the healing capacity is limited by the amount of O_2, since metabolically active bacteria require large amounts of O_2. In the absence of O_2, the healing capacity is inhibited [73].

Urea hydrolysis [74, 75]

This pathway has a better self-healing property than that of the first one. Special bacteria like Bacillus cohnii, Sphaericus, Subtilis, Pasteurii, Megaterium, and Sporosarcina urea can convert urea to ammonium NH^{4+} and $CaCO_3$ in a highly alkaline environment [76]. Although microbial urea decomposition mechanisms can promote rapid healing of cracks, e.g. a 970 µm wide crack can heal in 8 weeks [77], the hydrolysis product NH^{4+} becomes NH_3 under alkaline conditions. During this conversion process the OH^- ions in the concrete are depleted and this leads to degradation of the concrete [47]. In addition both NH^{4+} and NH_3 are considered to be harmful to aquatic life [78]

$$\mathrm{CO(NH_2)_2(aq) + 2H_2O(aq) + Ca(NO_3)_2(aq) \rightarrow CaCO_3(s) + 2NH_4^+(ion) + 2NO_3^-(ion).} \tag{2.12}$$

It is worth noting that when applying these pathways, the spores or bacteria should be protected from the harsh concrete environment in order to maintain their activity [79]. When bacterial spores are added directly to cement mixtures, they survive for only 1-2 months [71]. In addition, the direct addition of organic biomineral precursor compounds can cause a significant reduction in the strength of cementitious materials. Therefore various encapsulation techniques for bacteria have been investigated, such as immobilizing them with microcapsules [52, 77] and porous expanded clay aggregates [80].

(3) Adhesive Agents

Compared to the two methods mentioned above, using adhesive agents is the most rapid one. Strength recovery rates of up to 75% were observed after 48 hours of crack healing [53]. The adhesive agents can be encapsulated in microcapsules [81], hollow fibers [82] or vessel networks [83]. Adhesive agents can be classified as one-component or multi-component. Commonly used one-component adhesive agents are polyurethane [53] and epoxy [54]. It is worth mentioning that epoxy resins can also be divided into one-component and two-component. One-component epoxy resins are generally latent epoxy resins, where a curing

agent or catalyst has been added to the epoxy resin. However, the two-component one is resin and curing agent are initially encapsulated separately. When cracks appear, the two components are released from the sealing device subsequently undergo a hardening reaction to heal the cracks.

In addition to two-component epoxy resins, a commonly used multi-component adhesive is methylmethacrylate (MMA) [55]. Yang et al. combined MMA with triethylborane (TEB, catalyst) and obtained positive self-healing results [81]. Dry et al. used a three-component MMA [84], i.e. cumine hydroperoxide and cobalt neodecanoate as catalysts to promote the polymerization and hardening of the MMA. Multi-component adhesives have higher stability than single-component adhesives, since they are activated in situ. However, due to the inability to control the ratio of multi components penetrating into the crack, one-component adhesives have proven to be more effective in repairing cracks [85].

2.2.2 Self-healing modeling

The existing numerical methods for self-healing can be divided into: (1) chemical-transport-based models and (2) fracture-based models. Table 2.2 summarizes the existing models and their techniques.

2.2.2.1 Chemical-transport-based model

The chemical-transport-based model focus mainly on the diffusion mechanisms of heat, moisture and aqueous species in the cementitious material, and the chemical thermodynamics and kinetics for precipitation of hydration, carbonation and/or hygro-electrochemical self-healing products. Cementitious materials are considered as the porous multiphase medium, with air and/or capillary pores in the solid matrix occupied by liquid and/or gaseous phases. At the macroscopic scale, the governing equations of these models are formulated based on the average conservation equations for mass (phases and chemical species) and enthalpy under the assumption of local thermo- and/or hygral equilibrium.

For the further hydration self-healing, Zhang et al. [86] proposed a model in which the unhydrated cement nuclei were randomly distributed in the cementitious composite matrix. The cracks were simulated by splitting (the crack go through the unhydrated cement particles) and dome-like (the crack go along the surface of unhydrated cement particles) methods. The efficiency of self-healing influenced by the volume fraction and the particle size distribution of unhydrated cement nuclei was calculated from the perspective of geometric probability theory. Huang and Ye [32] determined numerically the self-healing efficiency by using capsules containing water to promote further hydration of unhydrated cement particles. The volume of additional water in the fracture was calculated as a function of time based on the transport theory. The amount of hydration products was determined by a thermodynamic model coupled by the mass balance, the charge balance and the chemical equilibrium.

A several hygro-thermal-chemical models were developed. Di Luzio et al. [87, 88] proposed a SMM (Solidification-Microprestress-Microplane) model to simulate the healing effect of concrete under different humidities, thermal fields and hydration degrees. The modified model can also simulate the effect of cracks on the permeability and the evolution of mechanical properties of

concrete. On this basis, Ferrara [89] introduced a recovery degree to approximate the degree of the self-healing. In addition, the recovery of the load-bearing capacity of concrete with and without additives was simulated and compared with experimental data. Chitez and Jefferson [90] presented a coupled thermal-hygro-chemical model and used reactive water transport component to predict the movement of healing materials. Moreover, a hydro-chemo-mechanical model based on micro-mechanical observations was established by Hilloulin et al. [91]. Based on a diffusion-hydration model, the recovery of mechanical properties during self-healing was evaluated using a continuum damage model.

Table 2.2. A review of self-healing modeling.

Phenomena	Category	Technique	Reference
Chemical-transport	Autogenous	Splitting crack model	[86]
		Thermodynamic-diffusion model	[32]
		Hygro-thermal-chemical model	[87–90]
		Hydro-chemo-mechanical model	[91]
		Reaction-diffusion model	[92]
		Embedded finite element method	[93]
	Autonomous	Level set method	[94]
		Coupled transport-damage model	[95]
		Hybrid genetic algorithm	[96]
		Analytical model	[97]
Fracture	Autogenous	Micro-mechanical model	[98]
		Two phases micro-mechanical model	[99]
		Softening-healing with SDA	[100]
		Cohesive zone damage-healing model	[101]
		Discontinuity embedded model	[100]
		Lattice model	[102]
	Autonomous	Phenomenological model	[103]
		Continuous damage model	[104]
		Reversed cohesive constitutive model	[105]
		Discrete element method	[106]
		Cohesive surfaces technique	[107]
		LatConX system model	[108]
		Particle flow code (PFC2D)	[109]
	General	Thermodynamic constitutive model	[110–114]
		Coupled damage-plasticity model	[115]

For the carbonation self-healing, Aliko-Benítez et al. [92] proposes a reaction-diffusion model using Finite Element Method (FEM). The diffusion of aqueous species and the reaction rate calculated from the three main species Ca^{2+} ions, $CO_3{}^{2-}$ ions and $CaCO_3$ precipitates were taken into account.

For the same mechanism, Ranaivomanana and Benkemoun [93] discretized the transport-reaction partial differential equations for the fracture and porous matrix using the Embedded Finite Element Method (E-FEM).

In contrast to autogenous self-healing, only a few chemical-transport models have addressed autonomous self-healing. Zemskov et al. [94] presented a mathematical model of bacterial self-healing. The moving boundaries were tracked using a level set method. Freeman and Jefferson [95] proposed a model for the delivery of healing agents to damaged zones. By coupling a crack flow model with the mass balance equation, the continuum and discrete-crack flows were simulated. Suleiman and Nehdi [96] developed a hybrid genetic algorithm-artificial neural network model predict the self-healing efficiency of concrete under the influence of different factors, i.e. water-to-cement ratio (w/c), type and dosage of supplementary cementitious materials, and bio-healing materials. In addition to numerical models mentioned above, Zhu et al. [97] developed an analytical model to predict the microcapsule-based self-healing efficiency.

2.2.2.2 Fracture-based model

Few studies aimed at the healing mechanical properties of cementitious materials are available in the literature. A representative fracture model is a two phase micro-mechanical constitutive model developed by Davies and Jefferson [99]. A cohesive zone damage-healing model was presented by Abu Al-Rub and Alsheghri [101]. In this model, the classical continuum damage mechanics were extended to describe the healing evolution within the crack cohesive zone. Zhang and Zhuang [100] proposed a time-dependent softening-healing law for self-healing quasi-brittle materials and evaluated the reliability of the model using a strong discontinuity embedded approach.

The main idea of Remmers and Borst's [105] phenomenological model is that fracture healing is triggered by fluid pressure. The re-bonding of the crack surface was modelled by a reversed cohesive constitutive model. Zhou et al. [106] proposed a three-dimensional damage healing model for microencapsulated self-healing cementitious materials under compressive loading by using a discrete element method. This model can be used to simulate local healing effects, as well as stress concentration effects and local healing effects. Hazelwood et al. [108] developed a LatConX model to predict the long-term healing behaviour of concrete materials containing shape memory polymer tendons.

For general fracture self-healing problem, several thermodynamic-based micro-damage healing models have been made in the literature [110–114]. Additionally, Caggiano et al. [115] proposed a damage-plastic constitutive theory for zero-thickness interfaces. The model was based on the fracture-energy concept and included the time evolution of concrete porosity. In addition, some thermodynamic-based constitutive models and coupled damage-plasticity model can be applied to both autogenous- and autonomous self-healing mechanisms [110–115].

2.3 A moving boundary problem

2.3.1 Introduction

The moving boundary problem (MBP), also known as the Stefan problem, was studied in depth by J. Stefan [116, 117]. The MBP occurs in many physical and engineering processes, e.g. dissolution

[118], heat transfer involving phase transformation [119], cracks in solid mechanics [120] and metallurgy [121]. These problems are usually defined as a system of partial differential equations (PDEs) in a certain domain, however the boundary (interface) separating two phases is unknown and must be determined as an integral part of the solution. The location of the moving boundary (MB) is described by a function of time t and space x, controlled by the transport conditions.

To illustrate the MB problem in more detail, the evolution of the solid-liquid boundary due to thermal diffusion and latent heat exchange in a homogeneous medium will be illustrated below using a classical solid-liquid system as an example (as shown in Figure 2.2). The solid phase I and the liquid phase II are divided into region Ω_1 and Ω_2 by an interface I of approximately zero width. Melting or solidification caused by temperature changes leads to regional changes in each phase. Therefore the position and the morphology of the interface I change accordingly. The temperature μ at the interface is the phase change temperature. The moving boundary obeys the laws of mass conservation and energy conservation, which are Stefan's conditions [122].

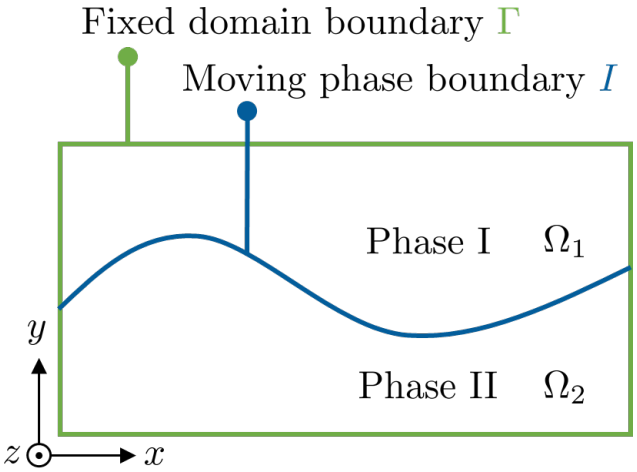

Figure 2.2. A two phases system with a MB. The domain Ω consists of phase I (Ω_1) and phase II (Ω_2). The contour bounds the overall domain (Γ), while the two phases are separated by a MB (I).

The temperature μ is governed by the heat conduction equation, which is expressed in the solid and liquid phases as follows

$$c_1\rho_1\frac{\partial\mu}{\partial t} = k_1\frac{\partial^2\mu}{\partial x^2}, \tag{2.13}$$

$$c_2\rho_2\frac{\partial\mu}{\partial t} = k_2\frac{\partial^2\mu}{\partial x^2}, \tag{2.14}$$

with the boundary condition

$$\mu(0,t) = \text{const}, \tag{2.15}$$

and the initial condition

$$\mu(x,0) = \text{const}, \tag{2.16}$$

where, k_1 and k_2 are the thermal conductivities, c_1 and c_2 are the specific heat capacities, ρ_1 and ρ_2 are the densities of solid and liquid phases, respectively.

The condition on the interface I is

$$\mu_1 = \mu_2, \tag{2.17}$$

where, μ_1 and μ_2 are the temperature of the solid and the liquid phases, respectively.

The Stefan conditions on the interface I are

$$\begin{cases} \lambda\rho_1 \frac{dI}{dt} = k_1 \frac{\partial \mu_1}{\partial x} - k_2 \frac{\partial \mu_2}{\partial x}, \\ I(0) = 0, \end{cases} \tag{2.18}$$

where, λ is the latent heat.

2.3.2 Numerical methods

For solving MBP, there are three main numerical methods. The first one is the fixed grid method (FGM) also called Eulerian method, where the grid is spatially fixed in Cartesian form. The MB is tracked by using a marker function or an auxiliary variable. Depending on the marker function, the FGMs can be divided into three categories, i.e., point, surface and volume marker methods. The point marker method is very effective in tracking interfaces with small perturbations, while producing numerical instability for complex migrations [123]. A commonly used surface marker method is the level set method [124], where the position of the MB is given as the zero-level set of an auxiliary field defined over the domain [125]. The volume marker method is often used for tracking of the internal region of the fluid. The interior of the fluid is discretized and each cell is assigned a volume fraction. The topologically changing fluid boundary is tracked through the changing volume [126].

In addition to the above-mentioned marker function, the most widely used auxiliary variable is the enthalpy function. The location of the interface is determined from the enthalpy function $H(T)$ where an energy jump occurs due to the phase transformation [127]. The heat transfer equation at the interface is expressed as

$$\frac{\partial H(T)}{\partial t} = K\nabla^2 T, \tag{2.19}$$

where $K = \lambda/(c\rho)$; T is the temperature; λ, c and ρ represent the thermal conductivity, the specific heat capacity and the density of the material, respectively.

The enthalpy as a function of temperature is written as [128]

$$H(T) = \begin{cases} cT, & T < T_1 & \text{solid phase} \\ cT + \frac{L(T-T_1)}{T_2-T_1}, & T_1 \le T \le T_2 & \text{interface region} \\ cT, & T > T_2 & \text{liquid phase} \end{cases} \tag{2.20}$$

where T_1 and T_2 are the temperatures at the lower and the higher ends of the interface region, respectively; L is the latent heat.

An outstanding advantage of the FGM is that its computational effort is low because the calculation is performed on a uniform and orthogonal fixed Cartesian grid.

The second method is the variable grid method (VGM) [129] also known as Lagrangian method, where the MB is located on a line of the grid nodes and the grid is scaled as the boundary moving.

It can also be subdivided into Variable Space-Step Method (VSSM), Variable Time-Step Method (VTSM), and Variable Time-Space-Step Method (VTSSM). A significant advantage of VGM is that the boundaries can be accurately calculated, because the MB coincide with a line of numerical nodes. However, the grid must be updated at each time step, and the computational effort is quite expensive. In addition, due to the shape of the moving interface and its trajectory are frequently compressed, it is possible to make the large deformation of the grid cells, which leads often to numerical errors.

The last approach is the hybrid method (HM) also called mixed Eulerian–Lagrangian method [130, 131] which employs properties of both fixed and deforming grids. Combining the advantages and disadvantages of the FGMs and VGMs, the calculation of this method is performed on a fixed Cartesian grid, which effectively avoids the problem of computationally heavy grid redistribution. The irregularly shaped interface is tracked on the fixed grid and represented by a marker function. The shape information of the interface is obtained by connecting the marker functions, e.g., for the point marker function, the node position and curvature are obtained. The new interface is obtained by the Lagrangian translation of updated marker functions.

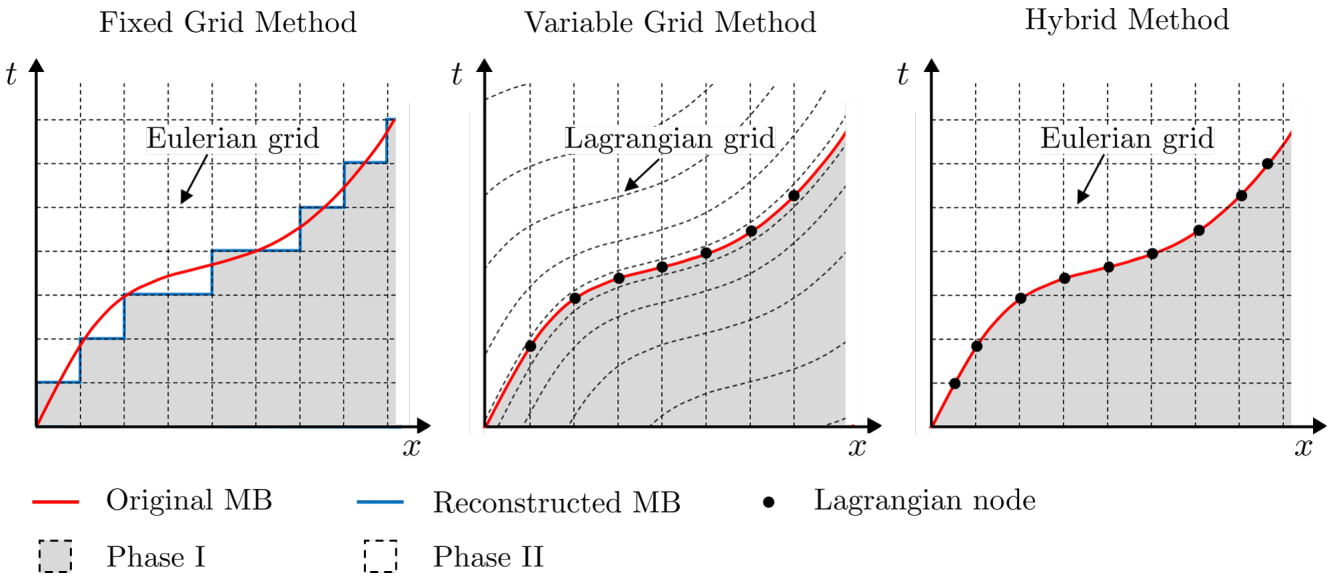

Figure 2.3. Expression of MB by using FGM, VGM and HM, respectively. FGM and VGM: Reproduced with permission from [132]. Copyright 2020, Springer; HM: Reproduced with permission from [130]. Copyright 1999, Elsevier.

2.4 Phase-field method

In the methods mentioned above, the thickness of the interface is considered to be infinitely sharp. This assumption limits their application. First, a series of partial differential equations are coupled by moving and unknown boundary conditions at the interface, which need to be explicitly tracked [133]. Complex changes in interface morphology often cause difficulties in convergence of iterations in numerical calculations. Second, treating an interface with limited width as a sharp interface leads to discontinuities in some continuously varying parameters (e.g. ion concentration and temperature fields), making it inaccurate to trace the evolution of certain physical processes. Third, anisotropic surface tension and interface kinetics are ignored, which can

lead to an unstable solution of the continuum model [133]. Irregular shape can in turn affect the direction of anisotropic growth of the interface. These formidable problems provide the impetus for developing a new model in which all these factors can be considered. The phase-field (PF) method avoids the difficulties of tracking interfaces at a conventional sharp interface by using a diffusive interface, thus can effectively simulate the complex microstructural evolution of non-equilibrium processes. In the following sections, general concepts will first be explained followed by a review of the basic thermodynamic principles, which are necessary in the context of the PF approach. Then thermodynamics of phase transitions and governing equations are be introduced.

2.4.1 General concepts

The microstructure of a material can be considered as a spatial distribution of phases and crystal structures of different compositions [134]. The evolution of the microstructure occurs as a result of phase changes, chemical reactions, the aggregation and coarsening of atoms or clusters within the material due to changes in temperature, the action of external stress, electric and magnetic fields [135]. This process is accompanied by a minimization of the total free energy (e.g. interfacial, elastic, magnetic, chemical and electrostatic energies) in the presence of an applied external field (e.g. applied stress, electric, temperature, concentration and magnetic field) [136]. Based on the energy evolution, a PF model is formulated thermodynamically by means of phenomenological free energy functions written in terms of phase and other fields (e.g. temperature, solute concentration, strain, etc.). The gradient energy across the diffusive interface is also taken into account. By minimising the free energy function, the migration of the interface can be determined [137]. Changes in the position and topology of the interface can be captured automatically without the interface tracking [138].

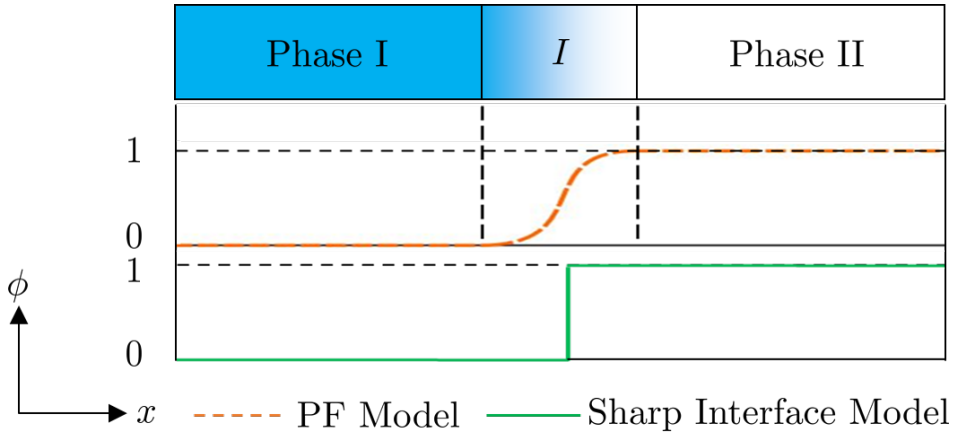

Figure 2.4. Schematic of a diffuse and sharp interface with corresponding typical interface profiles. Phases I and II are separated by the interface I. $\phi(x,t)$ varies smoothly across the interface in the PF model, taking its bulk value on either side of the interface. However, $\phi(x,t)$ is discontinuous at the interface in the sharp interface model.

Due to the universality of the energy concept, the PF method is widely used to deal with different physics and their coupling problems: solidification [15, 139], solid-state phase changes [140, 141], grain growth, nucleation and coalescence processes [142–144], dislocation dynamics [145], temperature inducing phase transformations [146], liquid-phase sintering [147], mass transport

phenomena [148], hydrodynamics [149] and electromigration [150]. Recently, many problems in solid mechanics deal with the use of PF for describing fracture phenomena and to capture complex crack patterns [151–155].

The main feature of a PF model is the description of a diffusion interface between two phases. The evolution of the interface microstructure is described in terms of a discrete order parameter (OP) that vary continuously in space and time, e.g., $\phi(x,t)$ (Figure 2.4). The OP has a constant value in the bulk phase (e.g. $\phi(x,t) = 0$ in bulk phase I and $\phi(x,t) = 1$ in bulk phase II). Over the diffusion interface ($0<\phi(x,t)<1$), the variation of $\phi(x,t)$ is described by an interpolation function. In contrast, in the sharp model, the interface width is zero, in which $\phi(x,t)$ jumps discontinuously. A second feature of a PF model is the focus on the non-equilibrium state of the phase. The OP acts as an independent state variable distinguishing different states of the material that may be identical in terms of other variables such as temperature, concentration, pressure, etc.

2.4.2 Thermodynamic free energy

The PF method is based on thermodynamics including the combined effect of the order-disorder state and the driving force to describe the evolution dynamic of a system. In the following, the basic thermodynamic principles relevant to this study are explained.

Thermodynamics is a discipline that studies the laws of state transitions and energy conversion in thermal phenomena. It is mainly concerned with the equilibrium state of matter and the physicochemical processes associated with the quasi-equilibrium state [156]. Thermodynamic processes with different limiting conditions are accompanied by different expressions of the free energy, which serves as a criterion for whether a process can proceed spontaneously or not. If the free energy changes negatively, the process can proceed spontaneously; if the free energy changes positively, the process cannot proceed spontaneously, but the reverse process is spontaneous [157]. When the change of the free energy equals to zero, the system is in thermodynamic equilibrium [157]. For a closed isothermal system (one that can not exchange any matter with its surroundings) with no chemical reactions in a constant volume, the Helmholtz free energy F can be expressed by the internal energy U, the temperature T and the entropy S of the system

$$F = U - TS. \tag{2.21}$$

The Gibbs free energy G is most commonly used as a measure for the judgment (especially in chemistry) when it is convenient for applications that occur at constant pressure P and T

$$G = U + PV - TS = H - TS, \tag{2.22}$$

where, H is the enthalpy.

The basic thermodynamic relationships are expressed by the following equation. For a closed system in thermal equilibrium, the microscopic change in internal energy $\mathrm{d}U$ is expressed by microscopic changes in entropy $\mathrm{d}S$ and volume $\mathrm{d}V$

$$\mathrm{d}U = T\,\mathrm{d}S - P\,\mathrm{d}V. \tag{2.23}$$

The fundamental relation can be also expressed in terms of G in the following way

$$\mathrm{d}G = -S\,\mathrm{d}T - V\,\mathrm{d}P. \tag{2.24}$$

2.4.3 Thermodynamics of phase transitions

A thermodynamic system may contain different phases. The states of these phases change at critical values under varying external conditions [158]. In order to describe the phase transition, the thermodynamic potential is used along with the corresponding equation of state, which describe the state of matter under a given set of physical conditions, e.g., pressure, volume and temperature. As mentioned in section 2.4.2, the thermodynamic potential can be expressed in terms of G [159]. The following section will provide a brief description of G and the chemical potential of an ideal solution and a binary phase system.

The chemical potential is the amount of energy that can be absorbed or released as a result of a change in the particle number of a given species during a chemical reaction [160]. For a given temperature, a molecule has a high chemical potential in the region of high concentration and a low chemical potential in the region of low concentration. The molecule tends to move from the region of higher chemical potential to the region of lower chemical potential, accompanied by the release of free energy. At chemical equilibrium, the free energy of the system is at minimum. The chemical potential of a species μ_i is also known as the molar Gibbs free energy under the condition of constant T, P and amount of all other components N_j [161]

$$\mu_i = \left(\frac{\partial G}{\partial N_i}\right)_{T,p,N_{j\neq i}}, \tag{2.25}$$

where, N is the number of molecules.

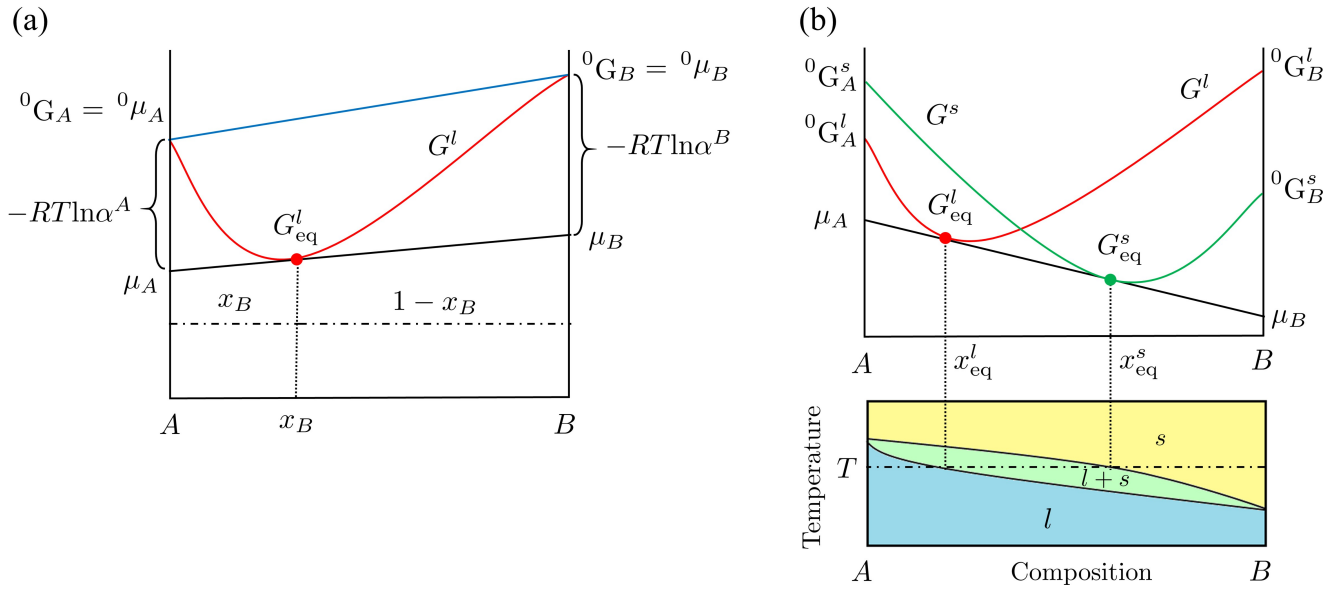

Figure 2.5. (a) The relationship between Gibbs free energies and chemical potentials of an ideal solution, Reproduced with permission from [162]. Copyright 2014 Elsevier; (b) Gibbs free energy curves corresponding to binary phase diagrams, showing the miscibility of the liquid and solid states, Reproduced with permission from [163]. Copyright 2006 John Wiley and Sons.

The relationship between the molar Gibbs free energy and the chemical potential can be well elucidated with an ideal solution (a solution with zero enthalpy of mixing) consisting of two

components A and B (Figure 2.5a). The left and right vertical lines represent the state of the two pure components. The straight blue line connecting the molar Gibbs free energy of the pure components represents the molar Gibbs energy of the mechanical mixture, while the red curve represents the molar Gibbs free energy of the ideal solution G^l. The intersection of the tangent line to the lowest point of the G^l curve (the equilibrium state) with the sides of pure component A and B marks their corresponding chemical potentials μ_{A} and μ_{B}. The minimum molar Gibbs free energy of the solution with the composition x_{A} and x_{B} ($x_{\mathrm{A}} + x_{\mathrm{B}} = 1$) is

$$G^l_{\mathrm{eq}} = x_{\mathrm{B}}\mu_{\mathrm{A}} + (1 - x_{\mathrm{B}})\mu_{\mathrm{B}}. \tag{2.26}$$

In addition, the difference between the molar Gibbs free energy of the pure component ($^0\mathrm{G}_A$ and $^0\mathrm{G}_B$) and the chemical potential of A and B can be written with the activity of component α as: $-RT\ln\alpha^{\mathrm{A}}$ and $-RT\ln\alpha^{\mathrm{B}}$, respectively,

$$^0\mathrm{G}_A - \mu_A = -RT\ln\alpha^{\mathrm{A}}, \tag{2.27}$$

$$^0\mathrm{G}_B - \mu_B = -RT\ln\alpha^{\mathrm{B}}. \tag{2.28}$$

For a heterogeneous system with two or more phases, such as pure components A and B both containing liquid (l) and solid (s) phases, the Gibbs free energy curves of the two phases must be considered separately (Figure 2.5b). $^0\mathrm{G}^l_A$, $^0\mathrm{G}^l_B$, $^0\mathrm{G}^s_A$ and $^0\mathrm{G}^s_B$ denote the molar Gibbs free energy of the liquid and solid phases of the A and B pure component systems, respectively. The compositions of the two phases in equilibrium at temperature T are $x^{\mathrm{l}}_{\mathrm{eq}}$ and $x^{\mathrm{s}}_{\mathrm{eq}}$, with their corresponding Gibbs free energies denoted as G^l_{eq} and G^s_{eq}, respectively.

2.4.4 Governing equations

The evolution of OPs can be described by their variable fractions of the free energy functional. Depending on whether the OPs are conserved or not, the equations for their evolution can be divided into two categories: (1) non-conserved field variables (e.g. ferroelectric polarisation fields [164, 165], grain orientation fields [143], gas-liquid-solid phase fields [166] and cracking fields [152]) mainly using the Allen-Cahn equation [167], and (2) conserved field variables (e.g. concentrations [168, 169]), whose dynamics are mainly described by the Cahn-Hilliard equation [170],

The Allen-Cahn equation:

$$\frac{\partial\phi_i(x,t)}{\partial t} = -L_\phi\frac{\delta F}{\delta\phi_i(x,t)}, \tag{2.29}$$

where $\phi_i(x,t)$ is the non-conserved field variable with i = 1, 2 ..., n, while L_ϕ is the kinetic structure operator (PF mobility); t is the time and x is the spatial coordinate.

The Cahn-Hilliard equation:

$$\frac{\partial c_i(x,t)}{\partial t} = \nabla M_c \nabla\frac{\delta F}{\delta c_i(x,t)}, \tag{2.30}$$

where c_i is the conserved concentration field variable; M_c is the kinetic coefficient of diffusion.

One of the key components of the PF method is the free energy functional. When temperature, pressure and molar volume are constant and there are no elastic, magnetic or electric fields, the total free energy of a system consisting of a concentration field c and the OP ϕ can be given by [134]:

$$F(\phi, c) = F_{\text{loc}} + F_{\text{int}} = \int_V [f_{\text{loc}}(\phi, c) + f_{\text{int}}(\nabla\phi, \nabla c)]\, \mathrm{d}V, \tag{2.31}$$

where, F_{loc} and F_{int} represent the energy contributions from the homogenous local phases and the diffuse interface region, respectively; f_{loc} represents the contribution of chemical interactions to the local free energy density, f_{int} is the gradient energy density, which is only non-zero at and around the interface.

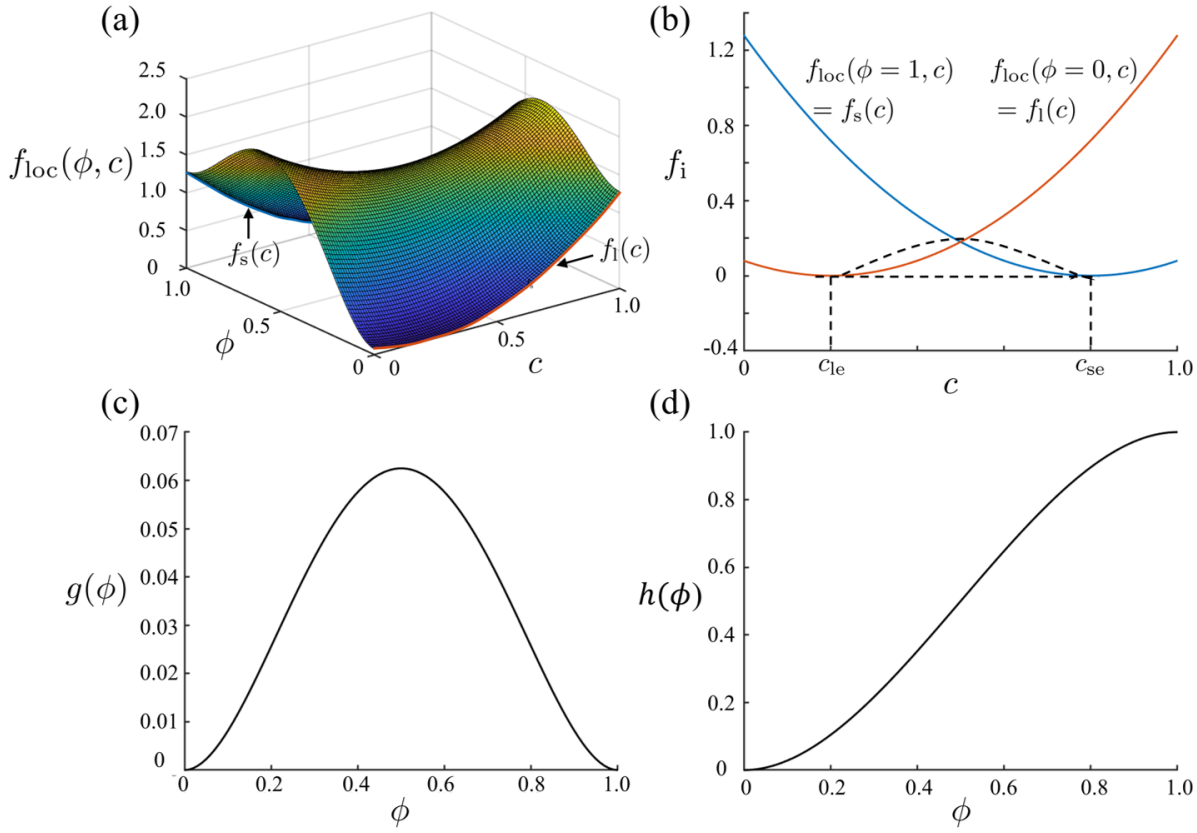

Figure 2.6. Graphic illustration for key functions of PF model. (a) 3D graphic of the local free energy f_{loc} as a function of the solute concentration c and the OP ϕ; (b) the free energy of the solid and the liquid phase; (c) the double-well function $g(\phi)$; (d) the interpolation function $h(\phi)$.

In a binary system, f_{loc} is commonly expressed as the free energy expressions of the coexisting phases combined by an interpolation function $h(\phi)$ and a double-well function $wg(\phi)$ (see Figure 2.6(a)):

$$f_{\text{loc}}(\phi, c) = h(\phi) f_s(c) + (1 - h(\phi))\, f_l(c) + wg(\phi) \tag{2.32}$$

where, $h(\phi)$ has a variety of expressions in the literature, e.g., $h(\phi) = -2\phi^3 + 3\phi^2$ [1] and $h(\phi) = \phi^3(6\phi^2 - 15\phi + 10)$ [136], both change from $h(0) = 0$ to $h(1) = 1$; w is the height of the double-well function $g(\phi) = \phi^2(1 - \phi)^2$ [1]; $f_s(c)$ and $f_l(c)$ are homogeneous free energy

expressions for c dependence of the solid and the liquid phase. Figure 2.6 (b) shows that the concentration of the interface lies between c_{le} and c_{se}. The tangent line indicates the equilibrium component of the coexisting phases. The dotted curve shows a possible evolution of f_{loc} across the interface. The functions $g(\phi)$ and $h(\phi)$ are used to construct f_{loc}, which are plotted in Figure 2.6 (c) and (d), respectively.

2.4.5 Multi phase-field model

Self-healing of cementitious materials can also be considered as a physicochemical reaction involving multiple phases including the cement matrix phase, the self-healing product phase consisting of the product of the further hydration and the carbonation reaction, air void phase and the solution phase. A review of multiphase models in the literature provides important insights into solving of the self-healing problems. In dealing with complex phase transformations, such as structure (poly-crystal) [171], multi-phase and/or multi-component (alloys and mixtures of fluids) [172–174] or the orientation of the crystal lattice (grains) [175], multi PF models are introduced. The phase is represented by a set of OPs ϕ_i. The following basic constraint is often applied to a system with N phases [176]

$$\sum_{i=1}^{N} \phi_i = 1. \tag{2.33}$$

For conserved OPs, the following constraint is commonly used

$$c = \sum_{i=1}^{N} h(\{\phi_i\}) c_i, \tag{2.34}$$

where $h(\{\phi_i\})$ is an interpolation function.

Table 2.3. A review of multi-PF models

Multi-PF model	Feature	Application	Reference
WBM model	Phases have the same composition but different volume fractions	Solidification in binary alloys	[177, 178]
KKS model	Phases have different compositions	Solidification in binary alloys	[1]
Steinbach model	Geometric description of the interface through the interface curvature	Eutectic and peritectic solidification, grain growth	[176, 179]
Losert model	Directional solidification with some asymptotics and vanishing kinetics	Solidification in dilute binary alloy	[180]

Commonly used models for addressing two or multi-phase transition processes are Wheeler-Boettinger-McFadden (WBM) model [177, 178], Kim-Kim-Suzuki (KKS) model [1], Steinbach model [176, 179] and Losert model [180], which are summarized in Table 2.3. Since the inception of these models, many other studies have used or expanded the ideas in the above references [181–184].

Wheeler et al. [177, 178] proposed a PF model dealing with isothermal phase transitions in binary alloys. The WBM model works well for sharp interface and finite interface thickness issues, but is not applicable for large interface thicknesses cases [179, 183, 185, 186]. The Gibbs free energy functional is based on the chemical potential of each component combined with the corresponding weighted concentration, which is given by

$$f(\eta, c, T) = c f_{\mathrm{B}}(\eta, T) + (1-c) f_{\mathrm{A}}(\eta, T) + \frac{RT}{v_{\mathrm{m}}}[c \ln c + (1-c)\ln(1-c)]. \tag{2.35}$$

Different from the WBM model, the interface in the Kim–Kim–Suzuki (KKS) model [1] was defined as a mixture of liquid and solid phases of different compositions, but with the same chemical potential as follows

$$\frac{\partial f(c'_{\mathrm{s}})}{\partial c'_{\mathrm{s}}} = \frac{\partial f(c'_{\mathrm{l}})}{\partial c'_{\mathrm{l}}}. \tag{2.36}$$

In the KKS model, each point throughout the domain is a mixture of two phases. The local free energy is determined to be a fraction-weighted average value of both solid and liquid free energy and an imposed double-well potential $\omega g(\phi)$ as follows

$$f(c', \phi) = h(\phi) f_{\mathrm{s}}(c'_{\mathrm{s}}) + [1 - h(\phi)] f_{\mathrm{l}}(c'_{\mathrm{l}}) + \omega g(\phi), \tag{2.37}$$

where the interpolation function $h(\phi)$ is built as $h(\phi) = -2\phi^3 + 3\phi^2$, ω is the height of the double well potential energy function given by $g(\phi) = \phi^2(1-\phi)^2$. Unlike the two models mentioned above, the model proposed by Steinbach et al. [176, 179] is not based on a thermodynamic treatment, but on a geometric description of the interface through an interpolation function of the interface curvature. The free energy functional is postulated

$$\begin{aligned} f(\phi) &= \sum_{i,k(i<k)}^{n} f_{ik} \\ &= \sum_{i,k(i<k)}^{n} \left\{ \frac{\varepsilon_{ik}^2}{2} |\phi_k \nabla \phi_i - \phi_i \nabla \phi_k|^2 + \frac{1}{4\alpha_{ik}} [\phi_i^2 \phi_k^2 \right. \\ &\quad \left. - m_{ik}(\frac{1}{3}\phi_i^3 + \phi_i^2 \phi_k - \frac{1}{3}\phi_k^3 - \phi_k^2 \phi_i)] \right\}, \end{aligned} \tag{2.38}$$

where f_{ik} is the energy term that is sensitive on the boundary between phases i and k; n is the number of phase states in a system; m_{ik} is the linear coefficient of the thermodynamic equilibrium deviation; ε_{ik} and α_{ik} are the thermophysical data.

Later, Losert et al. [180] exploited the similarity between alloys and pure materials to extend the thin interface model to the case of dilute binary alloys by matching variables in the pure material. However, there are two strict assumptions that limit the application of the model: (1) the solid

and the liquid phases have constant partition coefficients, and (2) the solute diffusivity is constant throughout the whole domain.

$$\begin{aligned}\tau(n)\partial_t\phi = (1-\phi^2)\left[\phi + \alpha(\phi^2-1)\left(\mu + \frac{z - z_0 - V_p t}{l_T}\right)\right] \\ + \vec{\nabla}[w(n)^2\vec{\nabla}\phi] + \partial_x\left(|\vec{\nabla}\phi|^2 w(n)\frac{\partial w(n)}{\partial \phi_x}\right) \\ + \partial_z\left(|\vec{\nabla}\phi|^2 w(n)\frac{\partial W(n)}{\partial \phi_x}\right),\end{aligned} \tag{2.39}$$

where $\tau(n)$ is a function related to ϕ; n is a normal vector; μ is a factor of the chemical potential; α is a constant factor; z and z_0 represent the real and the reference interface position, respectively; z_0 is the reference position of the steady state planar interface; l_T is the thermal length; V_p is a constant interface velocity and $w(n)$ is the interface thickness.

Based on the above review, the existing research on PF methods related to cementitious materials need to be summarized. As the main initial process of the self-healing mechanism, mineral component dissolution, will be investigated using the PF method to understand and verify the feasibility of the PF method for the moving boundary problem of mineral dissolution. The estimation of interfacial mobility and the interaction analysis of PF parameters need to be done, which lays the theoretical foundation for the multi-process multi-interface simulation. Based on the PF dissolution model validated in the previous step, a novel PF model dealing with the dynamic equilibrium of dissolution and precipitation will be developed. In the following chapter, the methodology, implementation and results of each step of the study will be described in detail through the three peer-reviewed publications.

3 Results

3.1 Publication 1: A Review on Cementitious Self-Healing and the Potential of Phase-Field Methods for Modeling Crack-Closing and Fracture Recovery

Sha Yang[1], Fadi Aldakheel[2], Antonio Caggiano[1,3], Peter Wriggers[1] and Eddie Koenders[1]

1 Institute of Construction and Building Materials, Technical University of Darmstadt, Franziska-Braun-Straße 3, 64287 Darmstadt, Germany

2 Institute of Continuum Mechanics, Leibniz Universitaet Hannover, An der Universitaet 1, 30823 Garbsen, Germany

3 CONICET and LMNI-FIUBA, Universidad de Buenos Aires, Buenos Aires C1127AAR, Argentina

Journal: Materials 2020, 13(22), 5265; https://doi.org/10.3390/ma13225265

3.1.1 Introduction

Concrete is characterized by its high compressive strength, a wide availability of its raw materials, and simple production methods, which is the main reason that it became the most commonly used construction material in the world [187, 188]. However, its low tensile strength is the main reason that various types of cracks can occur in a concrete element that may adversely affect its service life [189]. While under internal, external, or environmental load, open or closed micro- and/or meso cracks may develop inside a concrete element that may successively result in a loss of structural integrity [190]. Open surface cracks may also allow water or hazardous substances to enter and thereby severely impairing its durability [191, 192]. Therefore, improving the durability of concrete structures, asks for a limitation or reduction of the number of cracks where self-healing strategies could be solution. In the last decades, enormous efforts have already been done to develop various kinds of self-healing methods for cementitious systems [166, 193–200]. Most comprehensive scientific report so far is the RILEM TC-221-SHC [14], that summarizes the current research progress and defines the difference between “autogenic” and “autonomic” self-healing methods, depending on whether crack closure happens due to either the material itself [29, 201–203], or is triggered by means of engineered additions [28, 46, 70, 77, 198, 199, 204–209].

From a modeling point of view, the presently existing numerical approaches can be grouped according to the nature of their particular self-healing mechanism into (1) chemical reaction-based

models [32, 87, 89, 92, 166], for predicting carbonation, hydration, polymerization and precipitation phenomena; (2) transport phenomena-based models [94, 210], in which the phases affecting the healing processes are transported through the concrete pore-structure network; and (3) fracture-based models, smeared [88, 91, 98, 99, 103, 104, 108, 110–112] and discrete [100, 105, 107, 109, 113–115] crack approaches for predicting strength recoveries of self-healing systems.

When considering the number and type of experiments required to study the performance of self-healing concrete, it turns out that optimizing self-healing mechanisms through extensive experimental studies is a very demanding task. However, this task becomes more doable when employing numerical simulation models. However, most existing models do not incorporate physically/chemically driven boundary movements for an accurate simulation of solid-liquid interfaces. To overcome these difficulties, phase-field (PF) methods have been proposed as a powerful tool for handling moving interfaces caused by phase transitions [15, 135, 211]. In conventional numerical models for phase transformations and microstructural evolutions, interfaces are considered to be infinitely sharp and have to be schematized explicitly [212–214]. It leads to incompatibilities that makes calculations very complex and difficult to implement in a computer program. Contrarily, PF methods are based on thermodynamic principles and assume a diffuse interface, which makes them suitable for solving complex morphological evolutionary processes. The evolution of the "field", over time and space, is controlled by the nonlinear Cahn-Hilliard diffusion equation and its relaxation by the Allen-Cahn equation [215, 216]. For concrete, a self-healing mechanism is physically almost similar to a dissolution and/or precipitation principle that evolves at the cracked surfaces. It makes a PF modeling approach very suitable for solving this type of moving interface problems at cracked surfaces, caused by phase transformations.

This article provides a review on existing models to simulate self-healing in cracked concrete, with emphasis on PF methods. After the introduction in Section 3.1.1, the currently available self-healing methods for concrete are reported in Section 3.1.2. In Section 3.1.3, the possibility of using PF methods for simulating self-healing in concrete is presented and discussed. Then, in Section 3.1.4, the basic equations of a PF method are presented. Next, in Sections 3.1.5 and 3.1.6 existing PF techniques for precipitation and fracture in concrete are reported, respectively. Finally, items that should be addressed in self-healing models along with future research priorities and a concluding discussion on the whole article is given in Section 3.1.7.

3.1.2 Self-Healing Mechanisms in Concrete

In general, self-healing processes in cement-based materials can be divided into two categories: (1) autogenous self-healing and (2) autonomous self-healing [195, 217, 218]. Autogenous self-healing involves only the original components of a concrete. These components may, due to their specific chemical compositions, promote crack healing under favorable environmental conditions, driven by chemical reactions or transitions [30, 34, 196]. However, autonomous self-healing processes can only take place with the help of healing additives, such as microcapsules that may contain healing agents like polymers or bacterial spores [199, 219]. Autogenous healing mechanisms have a limited healing capacity, typically only being able to heal cracks of about 100-150 µm in width [13]. In contrast to this, autonomous mechanisms can easily heal cracks up to 300 µm µm and sometimes even more than 1 mm [13]. These self-healing mechanisms are described below in detail.

3.1.2.1 Autogenous Self-Healing

Autogenous self-healing has been extensively investigated in the last decades [12, 34, 195, 196, 220], mainly by using experimental techniques.

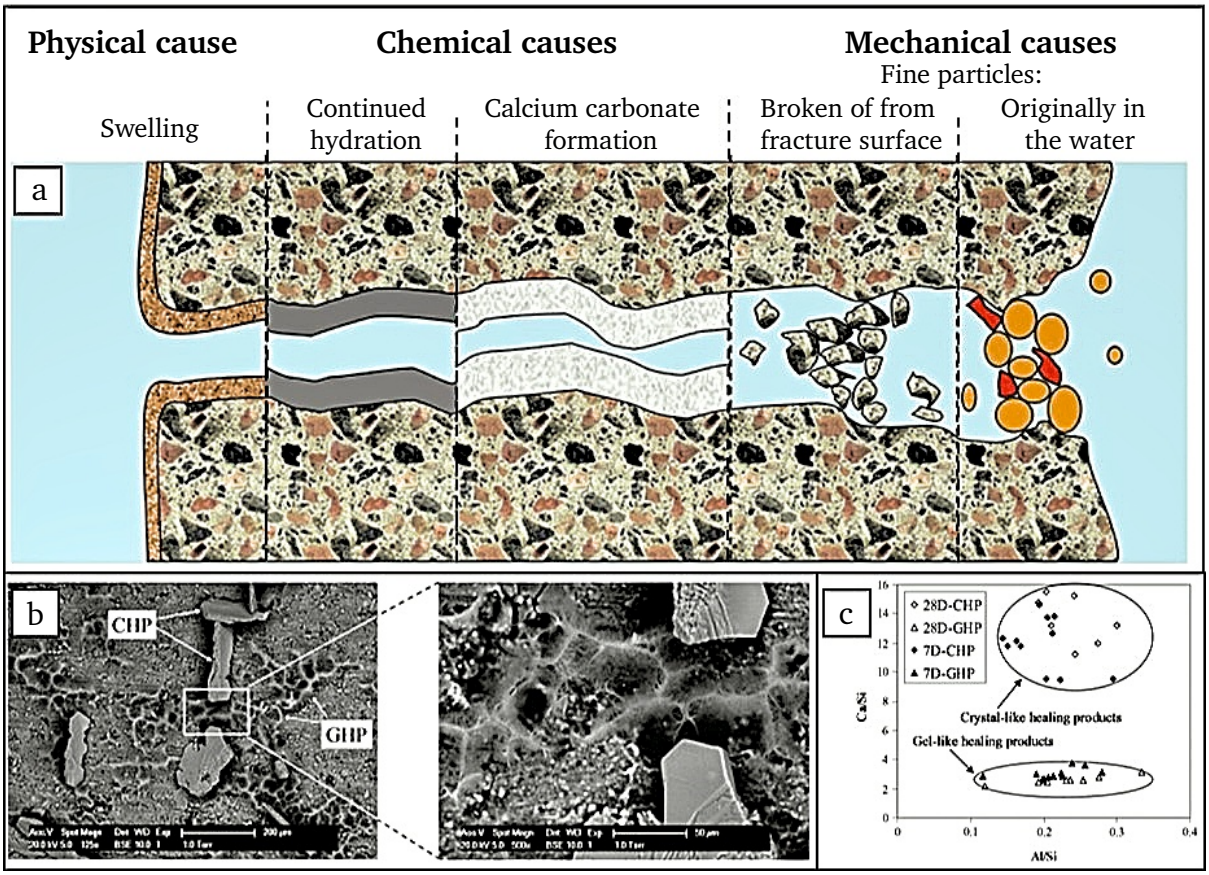

Figure 3.1. The autogenous self-healing mechanisms, products, and their corresponding chemical composition. (a) Schematic representation of the mechanisms of autogenic self-healing. Reproduced with permission from the authors of [221]. Copyright 2013, Springer. (b) Morphology of healing products (GHP refers to the gel-like healing product and CHP refers to the crystal-like healing product). Reproduced with permission from the authors [31]. Copyright 2013, Elsevier. (c) Ratios of Ca/Si and Al/Si of healing products with time. Reproduced with permission from the authors of [31]. Copyright 2013, Elsevier.

Figure 3.1a shows three main categories: physical, chemical, and mechanical healing. The physical healing mechanism is the process where the crack surface inside a cement matrix absorbs water and causes volume expansion [221, 222]. The chemical healing mechanism consists of two main reactions, namely, a further hydration of the still unhydrated cement clinker inside a concrete, generating additional Calcium Silicate Hydrates (C-S-Hs), and carbonation of the additionally formed portlandite [34–36, 223]. Finally, mechanical healing mechanisms refers to the filling of a crack with fine cement particles, which appear in a crack by water transport or diffusion [35]. The chemical mechanism is the primary and most promising healing method for hardened concrete at a young age [14]. Due to the relatively high content of unhydrated cement particles in these concretes, continuing hydration will still be possible and may result in a healing of cracks [29, 30].

At later ages after crack initiation, the formation and growth of calcium carbonate crystals ($CaCO_3$) becomes the main healing mechanism [37]. Figure 3.1b,c shows the main healing products and their chemical components.

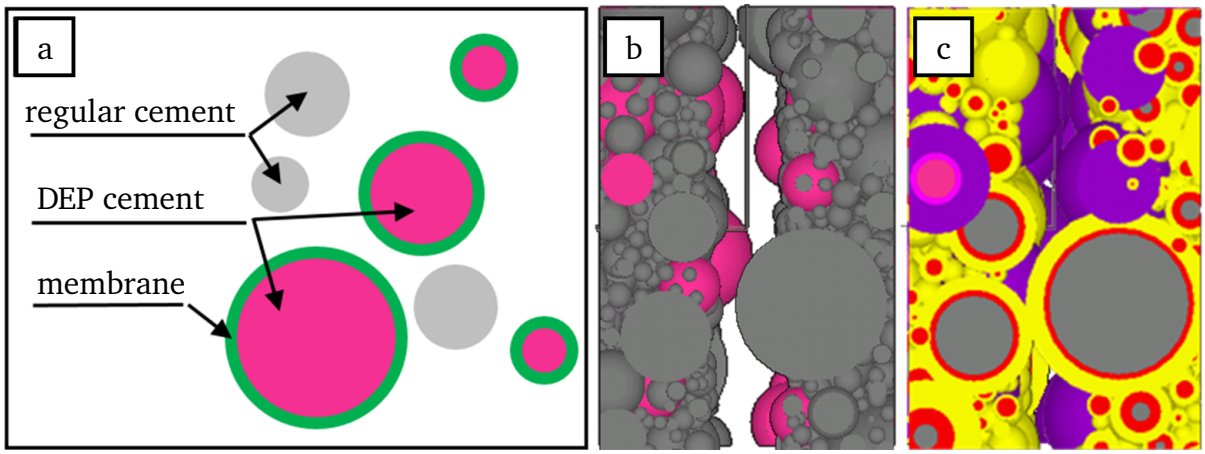

Figure 3.2. Self-healing with Dissoluble Encapsulated Particles (DEP): (a) Schematic representation of regular cement blended DEP cement [166]. (b) Initial state of microstructure by vol.-10% cement replacement by DEP [166]. (c) A high pH value will cause the DEP capsule to rupture, the healing agent will be released and a special hydration reaction with accompanying volume expansion will begin [224].

To improve the effectiveness of autogenous crack repair, an improved self-healing method called Dissoluble Encapsulated Particles (DEP) has been proposed [166, 197, 224]. In this self-healing method a certain amount of cement in a concrete mixture remains unhydrated for a predefined period of time because of the pre-encapsulation of certain cement fractions which are covered with a thin membrane that can dissolve whenever it is affected by a crack (Figure 3.2). A crack in a cementitious surface may open the DEP membrane due to either (1) a dissolution mechanism caused by low pH-conditions, i.e. due to increased CO_2 ingress, or (2) by mechanical fracture. After this happened, the original unhydrated cement will be exposed to the local environmental temperature and humidity conditions causing the cement to react and finally close the crack [224].

3.1.2.2 Autonomous Self-Healing

Autonomous self-healing is a method to improve the effectiveness of self-healing mechanisms for concrete, by either embedding encapsulated or non-encapsulated additions [13, 217]. Until now, addition of encapsulated agents (micro/meso $<$ 1 mm, macro $\geq$ 1 mm) is the most preferred method adopted for autonomous self-healing concrete [13], which may contain mineral [41, 43], bacteria [49, 70–72, 199, 225–230], and polymers [200, 231, 232]. Non-encapsulated additions may also contain these listed substances, but are added to a mixture in a pure, non-encapsulated, form where they become active directly after mixing of the concrete [68, 233, 234].

3.1.2.3 Self-Healing Based on Mineral Admixtures

Mineral admixtures are materials that are mixed in a concrete and react with water to form reaction products with an expanded volume to heal cracks developed in an already hardened concrete.

With this healing mechanism [42, 68, 198, 235], crack widths up to 120 µm can be repaired [13].

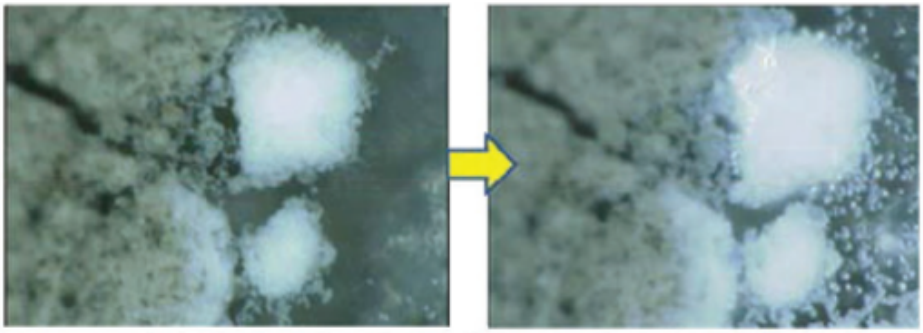

(1) Expansion term (Expansive agents)

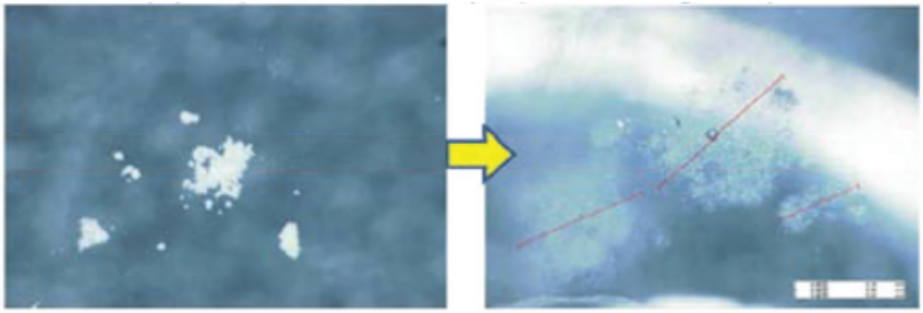

(2) Swelling term (Geo-materials)

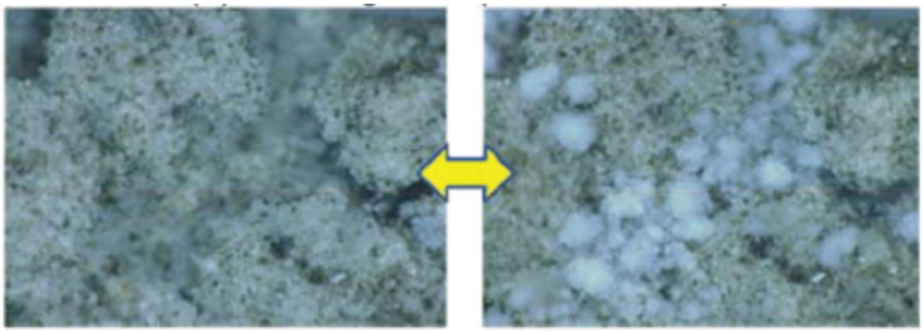

(3) Precipitated term (Chemical agents)

Figure 3.3. Three main self-healing mechanisms using mineral admixtures. Reproduced with permission from the authors of [43]. Copyright 2010, JCI.

Depending on the type of mineral additives, three subcategories can be identified: (1) expansive additives, (2) geo-material based additives, and (3) chemical agents (crystalline additives) (Figure 3.3). Expansive additives develop reaction products with an increased volume that can fill the cracks [58]. Commonly used are sulfoaluminate based expansive additives (C−S−A) [41]. The geo-material-based additives consist of silicon dioxide, sodium aluminum silicate hydroxide, and bentonite clay, which have the capacity to swell [43–45]. When this type of geo-material is exposed to water, its volume may increase 15-18 times its initial dry volume [43]. The most basic crystalline additive is tricalcium silicate (C_3S), which is the main clinker component in cement and reacts with water to form calcium silicate hydrate C−S−H phases [46].

3.1.2.4 Self-Healing Based on Bacteria

A certain category of bacteria can be applied for healing cracks in concrete [70]. It results in a closed crack which is watertight and has a limited capacity to restore the mechanical strength of a concrete [71, 72, 225]. The maximum crack width that can be healed with this system are 150 µm [226], which is rather limited whenever compared with other healing systems. Figure 3.4 shows a schematic impression of a fractured concrete with microencapsulated bacterial spores and the results of previous experiments [71, 72, 236].

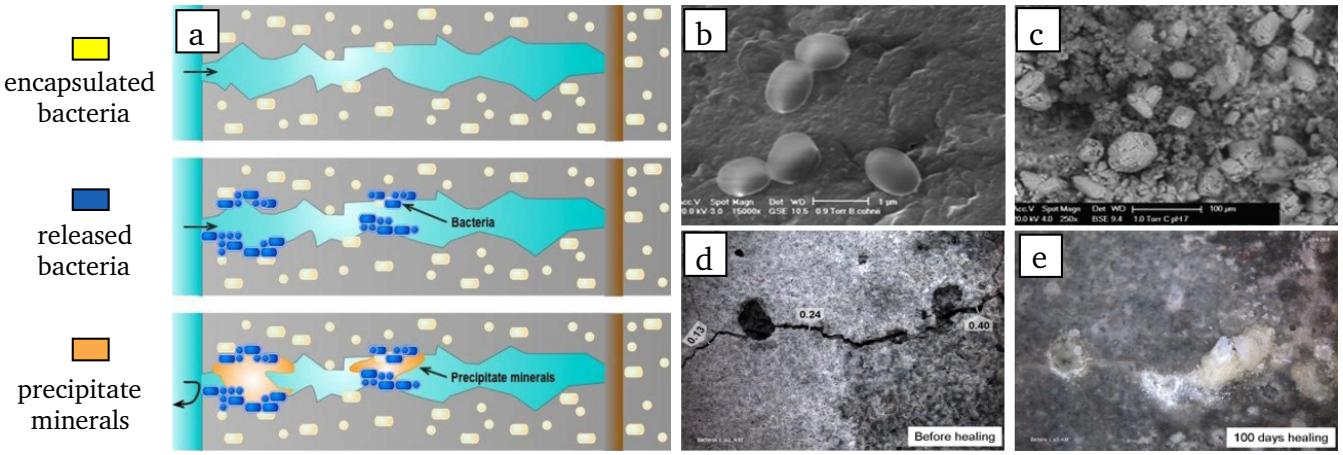

Figure 3.4. Self-healing mechanism using bacterial spores. (a) Schematic diagram of bacterial repair of concrete cracks. Bacteria on the surface of the crack are activated by water and precipitate minerals such as calcite to seal the crack and protect the reinforcement from external chemical attack. Reproduced with permission from the authors of [236]. Copyright 2018, Elsevier. (b) ESEM photomicrograph (15,000×magnification) of B. cohnii spores, showing that spore diameter sizes are up to 1 µm. Reproduced with permission from the authors of [71]. Copyright 2010, Elsevier. (c) Mineral precipitates (20-80 µm sized) on crack surfaces (250×magnification). Reproduced with permission from the authors of [71]. Copyright 2010, Elsevier. (d) Stereomicroscopic images of crack-healing process in bio-chemical agent-based specimen before and (e) after 100 days healing. Reproduced with permission from the authors of [72]. Copyright 2011, Elsevier.

Bacteria provide an important reaction component in a self-healing mechanism, where they are enhancing the calcium carbonate $CaCO_3$ production, needed for crack closing [237]. During healing, the mechanism passes the following two sequential steps; (1) conversion of calcium lactate and (2) hydrolysis of urea through (ureolytic) bacterial metabolism. In the first mechanism, oxygen and water penetrate into the concrete interior through cracks where the bacteria are activated to convert calcium lactate into $CaCO_3$ crystals and CO_2. Portlandite particles near the cracks will further react with CO_2 to produce more $CaCO_3$ which precipitates at the crack surfaces [72]. In the second mechanism, many components capable of producing organic urea (e.g. Bacillus cohnii, Sphaericus, Subtilis, Pasteurii, Megaterium and Sporosarcina ureae) can act as a catalyst during the self-healing process [76]. As it undergoes demineralization, negatively charged bacterial cells take up components from the cell wall and then react to $CaCO_3$ precipitates [238].

The efficiency of the precipitates generated by bacterial induction is determined first by the available water content and moisture movement in the concrete matrix [239, 240], and second by the concentration of calcium ions, the pH of the pore solution, the concentration of inorganic carbon and by the presence of nucleation sites [241, 242]. The first three are available in the concrete matrix, while the last one is related to the type of bacteria used [225]. In addition, factors that affect the effectiveness of healing include (1) the type of carrier (direct [243], encapsulated [52] containers like clay and aggregates [64, 80]) and (2) the concrete compatible chemical reactions taking place in producing $CaCO_3$ [228, 244].

3.1.2.5 Self-Healing Based on Adhesive Agents

This method is based on injecting adhesives into a crack to induce manual healing [56, 81]. The crack widths which can be healed with these systems vary from 50 µm up to 250-300 µm [13, 245]. Adhesive agents can be divided into one-component and multicomponent systems. Commonly used one-component adhesive agents are polyurethane [53] and epoxy [54]. Multicomponent adhesives are methylmethacrylate [55] and ureaformaldehyde/epoxy [56]. Adhesive agents are encapsulated in spherical capsules [81], tubular-shaped capsules [55, 246], and hollow fibers [82, 247, 248] that are mixed with fresh concrete (Figure 3.5). When cracks occur, rupture of the encapsulation takes place, where the adhesive will be released into the crack by capillary action, initiating crack healing with time.

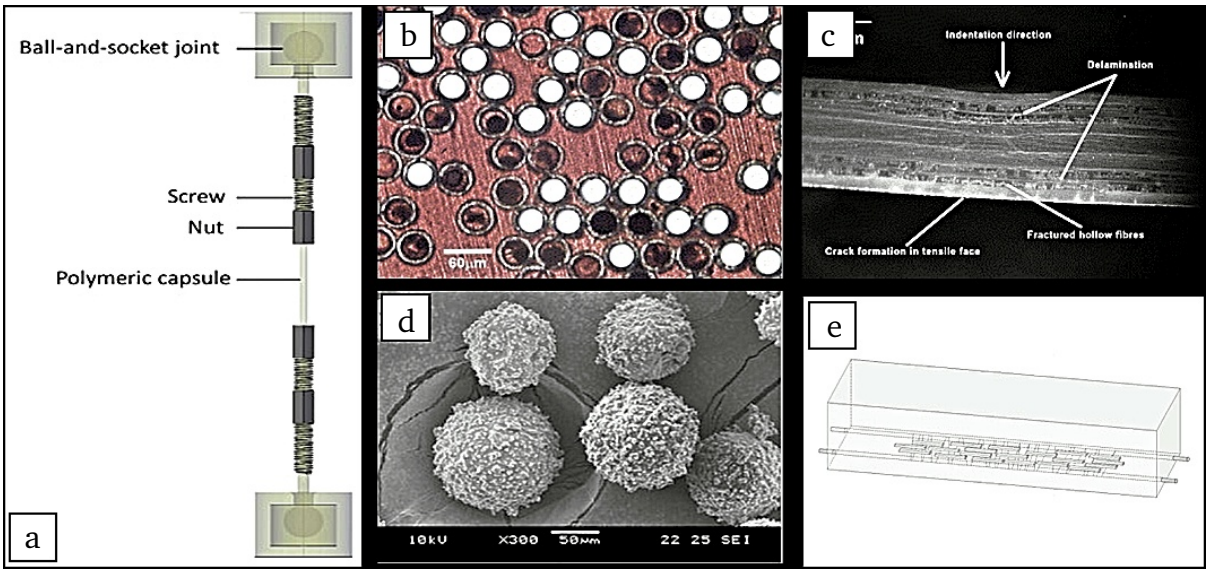

Figure 3.5. Self-healing mechanism based on adhesive agents. (**a**) Test setup used to determine the tensile strength of laboratory-scale hollow glass tubes with an outer hole of diameter 5 mm and an inner pin of diameter 3 mm. Reproduced with permission from the authors of [55]. Copyright 2015, Elsevier. (**b**) Hollow glass fibres of 60 µm external diameter with a hollowness of 50%. (**c**) Cross section through impact damaged hybrid solid glass/hollow glass/epoxy laminate. Reproduced with permission from the authors of [247]. Copyright 2005, Elsevier. (**d**) Spherical microcapsules with diameter of 120 $\pm$ 33 µm. Reproduced with permission from the authors of [249]. Copyright 2012, Elsevier. (**e**) Short glass/ceramic capsules attached to reinforcement, Reproduced with permission from the authors of [246]. Copyright 2015, Elsevier.

3.1.3 Phase-Field Methods for Modeling Concrete Self-Healing

The Phase Field (PF) method for simulating lower scale micro- and/or mesostructural cracking in materials has got an enormous upswing in the last decades. However, so far classical PF applications were focusing on the distribution of non-reactive multi-phase systems [250]; solidification problems [15, 139]; solid-state phase changes [140, 141]; grain growth, nucleation, and coalescence processes [142–144]; dislocation dynamics [145]; temperature inducing phase transformations [146]; liquid-phase sintering [147]; mass transport phenomena [148]; hydrodynamics [149]; and electromigration [150]. Recently, many problems in solid mechanics deal with the use of PF for describing fracture phenomena and to capture complex crack patterns [151–155]. Based on the present literature review, the following can be summarized.

- PF is an extremely powerful mathematical modeling scheme for accurately describing physical movements of phase boundaries.
- PF was mainly employed for solving solidification dynamics, material phase changes/separations, growing phases driven by chemo-kinetics and transport phenomena, nucleation and coalescence processes between particles in micro-to-mesostructures.
- PF has been successfully employed in fracture mechanics to capture the cracking response of brittle/ductile materials without the need for employing Discrete Crack Approaches (DCAs) and/or Smeared Crack Approaches (SCA).

Because of this, and as also supported by various state-of-the-art reports [15, 165, 211, 251–253], PF models can be employed for self-healing of brittle or plastic (ductile) materials in a fundamental and consistent way. It will combine the impact of two main phase changes that occur simultaneously in a self-healing mechanism, i.e. chemical reactions and fracture. Gradual changes from the fully-cracked (failure) to the uncracked configuration can be driven through the so-called Phase-Field order parameter (ϕ). It will provide a smooth transition of all relevant phenomena between the fully cracked configuration and the intact material phases: this strength and crack recoveries actually represent the self-healing process. The governing equations of the proposed unified model will be derived in the framework of thermodynamics concepts, in terms of kinematics and balance equations, dissipation inequality and constitutive laws. Particularly, the free energy will be considered as the sum of the contributions due to elasticity, reaction PF and fracture PF. The free energy of the system is described in a unified form over the entire phase transition region. In this regard, the advantage of the PF method over other competitive numerical methods is its enormous capability of capturing movements of interfaces, without the need for introducing any additional ad hoc technique, criteria and/or remeshing strategies, and also without any explicit tracking of the actual interface positions of these coupled processes. The governing equations of PF models for chemical/moisture reactions and fracture processes, associated with self-healing, as well as the coupling among them, can be formulated in a unified PF framework. The next sections report a review on the available formulations for a unified and coupled set of PF approaches for modeling reactions and fracture of self-healing mechanisms in concrete.

3.1.4 Main Equations of a Phase-Field Approach

The phase-field (PF) approach is a very powerful technique to simulate complex physical phenomena in multi-field environments. The main attributions of this approach are simplicity and generality.

A popular PF application is a diffusion interface model that is frequently used to simulate phase transformation problems in materials research [134, 254, 255]. The classical PF method is formulated based on the theory of Ginzburg and Landau, elaborated in the 1950s [256]. Compared with the sharp interface model, the PF diffusion interface model has the important advantage that no boundary conditions are specified on the interface between the different domains (Figure 3.6). A diffusive order parameter ϕ is a continuous function coordinate of time and space, which indicates each phase to convert between 0∼1 or -1∼1 within a thin translation layer [135, 253]. Moreover, ϕ is controlled by a set of coupled partial differential equations that can be discretized and solved numerically by evolving the equations. Any phase transformation is driven by a reduction of the free energy of the system F, which can be described by a set of conserved c_i and non-conserved ϕ_i field variables. The domain of the model is the entire phase transition system. The free energy of the system consists of the energy contributions from the homogenous bulk phases F_{bulk} and the diffuse interface region F_{int}, according to [134]

$$F(\phi, c) = F_{\text{bulk}} + F_{\text{int}} = \int_V [f_{\text{loc}}(\phi, c) + f_{\text{int}}(\nabla\phi, \nabla c)] \, \mathrm{d}V \tag{3.1}$$

where f_{loc} defines the local free energy density (including chemical, interfacial and elastic strain free energy density), while f_{int} defines the diffusive interface energy density. From the computational point of view, monolithic or staggered algorithms can be computed to solve the problem unknowns, in which mechanical, chemical, interface, and phase-field variables are computed simultaneously or sequentially, respectively. For more details the interested reader is referred to the works in [151, 257, 258]. In those works, robust and efficient monolithic schemes were employed for the numerical implementation.

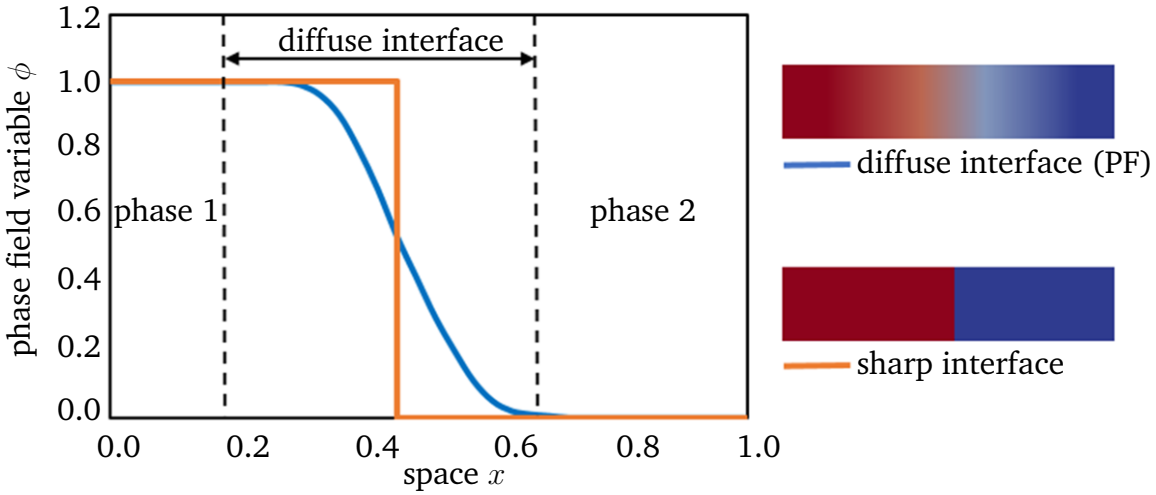

Figure 3.6. Schematic representation of sharp interface model and phase-field model.

3.1.4.1 Evolution Equation

The generalized PF method is represented by the Ginzburg-Landau or Onsager kinetic equation combined with the well fitted Landau- or Redlich-Kister-type free energy density functionals, which are dependent on both conserved and non-conserved field variables [134]. The time-dependent evolution of the conserved field variables (chemical concentration) is defined using a modified

Cahn-Hilliard equation [170], while the Allen-Cahn equation describes the transformations with non-conserved variables (e.g. crystal orientation, long-range order, crystal structure, and elastic strain) [167].

The Cahn-Hilliard equation is

$$\frac{\partial c_i(r,t)}{\partial t} = \nabla \cdot M_{\mathrm{c}} \nabla \frac{\delta F}{\delta c_i(r,t)} \tag{3.2}$$

where c_i is the conserved concentration field variable, M_{c} is the kinetic coefficient of diffusion (associated mobility), t is the time and r is the spatial coordinate, ∇ is a vector of partial derivative operator, and δ denotes the variational derivation of the functional F.

The Allen–Cahn equation is

$$\frac{\partial \phi_i(r,t)}{\partial t} = -L_\phi \frac{\delta F}{\delta \phi_i(r,t)} \tag{3.3}$$

where $\phi_i(r,t)$ are the i different structure field variables with i=1, 2 ..., n, while L_ϕ is the kinetic structure operators (order parameter mobility). Depending on the problem, L_ϕ has different expressions [139, 259, 260].

3.1.4.2 Local Free Energy Function

The local free energy function is a key component in the PF model [176]. This function describes the free energy density of each bulk phase, whose coefficients are obtained from thermodynamic data [259]. The expression of the local free energy depends on the problem of interest. For example, a double-well form is often used for solidification [255, 261]. When dealing with an electromigration problem, a double-obstacle potential is usually applied [15, 262]. A crystalline energy function is used to describe an overlapped dislocation of an elastically anisotropic crystal [263–265]. When the problem is temperature-controlled, as in the melting and solidification processes of crystals, the local free energy function contains a temperature field [266, 267]. In such cases, the phase-field is needed to be coupled with a temperature field [266–270]. Furthermore, a Landau-type polynomial potential can be applied for the treatment of a solid-state phase transformation [271–276]. Table 3.1 summarizes examples of the universal expressions, the graphs of the local free energies and existing phase-field applications.

3.1.5 Phase-Field Modeling of Precipitation Reaction Mechanisms

Self-healing of concrete can be numerically treated as a precipitation process of solutes at the solid–liquid crack interface [277, 278], which is time-dependent and controlled by chemical reactions and diffusion [94, 279]. When the rate of the chemical reactions at the interface is sufficiently high and there is no fluid flow, diffusion will be the only mechanism left for solute transport. The whole process is then a diffusion-controlled precipitation one [278]. However, when the chemical kinetics is slow enough, the precipitation process becomes chemically determined [280]. A review of existing models for self-healing that are based on chemical reactions show that these models are employing a reaction-diffusion process to describe the self-healing evolution [32, 87, 89, 92, 166].

Table 3.1. Expressions, graphs, and applications of the local free energy.

Double-well

$f(\phi) = A\left(-\frac{1}{2}\phi^2 + \frac{1}{4}\phi^4\right); \phi \in (-1, 1),$

where A is the height of the potential energy between the two states at the minimum free energy.

solidification	[15, 24, 135, 173, 255, 260, 261, 281–287]
coarsening and grain growth	[142, 143, 288–290]
dislocation dynamics	[291, 292]
crack propagation	[151–155]
crystal growth under stress	[293, 294]
biological application	[295, 296]
phase transformations in thin films	[297]
electrochemical process	[169, 298–301]

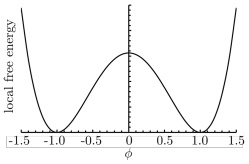

Double-obstacle

$f(\phi) = \psi(\phi) + I_{[-1,1]}(\phi),$

where $\psi(\phi) = A(1-\phi^2)$; $I_{[-1,1]}(\phi) = \begin{cases} \infty & |\phi| > 1 \\ 0 & |\phi| \le 1 \end{cases}$. When the phase transition only occurs in the narrow interface layer $\phi \in (-1, 1)$ instead of in regions outside the interfacial layer.

solidification	[302, 303]
cell dynamical system	[304, 305]
stiffness maximization	[275]
electromigration	[306, 307]

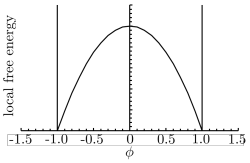

Crystalline energy

$f(\phi) = A\sin^2(\pi\phi); \phi \in (-\infty, +\infty),$

where A is the energy barrier between two neighboring minima. This function is formulated with an infinite number of degenerated minima.

dislocation system	[263, 264, 308, 309]
spiral growth	[265, 310]

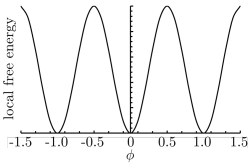

Potential with temperature field

$f(\phi, T) = \frac{1}{8\alpha}(1-\phi^2)^2 - (T_i - T_m)\phi,$

where $T_i - T_m$ is the difference between the current temperature and the melting temperature; α is a positive constant.

solidification	[266–270]

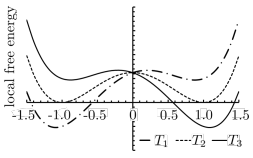

Landau-polynomial

$f(\phi) = f_{dis} + A\phi + B\phi^2 + C\phi^3 + D\phi^4 + E\phi^5 + F\phi^6,$

where f_{dis} is the free energy of the disordered phase; $A \sim F$ are expansion coefficients related to temperature.

solidification	[273, 311–314]
solid-state phase transformations	[271, 272, 315–317]
electrochemical process	[274, 318]
crystal growth under stress	[275]
phase transformations in thin films	[276, 319, 320]

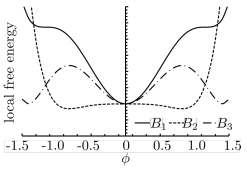

These models focus on two processes: (1) the diffusion mechanism where dissolved ions (e.g., calcium ions) are transferred from the concrete interior toward the surface of the crack, and (2) the precipitation of mineral ions reacting with, for example, carbon dioxide or carbonate ions to form calcium carbonate. They mostly consider how the chemical environment affects the formation of self-healing products and how to achieve agreement with experimental results [32, 87, 89, 94, 98, 108, 166, 210, 321].

However, these models have several limitations. First, they only simulate chemical reactions in solution and do not explicitly account for the change of the initial solid phase boundary due to the dissolution of soluble minerals at the fracture surface. Reaction diffusion models only include precipitation reactions in solution and do not simulate the dissolution reactions of the solid phase with a solution. Second, these models only uniformly simulate the healing process at the crack and do not accurately simulate the change in micro-morphology of the crack. The change in crack morphology is directly influenced by the concentration of aqueous substances and precipitations inside the solution [244]. In return, the change in crack morphology does affects the local concentrations of aqueous substances and precipitations in the solution. This interaction between the two factors is not reflected by existing models.

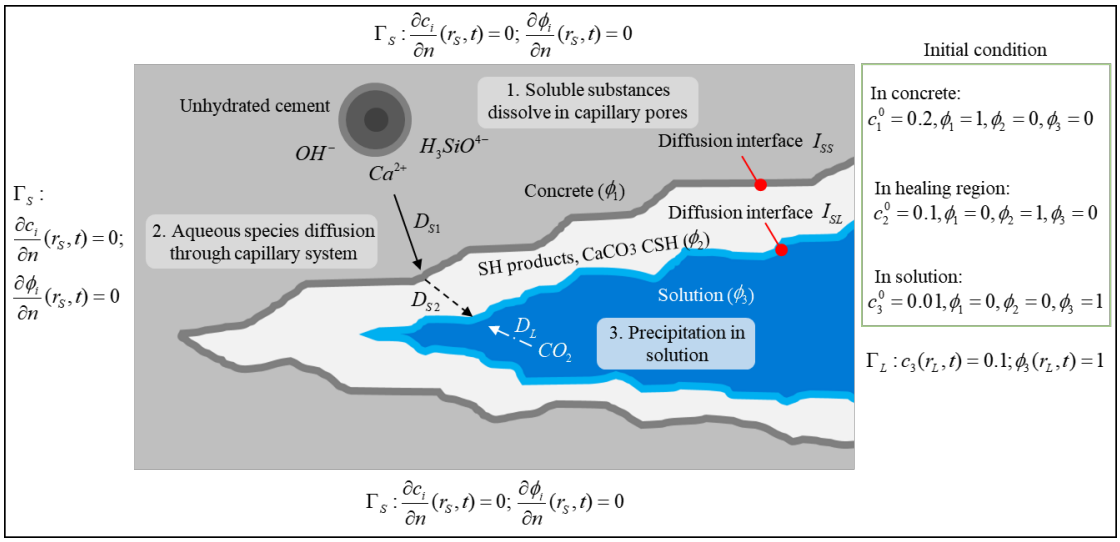

Figure 3.7. Schematic of the phase field model for the autogenous self-healing mechanism. Γ_S and Γ_L are the solid and liquid boundaries with coordinates r_S and r_L, respectively; n is the outward unit normal vector.

A PF method can fill these gaps. Figure 3.7 shows schematically a potential application of a PF model for an autogenous self-healing mechanism. The solid-liquid phase distribution is described by an eigenfunction in the value range [0,1]. The solid phase can be subdivided into an initial solid phase (ϕ_1) and a healing solid phase (ϕ_2), while ϕ_3 represents the solution phase. The solid-solid (I_{SS}) and solid-liquid (I_{SL}) interfaces are simulated continuously. In addition to the solution (D_L), diffusion constants are distinguished between the concrete (D_{S1}) and the healing region (D_{S2}) due to differences in the meso- and microstructures. Neumann boundary conditions (Zero composition flux) were applied at the top, bottom, left and right (the light gray part) boundary for the solute concentration c_i and the order parameter ϕ_i. The Dirichlet boundary condition ($c_3 = 0.1$ and $\phi_3 = 1$) was applied at the right boundary (the blue part). The initial conditions are set based on the

initial concentration in each phase. In this model, we chose to use the diffusion equation instead of Cahn-Hilliard equation because there is no phase separation. The Allen-Cahn equation is applied for solving the order parameter ϕ_i.

This approach can accurately capture information about the alteration of the crack morphology due to solidification by the hydration reactions or the accumulation of precipitates [12, 34, 220].

With this, an overview of the PF approaches to the solute precipitation [24, 322] and precipitation in binary alloys [287, 323, 324] is provided that are instructive for simulating self-healing mechanisms of concrete. The following models are presented in chronological order (Table 3.2).

Table 3.2. PF models for precipitation mechanisms.

Main Application	PF Model	Reference	Feature
Solute precipitation	Xu-Meakin model	[23,321 324-326]	Discontinuity of the solute concentration gradient at the interface
	Noorden-Eck model	[287, 323–325]	Single-phase free boundary problem with dynamic conditions at the moving boundary
Metal precipitation	Wang-Chen model	[286, 326]	Solid-state precipitation controlled by transformation-induced elastic strains
	Rubin-Khachaturyan model	[273, 327]	3D stochastic PF model
	Chen-Ma model	[285, 328]	Kinetic data of existing databases CALPHAD applied into the PF model

3.1.5.1 Solute Precipitation

Solute precipitation is the process at which a solute changes from a liquid phase to a solid phase and precipitates outside its solution [329, 330]. In fact, precipitates are mostly insoluble [331].

(1) Xu-Meakin Model, 2008

Xu and Meakin [24, 322] developed a PF model for studying the dynamics of liquid-solid interfaces due to precipitation and/or dissolution of phases, based on the Karma-Rappel model [260] for pure melt solidifications. Discontinuities in the solute concentration at the interface are explicitly considered. An additional term has been added to the solute diffusion equation to describe the discontinuity of the solute concentration gradient at the interface. In addition, a detailed asymptotic analysis was used to establish a connection between the sharp interface and the PF model by correlating the reaction rate parameter k with the microscopic PF parameters. This ensures that the PF model will converge to the corresponding sharp-interface limit. A modified

solute diffusion equation is built up as follows,

$$\frac{\partial c}{\partial t} = D\nabla^2 c + A_1 \frac{\partial \phi}{\partial t} + A_2 \frac{\partial \phi / \partial t}{|\nabla \phi|} \left(D\nabla^2 \phi - \frac{\partial \phi}{\partial t} \right), \tag{3.4}$$

where the second additional term of the equation is corresponding to the discontinuity the solute concentration gradient at the interface. While the third additional term represents the net source or sink of the solute coming from the discontinuity in the solute concentration across the interface; D is the diffusion coefficient; A_1 and A_2 are two constants, which can be determined by the sharp-interface boundary conditions.

(2) Noorden-Eck Model, 2011

Van Noorden and Eck [287] proposed a PF model for a precipitation and/or dissolution process. The model describes a single-phase free boundary problem with dynamic conditions at the moving boundary. The concentration on the precipitate side of the interface is specified, and the velocity normal to the interface is nonlinear dependent to the concentration on the other side of the interface. The evolution equation of ϕ and c is described according to

$$\frac{\partial \phi}{\partial t} = \frac{1}{\alpha}\Delta\phi - \frac{1}{\alpha\epsilon^2} p'(\phi) - \frac{1}{\alpha\epsilon} \beta k'(\phi) \left[f(c) + f'(c)(c - \rho) \right]; \tag{3.5}$$

$$\frac{\partial c}{\partial t} = D\nabla \left[\nabla c + (\rho - c) \frac{k'(\phi)}{k(\phi)} \nabla \phi \right], \tag{3.6}$$

where $p(\phi)$ is a double-well potential; $f(c)$ is a rate function; $k(\phi)$ is an interpolation function; α, β, D, and ρ are physical parameters; and ϵ is the thickness of an interfacial layer.

Redeker and Rohde [323, 324] extended the Noorden-Eck model by incorporating curvature effects between two fluid phases to simulate precipitation in a porous medium. The model contains two immiscible fluids and one solid phase. Dissolved ions in one of the fluids can precipitate at the pore boundaries. Bringedal et al. [325] considered not only the diffusion of ions in the fluid phase, but also the effect of fluid flow on precipitation.

3.1.5.2 Metal Precipitation

Unlike solute precipitation, metal precipitation occurs in a supersaturated solid solution. Metals and metal oxides exist in the form of crystals. A crystal is a structure in which its atoms or molecules are arranged in an orderly fashion according to certain rules. A crystal is pure when all the components are just a single substance or a compound. If there is another substance involved that occupies the original atomic location and does not destroy the original structure, then this is a solid solution [332]. The original component is equivalent to a solvent and the foreign component is equivalent to a solute. As with a solution, when the solute in a solid solution is supersaturated in the solvent, it can no longer remain stable in the crystal structure and eventually precipitates [333].

The precipitate particles are generally metallic compounds, but may also be formed by aggregation of solute atoms in supersaturated solid solutions in a number of small solute-rich regions [334]. The precipitated particles act as barriers to dislocation movement, allowing significant increase in strength and hardness of most structural alloys of aluminum, magnesium, nickel, and titanium,

as well as some steels and stainless steels [335]. The precipitation mechanisms of different binary and ternary alloys have been intensively studied by using PF models [289, 336, 337].

(1) Wang–Chen Model, 1993

In the earlier study by Wang et al. [286], a PF model based on a microscopic kinetic model and elastic strain theory was developed to study the morphological evolution of the solid-state precipitation, controlled by transformation-induced elastic strain. The free energy of an inhomogeneous solid solution is given by the following equation,

$$F(c) = \frac{1}{2}\sum_{\phi'} W(r-r')c(r)c(r') + k_B T \sum_{r} \left[c(r)\ln c(r) + (1-c(r))\ln(1-c(r))\right] \tag{3.7}$$

where $\phi(r,t)$ is the non-equilibrium single crystal sites of solute atoms, r is the crystal lattice site, $W(r-r')$ is the pairwise interaction energy of two atoms at the lattice site r and r', and k_{B} is the Boltzmann's constant. The drawback of this model is that the matrix phase and the precipitates are iso-structurally treated. However, this assumption does not apply to the simulation of Al-Li alloy precipitation.

(2) Rubin–Khachaturyan Model, 1999

Rubin and Khachaturyan [273] developed a 3D stochastic PF model for simulating the microstructural evolution of Ni-Al superalloys. This model considers the coherency strain in an elastic anisotropic system. The coarse grained stress-free free energy was expressed as

$$F = \int_V \left[\frac{1}{2}\left(\alpha_{ij}\nabla_{ic}\nabla_{jc} + \sum_{p=1}^{3}\beta_{ij}(p)\nabla_{i\phi_p}\nabla_{j\phi_p}\right) + f(c,\phi_1,\phi_2,\phi_3)\right] d^3r \tag{3.8}$$

where α_{ij} and $\beta_{ij}(p)$ are the gradient coefficients, ∇_{ic} and ∇_{jc} denote the gradient terms of multi-composition profile $c(r,t)$, $\nabla_{i\phi_p}$ and $\nabla_{j\phi_p}$ are the gradient terms of multi-component long-range order parameter $\phi(r,t)$, the specific free energy $f(c,\phi_1,\phi_2,\phi_3)$ is approximated by a polynomial, and the second integral term is the total strain energy functional based on the Fourier transform microelasticity method.

(3) Chen–Ma Model, 2004

Chen et al. [285] designed a quantitative PF modeling scheme for multicomponent diffusion-controlled precipitate growth and dissolution in Ti-Al-V system in which the thermodynamic and kinetic data of existing databases CALPHAD was directly inserted into the PF model. The total Gibbs free energy is described as follows,

$$G(T,c,\phi) = \frac{1}{V_{\mathrm{m}}}\int_V \left[G_{\mathrm{m}}(T,c_i,\phi) + \sum_{i=1}^{n-1}\frac{k_i}{2}|\nabla c_i|^2 + \frac{k_\phi}{2}|\nabla\phi|^2\right] \mathrm{d}V. \tag{3.9}$$

where G_{m} is the local molar Gibbs free energy; k_i and k_j are the gradient-energy coefficients for concentration and order parameter inhomogeneities, respectively; V_{m} is molar volume.

The temporal evolution of the composition is governed by Cahn-Hilliard diffusion equation on the basis of the phenomenological Fick-Onsager equations

$$\frac{1}{V_{\mathrm{m}}^2}\frac{\partial c_k}{\partial t} = \nabla\sum_{j=1}^{n-1} M_{kj}\left(T,c_i,\phi\right)\nabla\frac{\delta G}{\delta c_i} \tag{3.10}$$

where M_{kj} are chemical mobilities related to atomic mobilities.

3.1.6 Phase-Field Modeling for Fracture Mechanisms

Fracture mechanics of concrete is a topic of intensive research during the last years. Simulation technology for analyzing crack initiation and propagation in concrete are numerous [213, 338–354]. Besides boundary and finite element methods for linear elastic fracture analysis, different versions of the so called eXtended Finite Element Method (XFEM) are frequently applied [355, 356].

Starting with the works of Bourdin et al. [357] and Miehe et al. [251], fracture processes were modeled explicitly by a PF approach. Due to its simplicity this methodology gained a wide interest and started to be used in the engineering community since 2010. From there on many scientist have worked in this field and developed PF approaches for finite elements methods (FEM), isogeometirc analysis (IGA), and recently also for the virtual element methods (VEM). The main driving force for these developments is the possibility to handle complex fracture phenomena within numerical methods in various dimensions. Thus, research on PF approaches is still actual and points in many different directions.

In this review article, the simulation of fracture processes in concrete is achieved by utilizing the continuum PF method, which is based on the regularization of sharp crack discontinuities. This avoids the use of complex discretization methods for crack discontinuities and can account for multi-branched cracks within a solid skeleton (e.g. hydrated cement paste, unhydrated clinker particles, and stones). In particular due to the over-complicated geometry and content of concrete at multi-scales, in Figure 3.8 an example for PF modeling of water-induced failure mechanics in concrete microstructure is presented. In recent years, several brittle [358–395] and ductile [257, 396–423] PF fracture formulations have been proposed in literature. These studies range from modeling 2D/3D small and large strain deformations, variational formulations, multi-scale/physics problems, mathematical analysis, different decompositions and discretization techniques with many applications in science and engineering. All these examples demonstrate the potential of PF method for crack propagation.

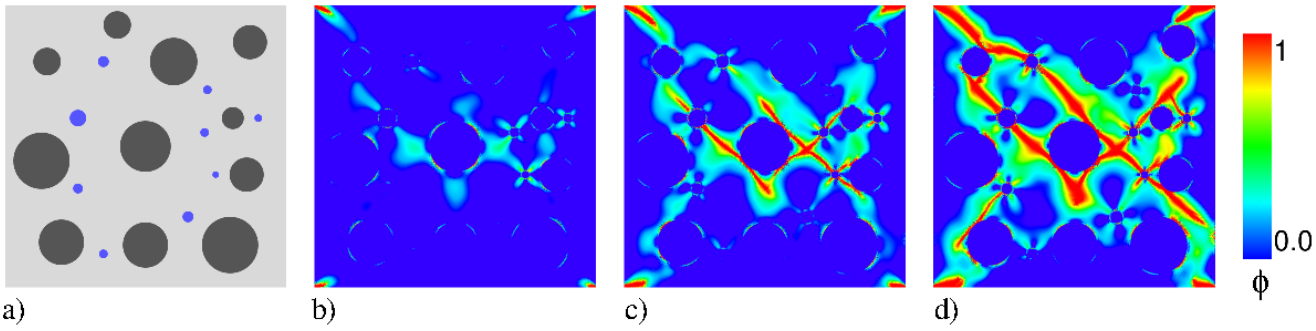

Figure 3.8. Concrete failure in poro-elasto-plastic media. (a) Schematic of the concrete idealized microstructure: Light gray color refers to the hydrated cement paste, dark gray color stands for the unhydrated clinker particles, and blue color depicts the water content. (b-d) Evolution of crack phase-field ϕ for different deformation states up to final failure, as outlined in [258].

The aforementioned PF approaches consider the fracture behavior of concrete, i.e. as a crack initiation and propagation. However, an important aspect in concrete is the treatment of the crack-closure effects. This response was firstly investigated in the works [424, 425] for fatigue

crack closure under cyclic tension. Thereby, the results indicate a fatigue crack, propagating under zero-to-tension loading may be partially or completely closed at zero load. A review of this physical phenomena can be seen in [426–428]. To the author's best knowledge, a PF approach for modeling crack closure is still an open issue. To this end, cohesive elements along the crack path will be coupled with the PF formulations to prevent overlapping of the crack faces. Another future direction is to use a contact scheme at the crack faces similar to the work developed by [429]. A further important aspect is the PF modeling of crack-closure induced by a self-healing mechanism (introduced in Section 3.1.3) in cementitious systems. These topics await investigation.

3.1.6.1 Fundamental Variational Formulations

In Griffith-type fracture formulations, the mechanical deformation denoted generally by "state" and the sharp crack surface Γ in a brittle elastic solid (e.g. cement paste) are determined by the incremental minimization problem developed by Francfort and Marigo [430] as

$$E(state, \Gamma) = \int_{V \setminus \Gamma} f(state)\, dV + G_c\, \mathcal{H}(\Gamma) \rightarrow \text{Min!} \tag{3.11}$$

where G_c is the Griffith critical surface energy release and $\mathcal{H}(\Gamma)$ is the Hausdorff surface measure of the crack set Γ. In Equation (3.11), the functional E has a structure identical to that for image segmentation developed by Mumford and Shah [431]. It consists of the strain energy stored in the solid as well as the energy release due to fracture.

3.1.6.2 Regularized Variational Theory

The numerical evaluation of the sharp crack interface in the functional E (Equation 3.11) is not suitable within a standard finite element framework, as outlined in the work of Bourdin et al. [357]. Therefore, a regularized crack interface using a specific regularization profile γ is introduced in the studies of Miehe et al. [251, 396]. It is based on a geometric regularization of sharp crack discontinuities that is governed by a crack PF

$$\phi \in [0, 1] \quad \text{with} \quad \dot{\phi} \geq 0 \tag{3.12}$$

It characterizes locally for the initial condition $\phi = 0$ the unbroken and for $\phi = 1$ the fully broken state of the material. Thus, the critical fracture energy is approximated by

$$G_c\, \mathcal{H}(\Gamma) \approx \int_V G_c\, \gamma(\phi, \nabla\phi)\, dV \quad \text{with} \quad \gamma(\phi, \nabla\phi) := \frac{1}{2\, l_f}\, \phi^2 + \frac{l_f}{2}\, |\nabla\phi|^2 \tag{3.13}$$

in terms of the crack surface density function per unit volume of the solid. The regularization is governed by a fracture length scale l_f. Note that the limit for vanishing the fracture length scale $l_f \rightarrow 0$ gives the sharp crack surface Γ.

Therefore, the minimization problem represented by Equation (3.11) can be expressed in the following form,

$$\widetilde{E}(\text{state}, \Gamma) = \int_V \widehat{W}(\text{state}, \phi, \nabla\phi)\, dV \rightarrow \text{Min!} \tag{3.14}$$

defined in terms of the total work density function $\widehat{W}$ as

$$\widehat{W}(\text{state}, \phi, \nabla\phi) = g(\phi)\, f(\text{state}) + G_c\, \gamma(\phi, \nabla\phi) \ , \tag{3.15}$$

contains a degraded elastic work density and the crack energy release per unit volume. $g(\phi)$ is a degradation function defined as $g(\phi) = (1-\phi)^2$. It describes the degradation of the solid with the evolving crack phase-field ϕ, as depicted in Figure 3.8b–d.

3.1.7 Discussion and Conclusions

Based on the above literature review, it can be observed that PF methods have a great potential for simulating self-healing mechanisms in concrete. Therefore, it can be applied to solve problems that cannot be addressed by commonly applied models. It has the potential of an unprecedented breakthrough. As self-healing of concrete is a rather complex process, it is an interaction between physical, chemical and mechanical mechanisms. Obtaining a novel, versatile model for self-healing concrete is a multidisciplinary study involving civil engineering, materials science, and chemistry. Many studies have been conducted in these fields using the PF approach, while it will be a great reference for the development of a self-healing PF model.

In future research, it would be recommended to include in the polynomial system of the PF approach the pore structure, concrete matrix, water dissolution, and hydration product phases at the crack front. In this way, the free-energy equations will combine hydration kinetics, crystallization kinetics, polymerization reaction kinetics, mass transport and chemical energies to provide a detailed description of the phase nucleation and growth mechanisms at the crack front. Coupling a reactive PF model with a fracture PF model allows to simulate the crack development and its mechanical self-healing recovery effects at different stages and under different environmental conditions. In order to achieve this goal, there are several self-healing mechanisms that need to be studied in great detail. Validating these models should be continuously done by comparing them with experimental results. The following potential future steps are identified:

(1) Evolution of the pore structure at the crack surface:

During the process of autonomous self-healing, soluble substances at the crack surface enter the solution and undergo various dissolution reactions, followed by hydration and carbonation crystallization reactions. Part of the solution will diffuse into the capillary pores of the concrete matrix, where crystallization and precipitation also occur. The growth of the cracked surface also forms a new pore structure, which further affects the diffusion and chemical reaction processes. Thus, the pore structure of the crack boundary is constantly changing with ongoing reaction. Its interaction with the crack morphology, reactant concentration, and mass transport needs to be investigated in the future.

(2) Influencing factors and simulations for mechanical repair of cracks:

The fracture PF part is a combination of elastic and fracture energies. Elastic free energy will follow the classical assumptions while the fracture part will account for the fracture toughness, order formulation, evolution equations, and healing regain laws. Moreover, both are closely related to the packing density field. This is because the mechanical properties at fracture mainly depend on the solid-phase continuity. The mechanical properties are enhanced in a homogeneously dense position of the filler and, conversely, worse in the disconnected parts of

the solid phase. The packing density field, in turn, is related to the mass transport. Therefore, a numerical transport–mechanical coupling strategy shall be developed to simulate the overall performance of the self-healing mechanism.

(3) Evolution of crack healing morphology:

The morphology of the crack greatly influences its local healing effect. At the crack tip, healing products are produced faster and more frequently because of the higher concentration of reactants. The movement of the crack tip is faster than at other locations. Thus the crack morphology changes continuously with the healing process. As the PF model avoids tracking the boundary conditions at the interface and instead simulates the evolution of the auxiliary field. Therefore, the evolution of the interfacial morphology is easier to simulate. In addition, the simulation of interfacial morphology will take into account the distribution of bacteria, adhesive agents and mineral admixtures. Therefore, the macroscopic representation of a crack healing morphology shall be simulated from a micro-level point of view.

(4) Free energy to distinguish between various product phases:

Self-healing products contain multiple substances (CSH, CH, or additional byproducts) that, although they have the same healing mechanism (aggregation, crystallization and precipitation), their chemical reaction kinetics are different. This affects the rate of healing of the cracks as a whole. Therefore, the free energies of the various product phases and the corresponding thermodynamic parameters will be distinguished in the future and reflected in specific simulations.

(5) Determination of PF parameters:

A formulation for the determination of the PF parameters needs to be provided. Information on the PF parameters and their interrelationships will be obtained from thermodynamic and diffusion databases in combination with experimental data. Combined with the second law of thermodynamics and non-equilibrium thermodynamics, the self-diffusion, mutual diffusion, and chemical diffusion coefficients will be related to the diffusion mobility (M). The order parameter mobility (L) will be derived and their relationship to other phase-field parameters will be investigated.

(6) Development of a three-dimensional model:

As a self-healing process includes complex physical-chemical-mechanical processes, these mechanisms can only be accurately simulated in a fully three-dimensional system. Therefore, a three-dimensional simulation of the self-healing process need to be performed with realistic boundary conditions. The simulation results need to be verified and compared with 3D computed tomography scan (CT scan) results of concrete specimens.

In conclusion, the use of a PF method is feasible and has a significant application advantages in the field of self-healing concrete applications. Although this method still has a long way to go before it becomes a fully fledged simulation tool, these early studies are considered to be an important step towards reaching this goal.

3.2 Publication 2: Numerical Phase-Field Model Validation for Dissolution of Minerals

Sha Yang[1], Neven Ukrainczyk [1], Antonio Caggiano[1,2] and Eddie Koenders[1]

1 Institute of Construction and Building Materials, Technical University of Darmstadt, Franziska-Braun-Straße 3, 64287 Darmstadt, Germany

2 CONICET and LMNI-FIUBA, Universidad de Buenos Aires, Buenos Aires C1127AAR, Argentina

Journal: Appl. Sci. 2021, 11(6), 2464; https://doi.org/10.3390/app11062464

3.2.1 Introduction

Mathematical modelling of the moving-boundary dissolution fronts of minerals is important in a wide range of engineering technologies. For example, it is of great importance in fields of geochemistry, materials science, hydrometallurgy, etc. Predictions of the moving boundary dissolution phenomena can support in the design of engineering processes where dissolution is desired: e.g. in extraction of elements or reactivity of cementitious minerals, but also when not desired, e.g. in durability (corrosion) issues of building materials (e.g. steel-reinforced concrete frames). In general, minerals dissolve when exposed to aggressive solution environments and form leached layers of varying density and strength [432]. This in turn affects the mechanical and transport properties of the microstructure which further may be relevant at higher scales, for example when the material (rock, concrete or mortars) has structural applications. In addition, the dissolution mechanisms of some special minerals can be of great industrial and environmental interest. For example, the dissolution of scorodite is considered a potentially good carrier for arsenic fixation [433]. Moreover, the application of innovative self-healing concrete in civil engineering has been extensively and intensively studied in recent years. The disdissolution of $Ca(OH)_2$ from the concrete matrix is one of the key processes of the durability and self-healing mechanisms [12, 13, 221].

The dissolution of minerals often involves complex physico-chemical processes at the solid–liquid interface. However, this can be simplified at the mesoscale to the problem of a continuously moving boundaries. Traditional sharp interface models are thus required to trace these moving fronts [434–444]. However, this becomes extremely difficult for high-dimensional problems, with complex dynamic geometries, especially those whose interface evolution is accompanied by energy changes. In this sense, phase-field (PF) methods provide a powerful way to track such interfaces. The PF method has been applied to various phenomena in materials science area, such as, solidification, solid-state phase transformation, recrystallization, grain growth, fracture, and electromigration [285, 298, 309, 445–447].

Generally speaking, the PF model can be regarded as a kind of diffusion interface model [15, 139, 211], which assumes that the thickness of the interface is limited, while the physical properties on the interface are continuous and smooth [253, 314]. The moving solid–liquid interface can thus be accurately tracked [136]. Compared with sharp interface models, the PF diffusion interface model has the important advantage that no boundary conditions are specified on the interface between different domains [134, 177]. This allows us to study the evolution of arbitrarily complex morphology without tracking the microscopic shape of the grain [448, 449]. A new variable,

namely the order parameter, is required to represent the ordered numbers of materials in terms of time and position [173, 281]. In these works, the complex interfacial spatial-temporal evolution has been investigated through the aforementioned order parameter in an implicit way. An additional feature of the PF method is that there is a functional total free energy that can characterize the nature of the phase transition. It includes the various energy contributions of the system at the non-equilibrium state: i.e. chemical energy [450–453], electric potential energy [158, 454, 455], stress energy [358, 360, 363], etc. It is the competition between these different energies that leads to the generation of changing microstructural topography during the phase transition. In solving the PF model, conservative fields such as concentration fields can be described e.g. through the Cahn–Hilliard equation [170], while non-conservative fields, as order parameters, can be described via the Allen–Cahn one [167].

There are four models in the literature that are most commonly used to address two or multi-phase transition processes. They provide important insights into solving of the mineral dissolution problems: the Wheeler-Boettinger-McFadden (WBM) model [177, 178], the Kim-Kim-Suzuki (KKS) model [1], Steinbach model [176] and Losert model [456]. The WBM model is derived in a thermodynamically consistent way, which is based on an assumption that each point of the interface is a mixture of coexisting phases with the same composition but different volume fractions [314]. This model works under both sharp-interface condition and finite-interface thicknesses [185, 186]. However, the larger interface thickness will lead to unreliable calculation results [179, 183, 457]. KKS model shows a different definition of the free energy density, which defines the interface as a mixture of liquid and solid phases of different compositions, but with the same chemical potential [185]. For the KKS model, the relationship between model parameters and material properties can be established through the equilibrium and thin interface limit analysis [1]. The Steinbach model is not based on the thermodynamic treatment, but based on the geometric description of interface through the innterpolating function of interface curvature. This model is more suitable for a dilute alloy [270]. Losert et al. [456] finally used the similarity of alloys and pure materials to expand the thin interface model by matching variables in pure materials. However, there are two strict assumptions in the model that limit its application (1) the liquidus and solidus lines need to be parallel, and (2) the diffusivity of the solute is constant in the entire region [458].

In applying the PF model, described above, to the moving boundary problem of minerals, it is necessary to understand how to select the interface mobility so that the model can effectively describe the dissolution process. In the literature, there are only a few studies that address this issue. Qin and Bhadeshia [259] proposed that, in a single-component system, the interface mobility is related to the interface velocity and the driving force according to the chemical rate theory. In the case of spinodal decomposition, the interface mobility can be obtained from the diffusion coefficient and thermodynamics. When the model is used to simulate the complex meso-morphological evolution, the interface mobility needs to be determined based on experiments, as also demonstrated in this paper (Section 3.2.6.3). Karma and Rappel [139] made a linear approximation of the temperature gradient at the interface and proved that in dealing with the solidification problem of pure melting, the PF parameters can be accurately determined under the thin interface limit. Based on this model, Xu and Meakin [24] developed a phase-field approach for aqueous dissolution/precipitation reactions assuming first order reaction kinetics. The model was validated by a one-dimensional analytical solution of interface motion due to solute precipitation. Two additional terms were added to the diffusion equation, one corresponding to the discontinuity of the solute concentration gradient, at the interface, while the second one represents the net source (or sink) of the solute, coming from the discontinuity in the solute concentration across

the interface. In most of the studies, the values of interface mobility are used as empirical or hypothetical ones [168, 172, 459–463]. Furthermore, few attempts have been made to explain in detail the calculation of the interface mobility and its relation to other physical parameters [182, 185, 303, 464, 465]. Therefore, tackling of this difficulty will be one of the innovations of this paper.

In contrast to the reaction kinetics controlled case, here we further validate the PF approach on the experimental results (of NaCl dissolutions) and are focusing mainly on the diffusion limited mechanisms. First, the one-dimensional diffusion-controlled dissolution problem will be simulated using an analytical solution and the classical KKS model, separately. The results will then be compared to clarify the estimation and interaction of the interface mobility with other PF parameters. The effect of solid particle shape on the dissolution process is 2D analysed and validated on literature data for NaCl dissolutions. The PF results are then validated against the data obtained from analysis by the video-microscopy images and compared with the analytical model. Finally, a concluding discussion on the whole article is given.

3.2.2 Dissolution Mechanisms

3.2.2.1 Types of Dissolution

Chemical dissolution of minerals occurs as a congruent or an incongruent reaction, depending upon the type of a mineral [466]. Congruent dissolution of a solid mineral is a chemical reaction which completely dissolves the mineral and all products of this reaction are dissolved species. An obvious example would be calcite $CaCO_3$ and NaCl [467, 468]:

$$\mathrm{A_aB_b(s)} \rightarrow \mathrm{aA(aq)} + \mathrm{bB(aq)} \tag{3.16}$$

when the primary solid phase is altered and at the same time a secondary solid phase is formed, incongruent dissolution occurs, for example the alteration of albite to gibbsite $NaAlSi_3O_8$, or Kaolinite [469, 470], which requires a more advanced thermodynamic modelling approaches to be integrated in the PF:

$$\mathrm{A_aB_b(s)} \rightarrow \mathrm{cC(s)} + \mathrm{dD(aq)}. \tag{3.17}$$

3.2.2.2 Diffusion-Controlled Dissolution Mechanisms

Figure 3.9 shows the dissolved diffusion process of soluble minerals based on the diffusion interface. When dealing with the problem of moving boundaries, the conventional approach separates the different phases by a sharp interface. The interface movement is solved by a partial differential equation describing, for example, mass and thermal diffusion equations. These equations have to be combined with boundary conditions of varying values and positions. When some variables (heat flux or concentration) cross the sharp interface, jump discontinuities can occur, making the calculation very difficult. In the PF model, the interface is described as a diffuse interfacial layer with smooth transitions. Thus, the phase transformation is represented by a change in an order parameter (ϕ). As shown in Figure 3.9, the solid phase is represented by “1” while the liquid phase by “0”, hence the order parameter varies continuously between 0 and 1 at the solid–liquid interface.

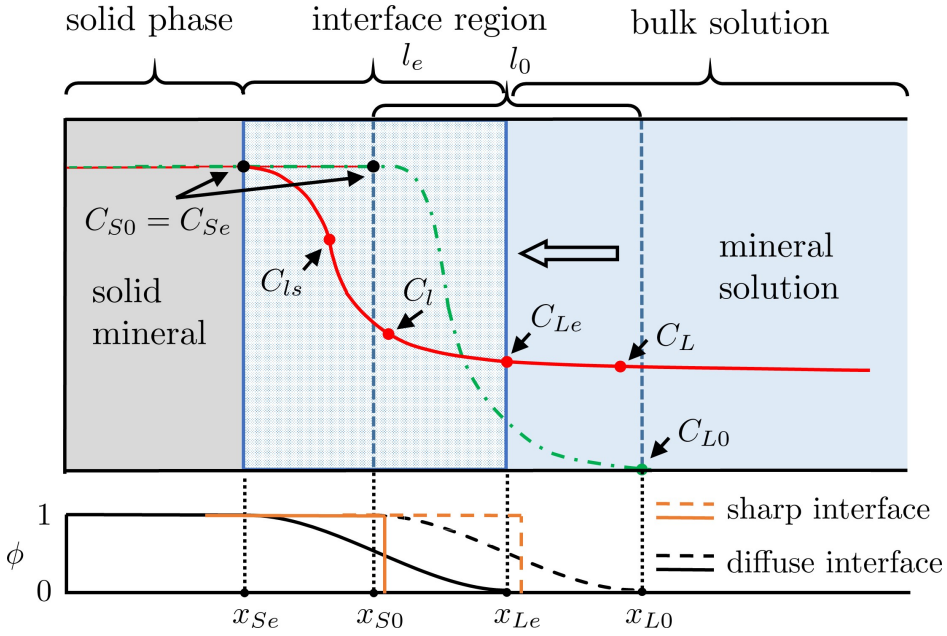

Figure 3.9. Schematic representation of solute concentration of soluble minerals in situ (i.e. green dotted line) and equilibrium states (i.e. red solid line), and the phase transformation within a diffuse and sharp interface, respectively. For the sharp interface, the evolution of the solute concentration is discontinuous at the interface. However, for the diffuse interface, the solute concentration evolves continuously between their equilibrium values at the mineral (c_{Se}) and solution boundary (c_{Le}).

As the congruent dissolution process occurs, the solute is gradually transferred into the solution, the length of the solute base phase decreases, and the solid–liquid diffuse interface gradually moves toward the inside of the solute base phase. The solute concentration in the initial solution is c_{L0}, while the solute concentration at equilibrium is c_{Le}. The solute concentration in the solid is kept constant when the diffusion phenomenon in the solid is not taken into account. The change of solute concentration in solution with time is related to its position. The solute concentration (c_{L}) increases with time away from the solute matrix phase; solute concentration (c_{ls}) decreases with time near the solute matrix phase. The solute concentration in between (c_{l}) is in a state of dynamic increase or decrease. x_{Se}, x_{S0}, x_{Le} and x_{L0} indicates the positions corresponding to the above solute concentrations.

3.2.3 Mathematical Methods

3.2.3.1 Analytical Solutions

A following 1D planar analytical description of a diffusion-controlled dissolution for phase transformation is considered, where the solid is immersed in a (semi-)infinitive liquid solution. The diffusion equation is a parabolic partial differential equation, which is expressed as follows:

$$\frac{\partial c(x,t)}{\partial t} = D_{\mathrm{L}} \nabla^2 c(x,t), \tag{3.18}$$

where D_{L} is the diffusion coefficient, $c(x,t)$ is the concentration at location x and time t, subject to the conditions:

$$c|_{\mathrm{x=R,\,t}} = c_{\mathrm{Le}}(0 < t \leq \infty), \tag{3.19}$$

$$c|_{\mathrm{x,\,t=0}} = c_{\mathrm{L0}}(x \geq R), \tag{3.20}$$

where $x = R$ is the position at the solid-liquid interface, c_{L0} and c_{Le} represents the initial concentration and the equilibrium concentration of one component in the liquid phase.

At the solid–liquid interface, the following independent flux balance condition must be fulfilled:

$$(c_{\mathrm{S}} - c_{\mathrm{Le}})\frac{dR}{dt} = D_{\mathrm{L}}\frac{\partial c}{\partial x}|_{\mathrm{x=R}}, \tag{3.21}$$

where c_{S} is the concentration in solid phase which is taken as a constant.

The exact analytical solution for the field is [434]:

$$c(x,t) - c_{\mathrm{M}} = (c_{\mathrm{Le}} - c_{\mathrm{L0}})\frac{\mathrm{erfc}\left[(x - R_0)/2\sqrt{D_{\mathrm{t}}}\right]}{\mathrm{erfc}(-\lambda)}. \tag{3.22}$$

The interface position at current time can be expressed as

$$R = R_0 - \lambda_{\mathrm{I}}\sqrt{D_{\mathrm{t}}}, \tag{3.23}$$

where R_0 denotes the value of R at the time $t = 0$, while

$$\lambda_{\mathrm{I}} = 2\lambda, \tag{3.24}$$

where λ is given by:

$$\sqrt{\pi}\lambda\mathrm{exp}(\lambda^2)\mathrm{erfc}(-\lambda) = \beta/2, \tag{3.25}$$

where $\beta = 2(c_{\mathrm{Le}} - c_{\mathrm{L0}})/(c_{\mathrm{S}} - c_{\mathrm{Le}})$.

Different from the planar solid where exact solution is available, only approximately analytical solution model for the diffusion-controlled dissolution of the spherical solid has been found. The stationary-interface approximation is expressed as [434]:

$$c(x,t) - c_{\mathrm{M}} = \frac{(c_{\mathrm{Le}} - c_{\mathrm{L0}})R}{x}\mathrm{erfc}\left[\frac{x - R}{2(D_{\mathrm{L}}t)^{1/2}}\right], \tag{3.26}$$

where the current interface position is $R^2 = R_0^2 - \beta D_{\mathrm{L}}t$; β as defined in Equation 3.25.

The implicit expression for the particle radius ratio y ($y = R/R_0$) with respect to time is defined as follows:

$$\ln\left[y + 2p(\tau)^{1/2}y + \tau\right] + \frac{2p}{(1-p^2)^{1/2}}\arctan\left(\frac{(1-p^2)^{1/2}}{\frac{y}{\tau^{1/2}} + p}\right) = 0, \tag{3.27}$$

where,

$$\tau = \frac{\alpha t}{R_0^2}, \tag{3.28}$$

$$\alpha^2 = \beta D_{\mathrm{L}}, \tag{3.29}$$

$$p^2 = \frac{\kappa}{4\pi}. \tag{3.30}$$

3.2.3.2 The Phase-Field (PF) Method

The total free energy of the thermodynamic system drives changes in the micro-structure of materials only when the total free energy changes from a high chemical potential (or a higher free energy) state to a low chemical potential (or a lower free energy) state to eventually attain an equilibrium. The total free energy of the system is a function of the solute concentration c and the phase parameter ϕ and expressed as:

$$F(c,\phi) = F_{\text{loc}} + F_{\text{int}} = \int_V \left[f_{\text{loc}}(c,\phi) + \frac{\kappa}{2}|\nabla\phi|^2 \right] \mathrm{d}V, \tag{3.31}$$

where F_{loc} is the local free energy of the system, F_{int} is the interfacial energy, and κ is the gradient energy coefficient. In order to simplify the numerical calculation, the molar concentration of the solute is normalized by the molar concentration of the solid c_{S}, that is, $c = c'/c_{\text{S}}$. The molar concentration of the solid is defined as the density of the solid divided by its average molar mass [471]. Each point in the entire domain is a mixture of two phases with different chemical compositions. The Gibbs free energy expression, in the KKS model, has been widely employed in solidification mechanisms of binary alloys [472, 473], in addition to the recent extension to the field of electrochemical corrosion [182, 459]. The mechanism of the corrosion reaction is similar to that of the dissolution reaction, i.e. both are phase transformations triggered by the diffusion of ions. Hence, the double well potential (i.e. Gibbs free energy density) has two minima at $\phi = 0$, $\phi = 1$ and a maximum at $\phi = 0.5$ (middle of the interface). Based on this theoretical basis, the present model identifies the local free energy $f_{\text{loc}}(c,\phi)$ as a fractionally weighted average of the solid $f_{\text{S}}(c_{\text{S}})$ and liquid free energies $f_{\text{L}}(c_{\text{L}})$, and imposes a double-well potential $\omega g(\phi)$ as follows:

$$f_{\text{loc}}(c,\phi) = h(\phi) f_{\text{S}}(c_{\text{S}}) + [1 - h(\phi)]\, f_{\text{L}}(c_{\text{L}}) + \omega g(\phi), \tag{3.32}$$

where the interpolation function $h(\phi)$ is built as $h(\phi) = -2\phi^3 + 3\phi^2$, and ω is the height of the double-well potential function given by $g(\phi) = \phi^2(1-\phi)^2$.

The free energy density of the solid and liquid phase is approximated by a parabolic function with the same curvature A as follows:

$$f_{\text{S}}(c_{\text{S}}) = A(c_{\text{S}} - c_{\text{Se}})^2, \tag{3.33}$$

$$f_{\text{L}}(c_{\text{L}}) = A(c_{\text{L}} - c_{\text{Le}})^2, \tag{3.34}$$

where $c_{\text{Se}} = c_{\text{S}}/c_{\text{S}} = 1$ and $c_{\text{Le}} = c_{\text{sat}}/c_{\text{S}}$ are the solute concentrations at the normalized equilibrium of the solid and the liquid phase, respectively.

Complementary condition indicates that the phase concentrations are constrained such that the chemical potentials of each phase are equal:

$$\frac{\partial f_{\text{S}}(c_{\text{S}})}{\partial c_{\text{S}}} = \frac{\partial f_{\text{L}}(c_{\text{L}})}{\partial c_{\text{L}}}. \tag{3.35}$$

The solute composition in the interface area is the fraction-weighted average of the liquid and solid composition, and the same formula is used for the diffusion coefficient, as shown below:

$$c = h(\phi) c_{\text{S}} + [1 - h(\phi)]\, c_{\text{L}}, \tag{3.36}$$

$$D = h(\phi)D_{\mathrm{S}} + [1 - h(\phi)]\, D_{\mathrm{L}}. \tag{3.37}$$

The interfacial evolution is controlled through coupled conserved and non-conserved dynamics. Particularly, the Allen-Cahn equation is used to describe the temporal evolution of the non-conserved variable ϕ. However, the diffusion equation is applied for solving the evolution of the conserved parameter c:

$$\frac{\partial \phi(x,t)}{\partial t} = -L\frac{\delta F}{\delta \phi} = -L\left[\frac{\partial f(\phi)}{\partial \phi} - \kappa\Delta\phi\right], \tag{3.38}$$

where L is the PF mobility:

$$\frac{\partial c(x,t)}{\partial t} = D\nabla^2 c(x,t), \tag{3.39}$$

where D is the diffusion coefficient.

The energy of the system is minimal when it reaches equilibrium. In order to find the PF profile $\phi_0(x)$ and the composition $c_0(x)$ at equilibrium state, Kim, et al. [1] deduced a one-dimensional solidification problem with boundary conditions $\phi_0|_{\mathrm{x}\to-\infty} = 1$ (solid) and $\phi_0|_{\mathrm{x}\to+\infty} = 0$ (liquid). Since the equilibrium state means the vanishing of the driving force, the PF profile $\phi_0(x)$ should satisfy the following Equation:

$$\frac{\delta F}{\delta \phi_0} = \frac{\partial f(\phi_0)}{\partial \phi_0} - \kappa\Delta\phi_0 = 0. \tag{3.40}$$

Thus, by combining with the double well equation, the PF profile can be expressed as:

$$\phi_0(x) = \frac{1}{2}\left[1 - \tanh\left(x\sqrt{\frac{\omega}{2\kappa}}\right)\right]. \tag{3.41}$$

Then, the composition is:

$$c_0(x) = h(\phi_0(x))c_{\mathrm{S}}^e + [1 - h(\phi_0(x))]\, c_{\mathrm{L}}^e. \tag{3.42}$$

3.2.4 Problem Description and Model Tests

In this section a 1D congruent dissolution case study is presented selected as benchmark for verifying the soundness and capability of the proposed PF procedure.

3.2.4.1 Benchmark with Analytical Model for One-Dimensional (1D) Congruent Dissolution

The model consists of a one-dimensional domain with a size of 20 mm. The solid and liquid domains have a 3:17 ratio (see Figure 3.10). This is chosen to ensure that the length of the solution must be long enough for diffusion to take place in a system whose domain is considered to be semi-infinite.

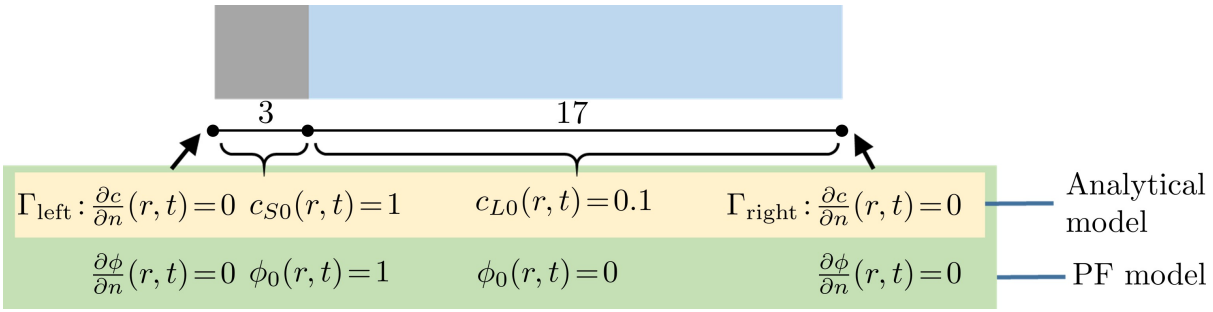

Figure 3.10. Initial benchmark configurations and boundary conditions for 1D single-component dissolution of a planar solid.

In the initial aqueous solution concentration c_{L0} is specified as 0.1 mol/m^3. The concentration c_{S} of the solid was constant at 1 mol/m^3. The equilibrium concentration c_{Le} was maintained at 0.4 mol/m^3 at the fluid-solid interface. The diffusion coefficient of the solute in the liquid D_{L} is taken as 1.0×10^{-9} m^2/s, while the diffusion of the solute in the solid D_{S} is 1.0×10^{-15} m^2/s. Neumann conditions (zero flux) were applied on the right and left side of the domain boundary. The parameters used in this study and their values are listed in Table 3.3.

Table 3.3. Summary of benchmark parameters.

Parameter	Description	Value	Unit
ΔG	Gibbs free energy	2233.23	J/m^3
A	curvature of the free energy density function	6.20×10^{3}	J/m^3
ω	height of the double well potential	1.94×10^{4}	J/m^3
L	interface mobility	4.02×10^{-5}	m^3/(J ·s)
κ	gradient energy coefficient	1.12×10^{-5}	J/m
l_0	initial thickness of the diffuse interface	1.0×10^{-4}	m
σ	interfacial energy	1.1×10^{-1}	J/m^2
D_{L}	diffusion coefficient in solution	1.0×10^{-9}	m^2/s
D_{S}	diffusion coefficient in solute	1.0×10^{-15}	m^2/s
c_{Se}	saturation concentration in the solid phase	1.0	mol/m^3
c_{Le}	saturation concentration in the solution	4.0×10^{-1}	mol/m^3
R	gas constant	8.31	J/(K ·mol)
T	ambient temperature	2.93×10^{2}	Kelvin
K	equilibrium constant	0.4	[-]
t	calculation time	2.88×10^{4}	s

3.2.4.2 Simulation Case Study Based on Available Measured Experimental Data of Mineral Particle Dissolution

Most of the available experimental data on solid dissolution in the literature focus on recording the evolution of solute concentration [439, 442, 474, 475] or dissolved solid mass over time, and do not explicitly observe the movement of the solid–liquid boundary [474, 475]. In some experiments, the dissolution process was influenced by convection with stirring [476–479]. In this sense, sodium chloride (NaCl) is one of the most common minerals: its congruent dissolution mechanism and the corresponding reaction thermodynamics and kinetics are well documented in the literature [468, 480–485]. However, studies addressing solid–liquid boundary regression due to diffusion-controlled dissolution have mainly tended to focus on the nanoscale [486–488].

The study of Quilaqueo and Aguilera [118] is one of the few studies that provides detailed experimental dataset to be used for the experimental validation of the PF numerical models. They performed image analysis by coupling a digital camera to a stereo microscope to obtain microscopic images of the dissolution process. Recording started by placing a single NaCl particle in 500 µL of water without stirring at 20°C. The time profile of dissolution was obtained by calculating the projected area of the single crystal as a function of dissolution time from the video microscope image.

Based on these experimental data, one-dimensional simulations of the dissolution process of a single salt particle performed, in a spherical coordinate system, and two-dimensional simulations of the dissolution process of three different shapes of NaCl particles, namely round, ellipsoidal and irregular, have been performed by using the PF model. Neumann no-flux boundary conditions are applied for 1D simulation. Periodic boundary conditions are used for 2D simulations. The thin interface limit is supported by the chosen experimental case of the highly soluble mineral crystals, which can be considered as non-porous. This results in negligible solid-liquid thickness (at the mesoscopic scale) and it has been considered in this paper. The employed parameters are summarized in Table 3.4. For easier implementation of energy equations at microscale, all length dimensions were normalized by the solution radius and energy terms normalized by A (see Appendix A4).

Table 3.4. Model parameters for diffusion-controlled NaCl dissolution.

Parameter	Value	Unit	Ref.	Parameter	Value	Unit	Ref.
ΔG	5.15×10^{5}	J/m^3		D_{L}	1.68×10^{-9}	m^2/s	[489, 490]
A	5.17×10^{5}	J/m^3		D_{S}	1.68×10^{-15}	m^2/s	
ω	1.51×10^{5}	J/m^3		c_{solid}	3.70×10^{4}	mol/m^3	[118]
L	4.11×10^{-3}	m^3/(J ·s)		p	357 - 360	g/L	[491, 492]
κ	1.44×10^{-6}	J/m		r	6.41×10^{-4}	m	[118]
l_0	1.28×10^{-5}	m		t	5×10^{2}	s	[118]
σ	1.10×10^{-1}	J/m^2	[489]				

3.2.5 PF Modelling Methodology and Numerical Implementation

3.2.5.1 Summary of Modelling Assumptions

In the analytical solution and the PF model, following simplifying assumptions are made:

(1) The NaCl particle dissolves isotropically;
(2) The diffusion coefficients of aqueous species in solids and in solution are constants, respectively;
(3) The diffusion of all aqueous species is expressed in terms of a single ionic concentration;
(4) The solubility of NaCl in solution is independent of particle size.

3.2.5.2 Parameterization

The relationships between material properties (interface thickness l_0 and interface energy σ) and PF parameters (coefficient of PF gradient κ and double-well potential ω) are discussed in Appendix A1. The derivation of the interface mobility L, under the thin-interface thickness condition, is shown in Appendix A2. The curvature of the free energy density function A can be determined from the Gibbs free energy, i.e., ΔG (Appendix A3).

3.2.5.3 Parameter Normalization

Normalization of the model parameters is one of the important steps of data pre-processing. A series of input values are normalized to the range [0, 1] according to Appendix A4, in order to let models converge effectively.

3.2.5.4 Finite Element Implementation

Numerical implementation of the PF model is carried out by using finite element method in the framework of multiphysics object-oriented simulation (MOOSE) environment [136]. Transient solver with preconditioned Newton's method was used. In this case, the full and accurate Jacobian was calculated. The backward Euler algorithm was employed. Adaptive time stepping was used to improve computational efficiency. The time step would grow or shrink according to the number of iterations taken and needed to obtain a converged solution in the last converged step. The maximum number of nonlinear iterations per time step was also set to provide optimal solution efficiency. For 2D simulation, the triangular element type was chosen to mesh the geometry.

In addition, an adaptive mesh refinement (AMR) was used [490]. Based on the error estimated from the FEM results, the global and local mesh errors were calculated, and then the mesh size was automatically adjusted to the changing morphology of the grain boundaries at each time step. This is very effective for the numerical solution of partial differential equations in regions of arbitrary shape. In order to ensure numerical stability and simulation accuracy, at least 5 nodes on the diffusion interface were used to describe the boundary morphology, while coarser grids were used for solutions and solids that were far from the boundary (Figure 3.11). This does not only provide an accurate representation of the boundary evolution, but also improved the computational efficiency. The relative and absolute error tolerance was set to 10^{-8}.

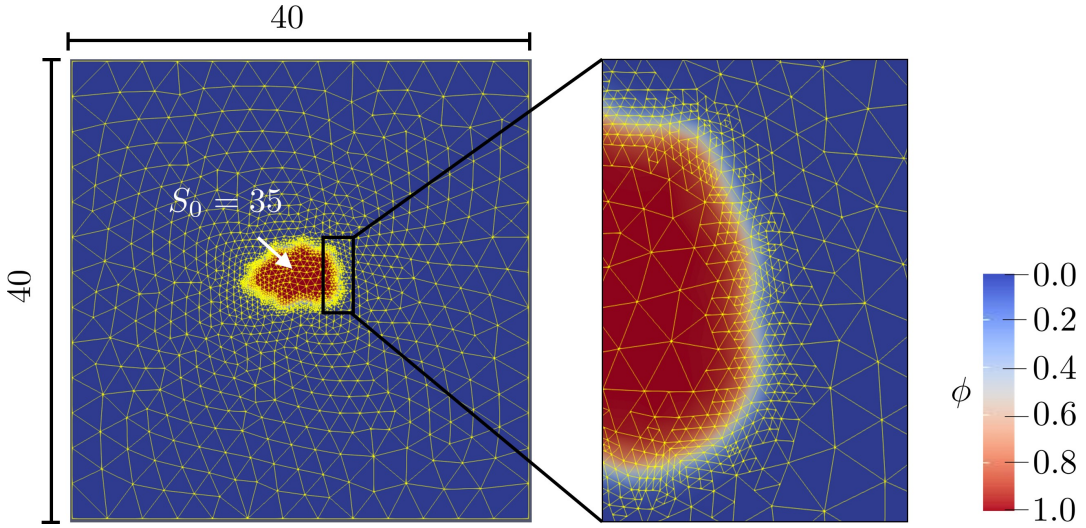

Figure 3.11. Adaptive mesh refinement in the simulation for mineral dissolution.

3.2.5.5 Central Processing Unit (CPU) Computation

The analytical experiments were performed using an Intel Core i7-6500U central processing unit (CPU) 2.5 GHz with 8 GB of RAM and MATLAB R2017a (64-bit). For the PF computation, a parallel computing was achieved by using Open Multi-Processing (OpenMP 42.0.51) on a High Performance Computer.

3.2.6 Results and Discussion

3.2.6.1 PF Validation against Analytical Solution for a Dissolution of Planar Mineral

Under diffusion-controlled dissolution conditions, if the initial thickness of the diffuse interface (l_0) is known, the interface mobility L can be determined using Equation (A10). Due to the lack of relevant experimental data upon the values of l_0, a parametric study of L was carried out. Under the assumption of a thin interface condition [1], the value of l_0 should be taken much smaller than the minimum radial dimensions of the initial solid phase; however, from a computational point of view, it is expected that the thickness of the interface has to be as large as possible in order to keep the interface from being overly densely meshed, which increases the computa-tional effort. Therefore, three cases of initial interface width, i.e., 1×10^{-8} (PFM1); 1×10^{-5} (PFM2) and 1×10^{-4} (PFM3), were tested, corresponding to 0.0003%, 0.33% and 3.33% of the initial length of the solid phase. In addition, there must be at least 5 to 10 grid points in the interface area to ensure the stability of the numerical calculation and the reliability of the results [136]. Three cases of V_0 (1×10^{-6} (PFM4); 1×10^{-8} (PFM5) and 1×10^{-10} (PFM6)) were tested.

Figure 3.12 shows a comparison between the analytical (diffusion limited) model and six cases of PF models, where the reaction rates are slower than in case of diffusion control. As l_0 decreases, L increases (as they are inversely related by Equation (A10)), causing a faster dissolution reaction, till reaching a limit defined by a diffusion control. At 8 h, PFM1 dissolves at a thickness 1.15 times greater than that of PFM3. The result of PFM2 is in good agreement with that of the analytical model. It can also be seen that the slope of the dissolution curve becomes progressively smaller

with dissolution time due to the diffusion-controlled dissolution, i.e., the overall rate of dissolution slows down as it is governed by the diffusion flux and thus dependent on the concentration gradient that reduces with saturation of the solution. However, the (slow) reaction-controlled mechanism (see curves PFM4, PFM5 and PFM6) approaches linearity as the V_0 decreases, and the lower the V_0, the slower the dissolution speed. The above results show that the PF model developed is capable of describing both the diffusion-controlled and the reaction-controlled dissolution. Under the thin interface limit condition, the agreement between the analytical (diffusion-controlled) results and the PF model for the diffusion-controlled dissolution is in satisfactory agreement with the converged solution (PFM2).

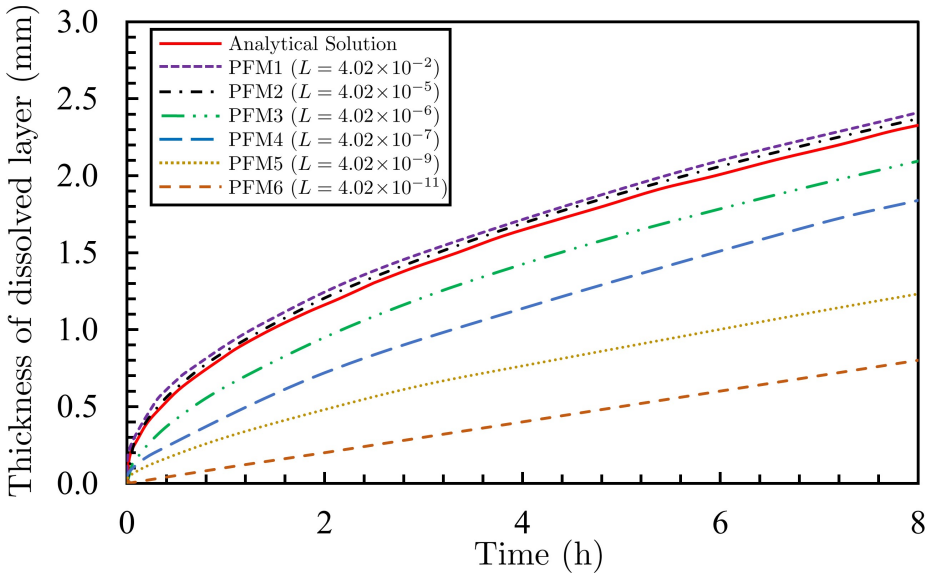

Figure 3.12. Comparison of analytical and phase-field (PF) model results of a dissolving planar mineral with variation of interface mobility L, to shift from the fastest diffusion controlled mechanism towards the slower ones limited by reaction rates.

A slight overestimation by the PFM1 model may be attributed to the used approximation (Equation (A10)) to numerically approach the diffusion-limited case. In this approximation, V_0 is approximated as D_{L}/l_0 (where D_{L} is the diffusion coefficient of the solute in the solution). The slight difference could also be the result from small incompatibility issues between the employed thermodynamic parameters, namely the used NaCl interfacial energy in PF model, and the NaCl solubility constant (p). Overall, we argue that the obtained agreement is overwhelming considering that no fitting calibration of the parameters has been performed.

Figure 3.13 shows the spatial distribution of solute normalised concentration over time. As solid dissolution starts, the concentration of solution c_{L} at the diffusive solid–liquid interface rapidly reaches saturation concentration (i.e. c_{Le} equilibrium state), while the solute normalised concentration in the solid phase keeps constant at 1 (i.e. at initial concentration). The solutes form a diffusion layer at the thin solid–liquid interface and continue to enter (diffuse) into the bulk solution. This results in a gradual decrease in the width of the solid phase. The concentration of solutes in the solution is gradually increasing, and the increase of the concentration near the solid–liquid interface is particularly significant due to diffusion limited transport through the solution. In turn the concentration of solute smoothly decreases to zero from the interface zone

to the right end of the solution. This confirms also that the dissolution is carried out in a system that is regarded as semi-infinite space, which is only controlled by a diffusion mechanism without any significant effects of the imposed boundary conditions (which deviate from the idealized semi-infinitive case).

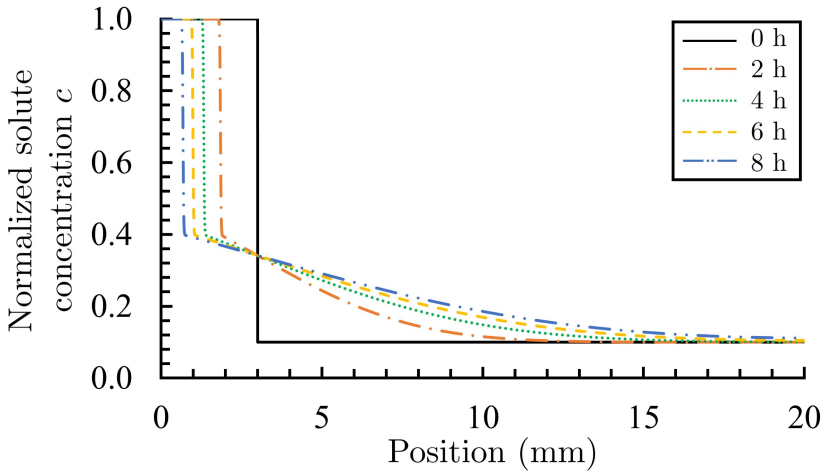

Figure 3.13. One-dimensional distribution of solute concentration by PF model ($L = 4.02 \times 10^{-1}$).

Figure 3.14 shows the movement of the interface over time. As the dissolution proceeds, the interface gradually moves toward the solid phase. It can be seen from the reduced width of the solid phase that the speed of dissolution starts faster and then slows down, again due to the limited diffusion process of the solute through the exposure solution.

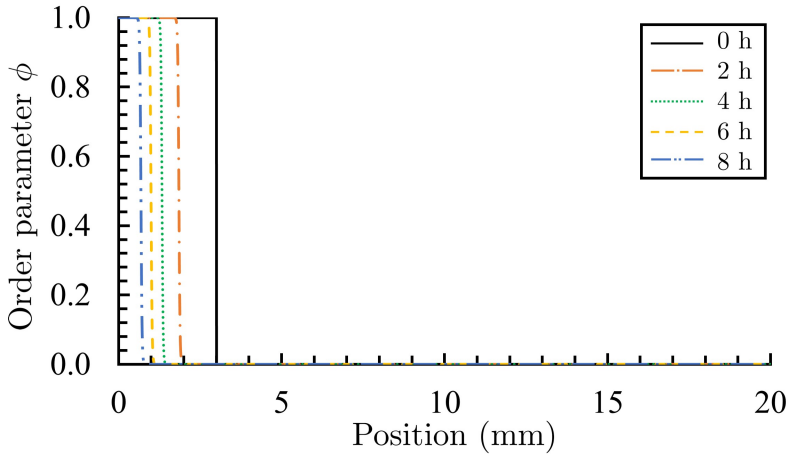

Figure 3.14. One-dimensional distribution of interface by PF model ($L = 4.02 \times 10^{-1}$).

3.2.6.2 The Effect of Mineral Shape: Dissolution Simulation by Two-Dimensional (2D) PF Model

Irregular particles can be simplified by spherical shapes provided certain conditions are met. Numerical simulations are then performed using the spherical symmetry and coordinate system, reducing the model to only one space dimension (1D model). However, some studies have shown,

both theoretically and experimentally, that the particle shape and surface roughness may affected the dissolution rates [491–495]. Therefore, before adopting the spherical simplified 1D model for NaCl crystals in this study, the effect of particle shape on the dissolution rate was analysed. In this way one can determine whether the simplification of the spherical shape for NaCl particle having some circularity factors (0.71 ± 0.06) as in used literature data [118] is reasonable.

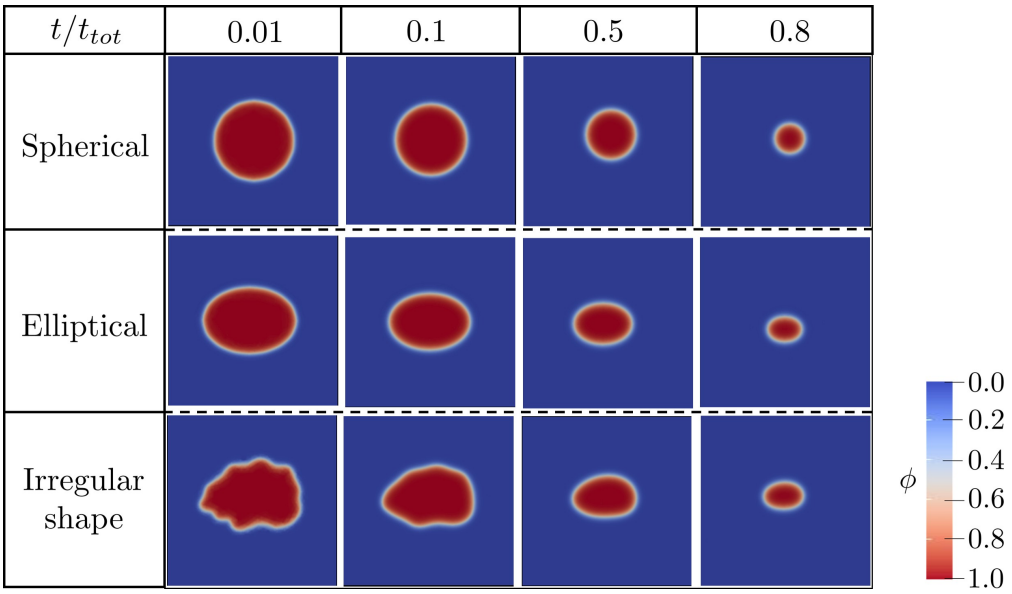

Figure 3.15. Snapshots corresponding to different time points in the dissolution profile of the NaCl crystal in 2D simulation.

Therefore, Figure 3.15 shows the 2D dissolution simulation results over time for spherical, elliptical and irregular shapes but with the same area. Qualitatively, the sharp edges of irregular shapes gradually disappear during the initial stages of dissolution, and the curvature decreases until they are completely rounded. The ratio of the major axis to the minor axis of the ellipse gradually decreases and develops towards the circular direction. The radius of the circle decreases gradually and the curvature remains constant. It can be seen that the dissolution under all shapes follows the process of spheroidization. The edges of the particle become smoother during dissolution. As the dissolution reaction proceeds, the morphological differences between the particles with different shapes become smaller.

The reason for this trend is that among closed geometries of equal area, circles have the smallest circumference. This means that the total interfacial free energy of the solid-liquid is minimal. Irregularly shaped solids have a high solid–liquid total interface free energy due to their uneven boundaries. A high interfacial energy means a high total free energy of the system. The system always tends to decrease the total free energy, this being an important factor in determining the mineral shape during dissolution. The area of the solid–liquid interface tends to decrease, which causes the flange at the solid–liquid interface to disappear and eventually to become round.

Since the solid–liquid interface is described in the PF model as a diffuse interface, with a certain width, it is difficult to describe the interface length in terms of the absolute perimeter of the solid phase. However, in order to characterize the change in the surface morphologies of crystals for different shapes with time, the contour length of ϕ=0.5 is taken to approximate the solid-phase perimeter. Figure 3.16 shows that at the initial condition, the irregular mineral grain has the

maximum interfacial length. As the dissolution reaction proceeds, the interfacial length gradually decreases and the curves of the ellipse and circle almost coincide.

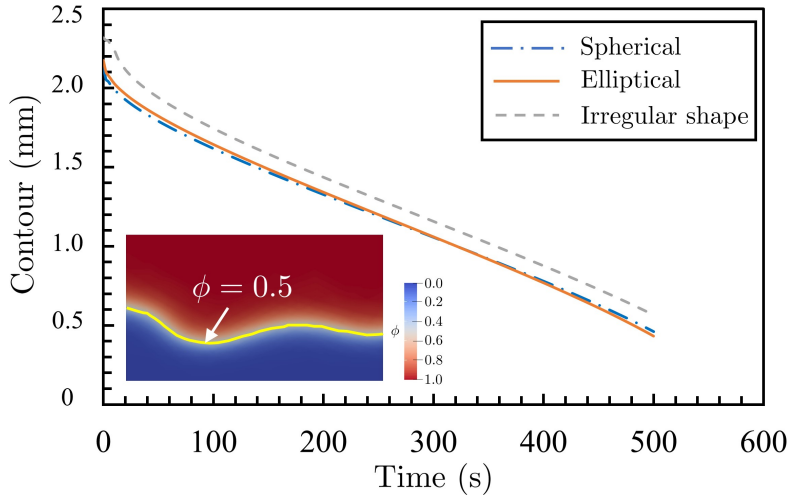

Figure 3.16. The contour change diagram of different particles for ϕ=0.5.

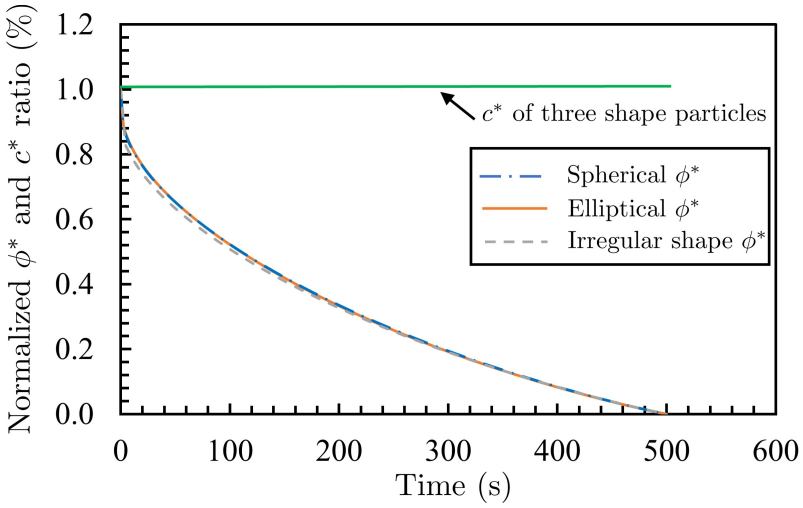

Figure 3.17. Evolution of normalized ϕ^* and c^*.

The normalized phase ratio ϕ^* is defined as $\phi^* = (\phi_t - \phi_{\text{min}})/(\phi_{\text{max}} - \phi_{\text{min}})$, being ϕ_t the integration of the phase at the time t, over the domain, while ϕ_{min} and ϕ_{max} are representing the min and max integration of the phase, respectively (for c as well). The profile of the normalized phase ratio physically represents the projected area of particles. It can be seen from Figure 3.17 that the projected area of the three shapes of particles decreases with time, while the normalized concentration ratio (c^*) keeps constant, which proves the conservation of mass for solute transport. The slope of ϕ^* becomes progressively smaller. This is because as the solid phase dissolves, the interfacial area decreases. The contact area between the solute source and the diffusion-solution zone is getting smaller. This results in a decreasing solute flux to the solid surface, which leads to a progressively slower dissolution rate. It can also be seen from this figure that the ϕ^* profile of the circles and ellipses basically overlap. The dissolution rate of irregular shapes before 200

s is slightly faster than that of circles and ellipses, while after 200 s, the three curves overlap and dissolve completely at the same time. This is because the perimeter of the irregular shape is much larger than that of the circles and ellipses, which exhibits a faster rate at the beginning of dissolution. As the dissolved shape tends to be round with the lowest interfacial energy, the circumference between the three shapes becomes similar (Figure 3.16). Therefore, in the later stages of dissolution, the dissolution curves of the three shapes are coincident.

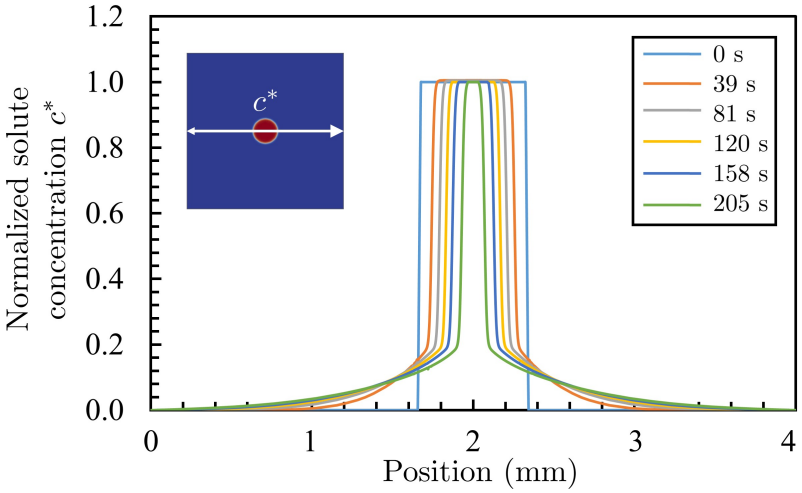

Figure 3.18. Concentration profiles of single NaCl spherical particle along radial direction with time.

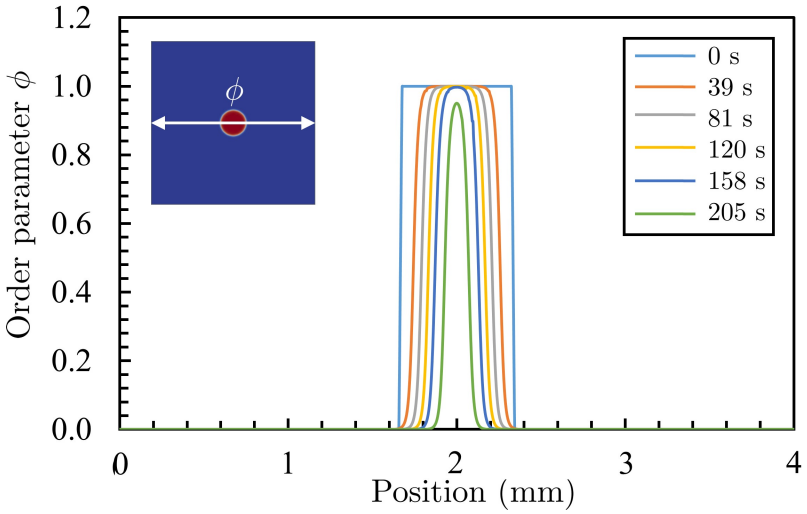

Figure 3.19. Phase profiles of single NaCl spherical particle along radial direction with time.

Figures 3.18 and 3.19 show the concentration along the radial of the circle and the spatial distribution of its phase with time, respectively. The concentration of the solute in the solid phase remains constant. The radial length of the solid phase decreases symmetrically towards the centre. After the onset of dissolution, the concentration of solutes near the solid–liquid interface saturates rapidly. The concentration of solutes in the solvent gradually increases with the diffusion mechanism.

3.2.6.3 PF Validation against Experimental Results and Analytical Solution

Figure 3.20 shows a comparison of the analytical solution, the PF model results and experimental results regarding the dissolution rate of individual NaCl crystals. The undissolved area is calculated from the residual solid phase length in the 1D simulation. The analytical solution is slightly below the lower boundary of the experimental values. In order to ensure that the dissolution reaction rate is completely controlled by the diffusion, the length (volume) of the exposure solution must be large enough so that semi-infinitive conditions are met, corresponding to the analytical solution. In that case no increase in concentration of solute should occur at the system (solution) boundary point.

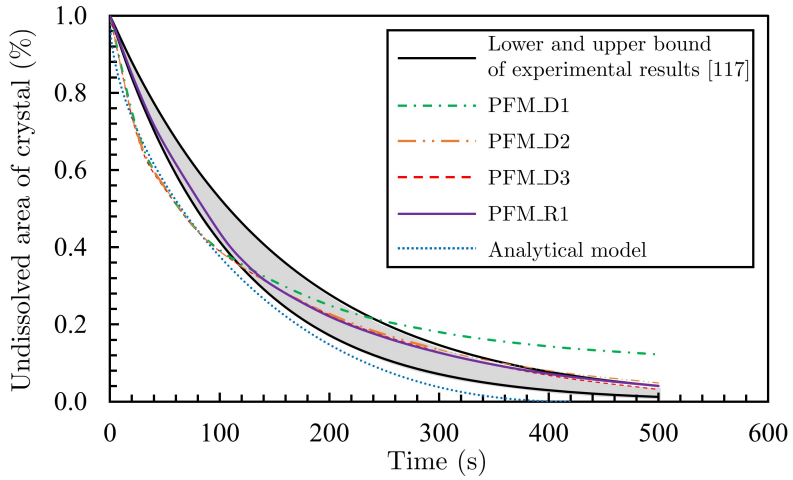

Figure 3.20. Comparison of numerical and experimental results of NaCl single particle dissolution.

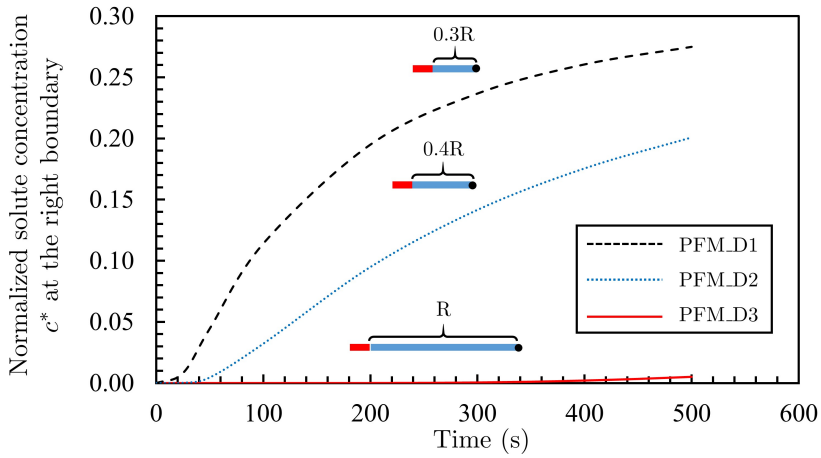

Figure 3.21. Change in solute at the solution boundary with time.

The length of solution 0.3 times (PFM_D1), 0.4 times (PFM_D2) and the original length (PFM_D3, 4.92×10^{-3} m) were tested using the PF method. From the results it can be seen that the dissolution rate slows down and the solute concentration increases significantly at the solution boundary point as the solution phase length becomes shorter (Figure 3.21). The change in solute at the boundary point, calculated using the solution lengths in the experiment (PFM_D3), is almost zero. It was

thus verified that the diffusive dissolution of individual NaCl crystals can be simulated well using our implementation of the PF method.

The experimental result in Figure 3.20 shows lower initial rates, due to the reaction controlled mechanism. Initially, the diffusion flux is very high, as the solute concentration of the initial exposure solution is zero (initial condition). Therefore the overall reaction rate is limited by the reaction rate which is lower than the initial high diffusion flux. Such reaction rates in the PF model can be considered in the interface mobility (L) that should vary with time and is fundamentally a function of the Gibbs free energy of the chemical reaction or the solute concentration. In future, it should be attempted to physically represent the interface mobility kinetics (L) as a function of the solute-under saturation, as commonly used in reaction rates expressions. Such a more fundamental approach is still missing in PF, due to the complexity in its mathematical derivation. Here, L is adjusted in a simplified way as a smaller value (4.11×10^{-6}) within 100 s and a larger value (4.11×10^{-3}) after 100 s whose result is represented by PFM_R1. As can be seen from the comparison, the dissolution rate is relatively flat at the early stage of dissolution when process controlled by the reaction. The curve of PFM_R1 is higher than that of PFM_D1, D2 and D3. However, after 100 s, PFM_R1 almost overlap with the other three due to the conversion of the dissolution rate control into the diffusion control mechanism.

3.2.7 Conclusions

Based on the results of this study, the following conclusions can be summarized:

(1) by comparing with the results of the analytical method, it is verified that the PF model can accurately handle the dynamic evolution of the general diffusion-controlled phase transformation process;

(2) using NaCl as an example, the PF model can successfully simulate the mesoscopic evolution of inorganic non-metallic materials caused by diffusion-controlled dissolution. Using the derived interfacial mobility, the PF numerical simulation results show accurate and consistent agreement with the analytical method results, as well as with the experimental ones derived with video-microscopy images analyses. It is worth mentioning that all the input parameters of the PF model have real physical meaning and are based on the experiments data;

(3) an observed discrepancy was related to the dissolution mechanism, which was found to be initially limited by the reaction rate, being slower than the diffusion flux due to the rapid change of solute concentration. This change in dissolution mechanism was successfully captured by adjusting the PF interface mobility (L).

(4) the dissolution characteristics of NaCl particles with different circularity factors were analysed by the 2D PF model. The simplification of spherical shape for NaCl particles was verified to hold.

In future studies, the reaction control and diffusion control mechanisms will be combined with the second law of thermodynamics and non-equilibrium thermodynamics with respect to L, so that L can be represented as the function of solute concentration or the Gibbs free energy of the reaction. In addition, numerical simulations need to be implemented at higher space dimensions to allow the introduction of complex microstructures in mineral particles, such as pores, grain structure and surface roughness, so that their impact on dissolution kinetics can be assessed. The above

results confirm that the dissolution kinetics of mineral particles can be successfully simulated using the employed PF model and the irregular morphological evolution can be effectively simulated in 2D. It is worth noting that the surface morphology of irregular particles has a strong influence on the dissolution kinetics. Numerical simulations need to be implemented in a higher spatial dimension to allow the introduction of complex microstructures such as pores, grain structures and surface roughness in mineral particles so that their influence on dissolution kinetics can be evaluated. The complex evolution of particle morphology in physicochemical processes can be accurately evaluated only in a full 3D system. Furthermore, a dynamic (apparent) diffusion coefficient should be explicitly taken into account, e.g. as a function of concentration, which is of critical importance in analyzing the diffusion-controlled dissolution through porous materials involving additional chemical interactions. However, highly soluble (NaCl) crystals, as investigated in this work, can be considered as non-porous which leads to assume that their diffusion coefficient can be kept constant. It is worth mentioning that the proposed PF approach can be also extended for simulating the opposite processes of those presented in this paper, namely the precipitation of NaCl. This is part of forthcoming research and will be undertaken by enriching the current free energy density function of the liquid phase through adding an extra precipitation term, i.e. $\Delta_r f$. This should be considered for further development to develop a comprehensive mineral dissolution and precipitation modelling tool.

3.3 Publication 3: A phase-field approach for portlandite carbonation and application to self-healing cementitious materials

Sha Yang[1], Yangyiwei Yang[2], Antonio Caggiano[1], Neven Ukrainczyk[1] and Eddie Koenders[1]

1 Institute of Construction and Building Materials, Technical University of Darmstadt, Franziska-Braun-Straße 3, 64287 Darmstadt, Germany

2 Mechanics of Functional Materials Division, Institute of Materials Science, Technical University of Darmstadt, 64287 Darmstadt, Germany

Journal: Mater. Struct. 2022, 55(46); https://doi.org/10.1617/s11527-022-01887-y

3.3.1 Introduction

The problem of cracks in cementitious materials is a widespread and thorough engineering problem [496]. Although small cracks do not directly cause structural failure, they can also accelerate the deterioration of a structure [497]. The presence of cracks not only affects the permeability of building structures and reduces their freeze-thaw resistance, but also many enhance the chloride attack of concrete [498–501]. Inspired by nature, a variety of self-healing mechanisms have been developed for cementitious materials [13, 49, 58, 193, 195], which has led to concrete materials becoming intelligent and capable of detecting the damage and repairing themselves. According to the report RILEM TC-221-SHC, the self-healing mechanism can be classified into "autogenic" and "autonomic" [14]. The autogenous self-healing is mainly based on the original composition of cementitious materials, which consists of three mechanisms: 1) the cement matrix on the crack surface absorbs water leading to volume expansions [14], 2) further hydration of the unhydrated cement clinker [31], and 3) carbonation of the additionally formed portlandite [30]. The autonomous self-healing is carried out with the help of healing agents. Depending on its composition, the healing agent can be divided into polymers [55], minerals [41] and bacterial spores [502].

The currently available numerical methods for self-healing can be grouped according to the nature of their self-healing mechanisms into: 1) chemical reaction-based models, for predicting carbonation [92], further hydration [31, 86, 87, 90, 91, 166, 503, 504], precipitation [89, 94] and encapsulation [97, 106, 505, 506]; and 2) transport-based models [92, 94], in which the phases affecting the healing processes are transported through the pore-structure network. A few models involve thermodynamics. Huang and Ye [32] modeled the further hydration of unhydrated cement particles based on a thermodynamic-diffusion model with coupled mass balance, charge balance and chemical equilibrium. In addition, Lattice-Boltzmann Method (LBM) as a class of Computational Fluid Dynamics (CFD) methods for fluid simulation has been used for self-healing materials in non-equilibrium thermodynamic states, such as polymer [507] and cementitious materials [508]. For the carbonation reaction, which is one of the important mechanisms of self-healing in cementitious materials, there are numerous studies that consider it as a moving boundary problem since the position of the free boundary is a function of time [509–512].

Based on the present literature review, it can be summarized that self-healing of cementitious materials is treated analytically and numerically mainly using reaction-diffusion equations. How-

ever, these models have several limitations. Firstly, the solid-liquid interface is treated as a sharp interface, which leads to the discontinuity in some of the continuously varying parameters at the interface (e.g. ionic concentration field), making it difficult to trace the evolution of certain physical processes, notably, the concentration profile across the interface. Secondly, sharp interfaces have to be explicitly tracked, especially for the evolution of high-dimensional, microstructurally complex interfaces, which can make numerical calculations extremely difficult. Thirdly, only single solid-liquid interface has been investigated in existing models. The effect of dissolution of soluble minerals on the fracture surface on the initial solid-phase boundary is not yet considered. Finally, these models are concentrated solely on the standalone self-healing process, neglecting interactions between the concentration of aqueous species in the solution, the moving front of self-healing products, and the morphology of the interface. The above limitations will be overcome by applying the Phase-Field (PF) method presented in this study.

The PF method provides an effective way to simulate migration problems of thermodynamically driven interfaces, which applies order parameters (OPs) to represent microstructures (e.g. pores, liquid and solid phases) and can include natural thermodynamic quantities such as concentration and temperature. The OPs take different constant values in different regions and have a continuous spatial variation across the interface. The microstructure and its evolution is thus reproduced by the spatial and temporal distribution of the OPs, without the need for interfacial tracking [513]. Several PF models for dissolution and/or precipitation simulations have been proposed: solutes in liquids [24, 287, 322], tri phases in porous media (two immiscible fluids and a solid phase) [323], binary or ternary alloys [273, 285, 286]. Moreover, some PF models for simulating metal corrosion are also worthy of reference [182, 298, 459].

Unlike the conventional sharp and/or single interface PF models, the contribution of presented novel PF model is based on thermodynamics to simulate the evolution of multi diffusion interfaces of self-healing process. We used the physicochemical principles of the self-healing problem to construct a free energy function that incorporates the mechanism of dissolution and precipitation interactions. By introducing an auxiliary (phase) field as a front tracking tool, the complex interface migration are implicit solved. Specifically, the solution of the model consists of determining the concentration fields of the active species and the PF.

Based on the above overview, this study will report numerical simulations of the carbonation reaction of cementitious materials using the PF method from the perspective of dissolution and precipitation. The numerical model is introduced in chapter 3.3.2, including the novelty on the construction of energy functions for multiphase dissolution and precipitation. Numerical simulation and experimental methodology is presented in chapter 3.3.4. The experimental validation and the model application are demonstrated in chapter 3.3.5, followed by a series of parametric studies. Finally, concluding remarks are provided in chapter 3.3.6.

3.3.2 Phase-field model of self-healing

3.3.2.1 Phase-field scenario

From a chemical point of view, the hydration reaction of cementitious materials is a complex dissolution-precipitation reaction in which, unlike the reaction of a single component, numerous components of cementitious materials react simultaneously with different thermodynamics and kinetics, and the various mineral components interact with each other. This poses a great challenge

for modeling. However, the carbonation reaction, which is one of the main mechanisms of self-healing in cementitious materials, could be simplified as a $Ca(OH)_2$ dissolution and $CaCO_3$ precipitation process. From the modeling point of view, a simplified approach to the analysis of the carbonation reaction (Eq. 3.43) [40, 509] can help to analyze and understand the complex self-healing mechanism based on nonequilibrium thermodynamics.

$$\begin{cases} \mathrm{CO_2(g) + H_2O} \overset{\langle 1 \rangle}{\longleftrightarrow} \mathrm{CO_2(aq) + H_2O} \overset{\langle 2 \rangle}{\longleftrightarrow} \mathrm{H_2CO_3(aq)} \overset{\langle 3 \rangle}{\longleftrightarrow} \mathrm{HCO_3^-(aq) + H^+(aq)} \\ \overset{\langle 4 \rangle}{\longleftrightarrow} \mathrm{CO_3^{2-}(aq) + 2H^+(aq)}, \ ① \\ \mathrm{Ca(OH)_2(s)} \overset{\mathrm{H_2O}}{\longleftrightarrow} \mathrm{Ca^{2+}(aq) + 2OH^-(aq)}, \ ② \\ \mathrm{Ca^{2+}(aq) + CO_3^{2-}(aq)} \longleftrightarrow \mathrm{CaCO_3(s)}, \ ③ \end{cases} \tag{3.43}$$

where, “aq”, “g” and “s” refer to species which are in an aqueous, gaseous and solid states, respectively.

Figure 3.22 shows the carbonation process and the corresponding profiles of the OPs in the PF model. Generally, the carbonation based self-healing consists of three main mechanisms: 1) CO_2 dissolves in water to form carbonate ions, 2) dissolution of Ca^{2+} ions source phase $Ca(OH)_2$, hydration product, e.g. calcium silicate hydrate (C-S-H or $3\mathrm{CaO} \cdot 2\mathrm{SiO_2} \cdot 3\mathrm{H_2O}$) and non-hydrated cement phases, e.g. tricalcium silicate ($\mathrm{C_3S}$ or $3\mathrm{CaO} \cdot \mathrm{SiO_2}$) and dicalcium silicate ($\mathrm{C_2S}$ or $2\mathrm{CaO} \cdot \mathrm{SiO_2}$) [514] in the unsaturated solution, and 3) nucleation and growth of precipitated $CaCO_3$ in the supersaturated solution [515]. The dissolution of CO_2 (g) in water proceeds through a multi-step equilibrium reactions (mechanism 1, reaction $\langle 1 \rangle$), where the reaction $\langle 2 \rangle$ is the bottleneck process, as only a very small fraction of CO_2 (aq) is transformed into H_2CO_3. In our first PF approach, a full availability of $CO_3{}^{2-}$ species is considered, thus neglecting the kinetic effects of CO_2 dissolution steps $\langle 1 \rangle - \langle 4 \rangle$. A more detailed modeling approach for the carbonation of cement pastes considering chemical thermodynamics and diffusive and convective transports can be found in recent literature, e.g. [516]. Following the PF scenario, the ion diffusion in each phase (labeled as i) is described with a conserved field variable, i.e. c_i adopting physical meaning of the concentration and track the phase evolution with a non-conserved field variable, i.e. ϕ_i adopting the physical meaning of the volumetric fraction of the phase i. Note here the c_i refers to the ratio of the actual ionic concentration C_i at a certain position and time to the initial concentration of the source phase C^0_{sou}, both in units of mol/m^3 (see Table 3.5, Sect. 3.3.4.2). The calcium ion source phase ϕ_{sou} (hereafter referred to as the source phase), the precipitation phase ϕ_{pre} and the aqueous solution phase ϕ_{aq} together form a multiphase system.

In the initial stage ($0 < t < t_p$), when the dissolution begins, i.e., only ϕ_{sou}, ϕ_{aq} and their interface $I_{\text{a-s}}$, are present in the system. Then Ca^{2+} ions diffuse from $Ca(OH)_2$, hydration products and unhydrated cement particles ($t > t_p$), and react with dissolved CO_2 in water to form suspended $CaCO_3$. As its concentration reaches a saturation c^{E}_{aq} and even an oversaturation state $c^{\text{sat}}_{\text{aq}}$, calcium carbonate pre-nucleates, nucleates, and eventually later forms crystals, precipitating on the crack surface. The interaction energy of $CaCO_3$ particles is strongly dependent on the ionic concentration in the solution [517]. This is mainly due to the fact that Ca^{2+} ions in solution produce short-range attractive and long-range repulsive interactions [518]. $CaCO_3$ particles accumulate more in ion-concentration-enriched regions. Therefore, the ion concentration can be used to express the local packing density of precipitated $CaCO_3$ particles. The corresponding interfaces of ϕ_{pre} with ϕ_{sou} and ϕ_{aq} are denoted by $I_{\text{s-p}}$ and $I_{\text{p-a}}$, respectively.

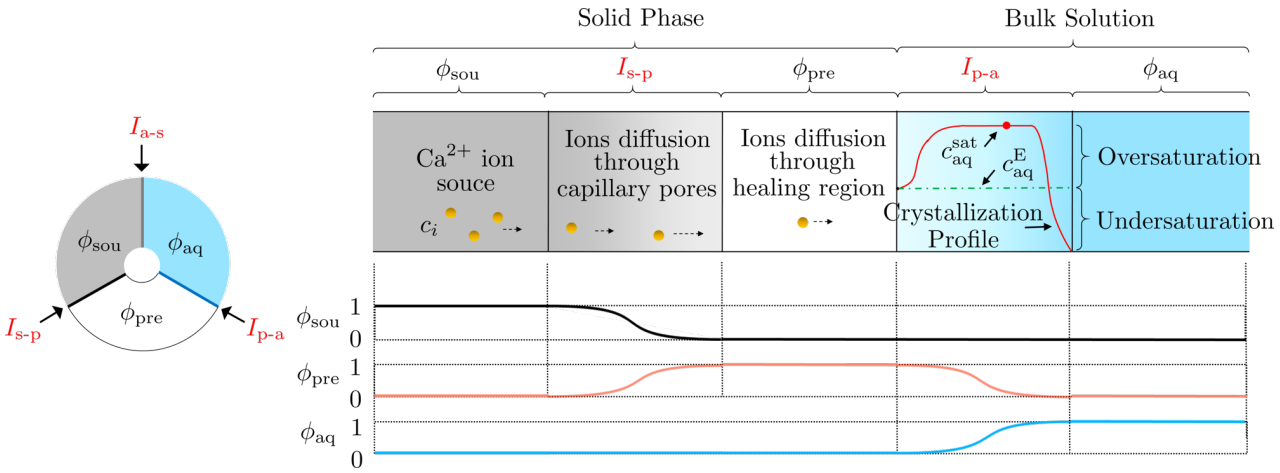

Figure 3.22. Schematic diagram of the simplified self-healing mechanism and profiles of the order parameters of the corresponding phases; t_p is the time to start precipitating.

Based on the self-healing mechanism described above, several modeling assumptions have been made:

- only the reaction of Ca^{2+} with $CO_3{}^{2-}$ ions to form $CaCO_3$ is considered. The carbonation products do not contain other intermediate substances;
- all Ca^{2+} ions localized in the crack solution may eventually be equilibrated with respect to $CaCO_3$ precipitates;
- since the number of moles of $CaCO_3$ is the same as that of Ca^{2+} ions it contains, the diffusion of all aqueous species (Ca^{2+} ions and suspended $CaCO_3$) can be expressed as a single ionic concentration c_i;
- the diffusion coefficients of aqueous substances in phase (ϕ_{pre}, ϕ_{sou} and ϕ_{aq}) and the corresponding interface ($I_{s\text{-}p}$ and $I_{p\text{-}a}$) are constant, respectively (see Figure 3.22).

3.3.3 Thermodynamic and kinetic formulations

The multi non-conserved OPs $\{\phi_i\}$ are continuous functions of time t and space x, which indicate each phase to convert between 0 and 1 within a thin diffusion translation interface. Subscription $i = \text{sou, pre and aq}$ is used further. The three phase contributions (ϕ_{sou}, ϕ_{pre} and ϕ_{aq}) are constrained following [519], i.e.,

$$\phi_{sou} + \phi_{pre} + \phi_{aq} = 1. \tag{3.44}$$

Considering this multi-phase constraint, the free energy $\mathscr{L}$, within the simulation domain Ω with the Lagrangian multiplier λ, is written as

$$\mathscr{L}\left(\{c_i\},\{\phi_i,\nabla\phi_i\}\right) = \int_\Omega \left[f_{loc}(\{c_i\},\{\phi_i\}) + f_{int}(\{\nabla\phi_i\}) + \lambda(1-\sum\phi_i)\right] \mathrm{d}\Omega, \tag{3.45}$$

where f_{loc} and f_{int} are the terms for local and interface free energy density, respectively. The local free energy f_{loc} can be formulated as an extension of the double-well function as

$$f_{loc}(\{c_i\},\{\phi_i\}) = \sum_i \left[\Phi_i(\phi_i)f_i(c_i) + \omega_i g(\phi_i)\right] \tag{3.46}$$

where $\Phi_i(\phi_i)$ are originally the tilting functions [520], which is reduced in this work in a two-phase interpolating function as: $\Phi_i(\phi_i) = (10 - 15\phi_i + 6\phi_i^2)\phi_i^3$. ω_i is the height of the imposed double-well energy barrier of each phase. $g(\phi_i) = \phi_i^2(1-\phi_i)^2$ is the double-well potential. The free energy density of each phase $f_i(c_i)$ is approximated by a parabolic function as follows

$$f_{\text{sou}}(c_{\text{sou}}) = A_{\text{sou}}(c_{\text{sou}})^2, \tag{3.47}$$

$$f_{\text{pre}}(c_{\text{pre}}) = A_{\text{pre}}(c_{\text{pre}} - c_{\text{pre}}^{\text{E}})^2 - \Delta_{\text{r}} f, \tag{3.48}$$

$$f_{\text{aq}}(c_{\text{aq}}) = A_{\text{aq}}(c_{\text{aq}} - c_{\text{aq}}^{\text{E}})^2, \tag{3.49}$$

where A_i is the potential parameter employed to construct the local free energy of distinct phases in order to approximate the actual thermodynamic system.

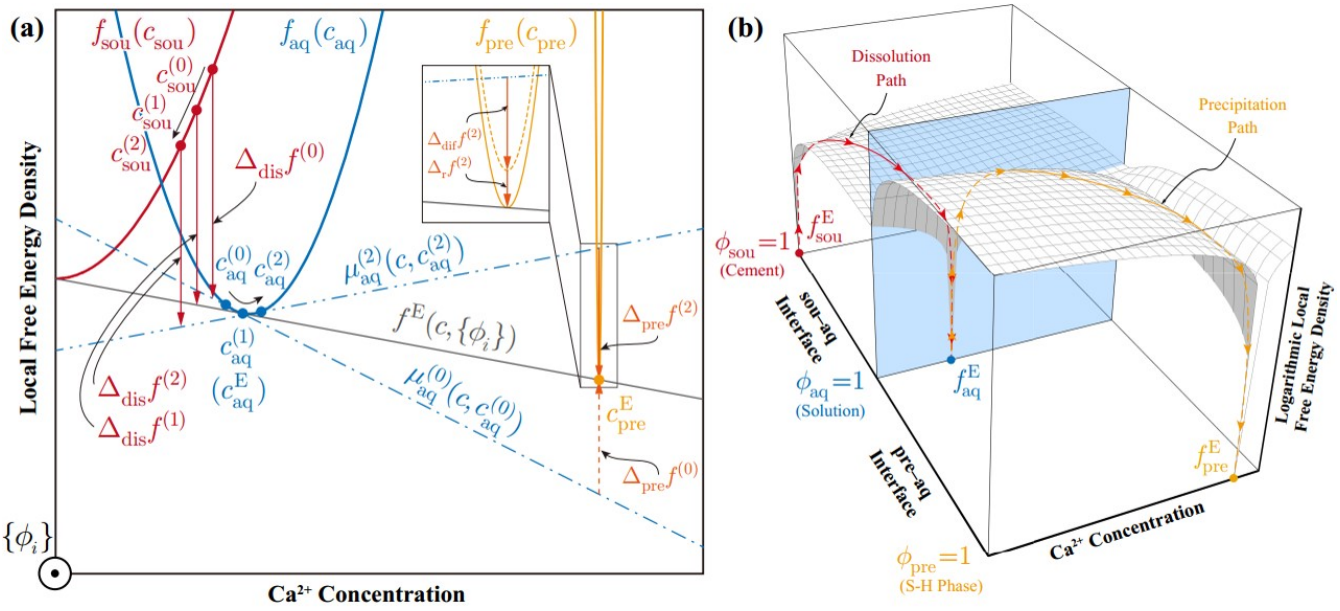

Figure 3.23. (a) Processes and driving forces for the three stages. (b) Logarithmic free energy density landscape among the source phase, the precipitation phase, and the aqueous solution as the junction phase. Energy variation paths (of dissolution and precipitation) are also illustrated.

Figure 3.23 illustrates the path of local free energy variation with the concentration $\{c_i\}$ and the order parameters $\{\phi_i\}$ for the three stages of the self-healing reaction, i.e. (0) undersaturation, (1) saturation and (2) oversaturation. In the unsaturated state, Ca^{2+} ions dissolve from the cementitious matrix and diffuse into the solution to form suspended $CaCO_3$, which is accompanied by a decrease in the solute concentration in the cementitious matrix from $c_{\text{sou}}^{(0)}$ to $c_{\text{sou}}^{(1)}$ and an increase in the solute concentration from $c_{\text{aq}}^{(0)}$ to $c_{\text{aq}}^{(1)}$ in the solution. The difference in the diffusion energy of the cementitious matrix changes from $\Delta_{\text{dis}} f^{(0)}$ to $\Delta_{\text{dis}} f^{(1)}$. The precipitation chemical driving force $\Delta_{\text{pre}} f^{(0)}$ is negative when the solution is not saturated, which corresponds to the inability to precipitate but only to dissolve. When the solution is saturated or even supersaturated ($c_{\text{sou}}^{(1)}$ to $c_{\text{sou}}^{(2)}$ and $c_{\text{aq}}^{(1)}$ to $c_{\text{aq}}^{(2)}$), i.e. the chemical driving force $\Delta_{\text{pre}} f^{(2)}$ is positive, after which the suspended

$CaCO_3$ starts to precipitate. In order to properly emulate this process, $A_{\text{sou}} < A_{\text{aq}} \ll A_{\text{pre}}$ should be numerically satisfied. Meanwhile, the thermodynamic driving force for the precipitation of $CaCO_3$ consists of the contribution of the reaction part $\Delta_{\text{r}} f^{(2)}$ and the diffusion part $\Delta_{\text{dif}} f^{(2)}$.

The precipitation follows a non-equilibrium process in which $CaCO_3$ aggregates with characteristic mean cluster size form and grow, thus filling the cracks. For $CaCO_3$ nanoparticles present in solution, their mutual clustering is strongly dependent on the ionic concentration of the solution. When the ionic concentration is small, dissolution of the reactants is promoted. An increase in the ionic concentration rapidly promotes the production of more precipitation. The precipitation reaction term $\Delta_{\text{r}} f$ should be an expression of the free energy density related to the chemical formation of $CaCO_3$ particles [451]. In this PF model, we simplify the precipitation term to a non-negative constant. With this constant we are able to define the free energy of the precipitation phase $f_{\text{pre}}(c_{\text{pre}})$ (as shown in Eq. (3.48)) in the region that allows the $CaCO_3$ precipitation, i.e. located in the oversaturation (OS) regions.

The energy contributions at the diffusive interface is formulated [1] as

$$f_{\text{int}}(\nabla\{\phi_i\}) = \sum_i \frac{\kappa_i}{2} |\nabla\phi_i|^2 \tag{3.50}$$

where κ_i is the gradient energy coefficient of each phase. Based on the formulations of [1], the interface is described as a mixture of multi-phase with different compositions, but with the same chemical potential. The local concentration c is thus defined as the weighted superposition of each phase c_i

$$c = \Phi_{\text{sou}} c_{\text{sou}} + \Phi_{\text{pre}} c_{\text{pre}} + \Phi_{\text{aq}} c_{\text{aq}}. \tag{3.51}$$

These phase concentrations are further constrained by an equal-chemical-potential condition, i.e.

$$\mu = \frac{\partial f_{\text{sou}}}{\partial c_{\text{sou}}} = \frac{\partial f_{\text{pre}}}{\partial c_{\text{pre}}} = \frac{\partial f_{\text{aq}}}{\partial c_{\text{aq}}}. \tag{3.52}$$

The temporal evolution of the non-conserved order parameters $\{\phi_i\}$ is governed by the Allen-Cahn equation [167] as

$$\frac{\partial \phi_i}{\partial t} = -L_i \frac{\delta \mathscr{L}}{\delta \phi_i} \tag{3.53}$$

with the corresponding interface mobility coefficient L_i. On the other hand, the conserved local concentration field c is governed by diffusion equation [1] as

$$\frac{\partial c}{\partial t} = \nabla \cdot \left(D \sum_i \Phi_i \nabla c_i \right), \tag{3.54}$$

which can be also regarded as the reduced version of Cahn-Hilliard equation by applying the chain rule on the chemical potential [1]. The solute diffusion coefficient can be formulated as $D = \sum_i \Phi_i D_i$ considering the effective value of each phase D_i and corresponding interpolation Φ_i.

Analyzing the equilibrium properties of the kinetic equations (3.53) and (3.54) by means of the thin interface limit analysis [1], the unknown model parameters κ_i and ω_i can be expressed

by the interfacial energy $\sigma_{i\text{-}j}$ and the interfacial width $l_{i\text{-}j}$. As the general formation, κ_i and ω_i, corresponding to the OP ϕ_i, are calculated as follows

$$\kappa_i = \frac{3}{4}\left(\sigma_{i\text{-}j} l_{i\text{-}j} + \sigma_{i\text{-}k} l_{i\text{-}k} - \sigma_{j\text{-}k} l_{j\text{-}k}\right), \tag{3.55}$$

$$\omega_i = 6\left(\frac{\sigma_{i\text{-}j}}{l_{i\text{-}j}} + \frac{\sigma_{i\text{-}k}}{l_{i\text{-}k}} - \frac{\sigma_{j\text{-}k}}{l_{j\text{-}k}}\right), \tag{3.56}$$

where $i,\ j,\ k$ are distinct phase subscriptions, i.e. sou, pre or aq.

3.3.4 Method

3.3.4.1 Simulation setup

Figure 3.24 shows a 2D schematic view of a simulation domain of size 375 µm × 750 µm for the parameter research. The initial width of the crack is set to 150 µm. In this model, the solid calcium hydroxide provides a source of calcium ions. When the crack width is much smaller than the size of the source phase and the number of cracks is sufficiently few, it can be considered as a constant supply of calcium ions in the system. However, when the cracks are densely distributed, this causes competition for the supply of Ca^{2+} ions around the cracks. Therefore, only a limited ions supply is available. This phenomenon can be simulated by two boundary conditions (BC), i.e. BC1: the boundary of the domain Γ_1 is a constant concentration ion reservoir following (Equation 3.51); BC2: there is no mass exchange between the domain and the environment along the outward unit normal of the boundary Γ_2. $\mathbf{n}$ is the normal vector. For the realistic simulation of the model, Binary Large Objects (BLObs) were converted from the experimental images derived from the stereo microscope (see Sect. 3.3.5.3), imported and processed using the MOOSE-embedded ImageFunction and associated utilities.

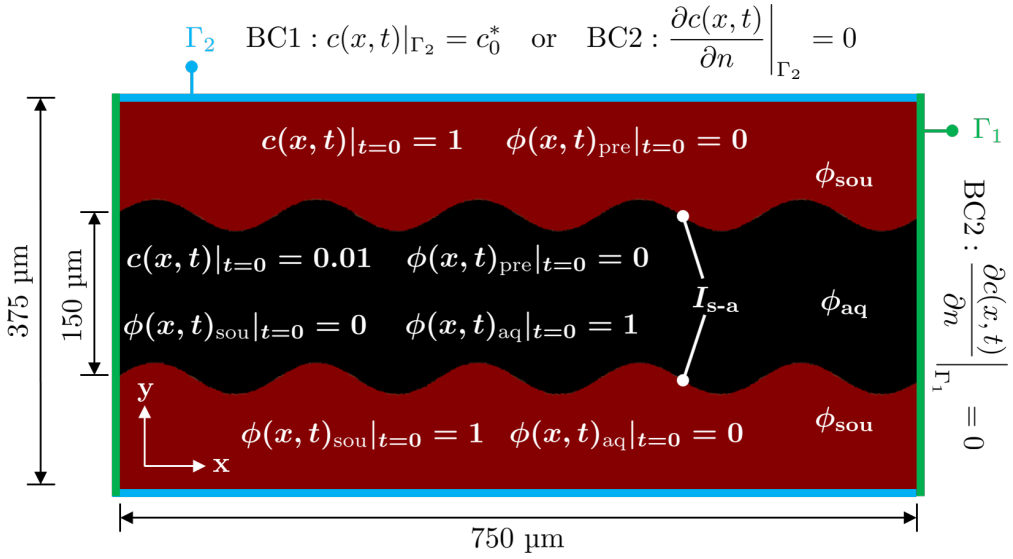

Figure 3.24. Schematic view of a typical crack and the initial and boundary conditions used in the PF model. The source phase and the aqueous solution phase are separated by the diffusion interface $I_{\text{a-s}}$.

3.3.4.2 Parameter normalization

To ensure the convergence of the model and to improve the computational efficiency of solving the non-linear governing equation sets, all variables are normalized. Spatial derivatives are normalized with respect to the reference length r, which is set to 5% of the initial crack width. Dimensionless forms of other quantities are given in Table 3.5.

Table 3.5. The dimensionless forms of the parameters.

	Symbol	Normalization		Symbol	Normalization
Physical quantity	c_i	$c_i^* = C_i/C_{\text{sou}}^0$	Model parameter	A_i	$A_i^* = A_i/\omega_{\text{pre}}$
	L_i	$L_i^* = \omega_{\text{pre}} r^2 L_i/(D_{\text{aq}})$		ω_i	$\omega_i^* = \omega_i/\omega_{\text{pre}}$
	t	$t^* = D_{\text{aq}} t/r^2$		κ_i	$\kappa_i^* = \kappa_i/(\omega_{\text{pre}} r^2)$
	D_i	$D_i^* = D_i/(D_{\text{aq}})$			
Operators	∇	$\nabla^* = r\nabla$			

In order to enable a valid comparison of the varying order parameters in the same time frame, the original data were linearly transformed by equation 3.57.

$$\phi_i^* = \frac{\phi_i^t - \phi_i^{\min}}{\phi_i^{\max} - \phi_i^{\min}} \tag{3.57}$$

where, ϕ_i^t is the integration of the corresponding phase at the time t over the 2D domain, while $\phi_i^{\min}$ and $\phi_i^{\max}$ represent the minimum and maximum integration of the corresponding phase, respectively. The residual source phase ratio, the precipitation generation ratio and the self-healing ratio can be expressed as the corresponding normalized phase ratio ϕ_{sou}^*, ϕ_{pre}^* and ϕ_{aq}^*, respectively. The physical meaning for the integration, could be related in terms of the derivative of the porosity integral on the surface.

3.3.4.3 Finite element implementation

The PF model was implemented using the Finite Element Method (FEM) in the framework of the Multiphysics Object-Oriented Environment (MOOSE) [521]. 4-node quadratic Lagrangian elements were chosen to mesh the geometry. Transient solver with preconditioned Jacobian-Free Newton–Krylov method (PJFNK) and backward Euler algorithm were employed. Adaptive mesh and time stepping schemes are used to reduce computation costs. Error indicators employed in H-adaptive meshing scheme on both $\{\phi_i\}$ and $\{c_i\}$, with the h-level as four, were specified to guarantee the precision requirement of the diffusive interface.

3.3.4.4 Experimental method

Experimental studies were conducted at the Institute of Construction and Building Materials of the TU Darmstadt. The $Ca(OH)_2$ powder (ROTH, >96%) was compressed by a hydraulic press (ENERPAC P142, USA) at 40 MPa pressure into tablet specimens having dimensions of 15 mm diameter and 10 mm height (Figure 3.25). The specimens were completely sealed using a vacuum

impregnation device (EPOFIX from Struvers, Denmark) at a pressure of 20 kPa then a fissure opening with a width of 1.0 mm was carved along its diameter. This geometry was chosen to ensure one dimensional advancement of the carbonation reaction front. Each specimen was immersed in 200 mL distilled water and transferred to a regulated environmental chamber (ICH-C 110, Memmert, Germany) and carbonized for 3, 7, 14 and 21 days at a temperature of 20°C, a relative humidity of 80% (to avoid the evaporation of water from the vessel).

Due to the low concentration of CO_2 in the atmosphere (about 0.03% by volume), the carbonation process of $Ca(OH)_2$ and cementitious materials is very slow in the natural environment. Accelerated carbonation experiments are usually performed in the laboratory to quickly assess the carbonation process. In the literature, the CO_2 concentration for accelerated carbonation varies from 3% to 100% [522, 523]. The carbonation rate increases with increasing CO_2 concentration. However, this development is not significant at CO_2 concentrations above 20%, due to the fact that at high CO_2 concentrations, in the outer layers of the concrete, dense carbonation microstructures are formed, which prevent further penetration of CO_2 [524]. In order to ensure that the accelerated carbonation produces a sustained self-healing effect, a CO_2 concentration of 5% by volume was chosen for this study. Here it is important to note that our model disregarded the CO_2 dissolution kinetics, by assuming that the CO_3^{2-} is fully available in the pore system, i.e. the dissolution kinetics is instantaneous. In future modeling works, the CO_2 dissolution kinetics should be considered as well.

At each exposure time period, the corresponding specimen was taken out of the water and dried at 40°C for 24 hours. The crack opening was then vacuum filled with a low viscosity (nominally 0.6 mPa·s) epoxy resin. After the epoxy resin hardened, the specimens were polished using a semi-automatic grinding–polishing machine (LaboSystem, Struers, Denmark), initially using a disc in hardness range HV 150 to 2000 at a rotational speed of 300 rpm, followed by a lubricated cloth and polycrystalline diamond spray of, consecutively, 9, 3, and 1 µm sizes at a rotational speed of 150 rpm. The polished cross-sections of the specimens were imaged by an environmental scanning electron microscopy using a back-scattered electron detector (SEM-BSE, Zeiss EVO LS25, Germany). The chemical analysis of the polished cross sections of the samples were conducted using the energy dispersive spectroscopy (EDS) detector.

Figure 3.25. Schematic procedure of $Ca(OH)_2$ carbonation experiments.

3.3.5 Results and discussion

3.3.5.1 Experimental validation

The purpose of the experimental observation of the carbonation reaction of a single substance, $Ca(OH)_2$, is to verify the appropriateness of the multiple interfaces settings in the PF model. Figure 3.26(a) shows the SEM images of specimens after different repair time. The dashed line indicates

the initial solid-liquid interface $I_{a\text{-}s}$. The dissolution process of calcium hydroxide occurs first on the exposure surface. As the solution penetrates the surface layer of $Ca(OH)_2$ is exfoliated. By day 7, typical dendritic calcium carbonate crystals can be clearly observed on the stripped layer. Based on this dendritic layer of $CaCO_3$ crystals, $CaCO_3$ will continue to precipitate and fill the voids, resulting in a porous layer. The pore system provides a channel for further bi-directional diffusion of CO_3^{2-} and Ca^{2+} ions. By day 14 it can be seen that the carbonate ions diffuse through the porous $CaCO_3$ layer generated at the crack surface into the $Ca(OH)_2$ matrix and undergo precipitation reactions, which allows the interface $I_{s\text{-}p}$ to continue to move deeper into the matrix. At the same time, the interface $I_{p\text{-}a}$ continued to grow toward the solution, and by day 21, the cracks had completely healed. Non-homogeneously distributed light-colored patches in the healed regions were observed in the SEM images, which was due to the studied cross-section of the precipitation region containing crystalline $CaCO_3$ [525]. We also analysed the different depths of the cracks in combination with stereo microscopy and found that in the 21-day sample, the deeper areas of the cracks were completely filled with calcium carbonate. $CaCO_3$ composition was confirmed using EDS point analysis (average composition of 40.05 wt% Ca, 15.71 wt% C, 44.24 wt% O, Figure 3.26(c)). From the experimental results in Figure 3.26(b), it can be seen that by 21 days, the total moving distance of single side of $I_{p\text{-}a}$ is 2.7 times greater than that of $I_{s\text{-}p}$.

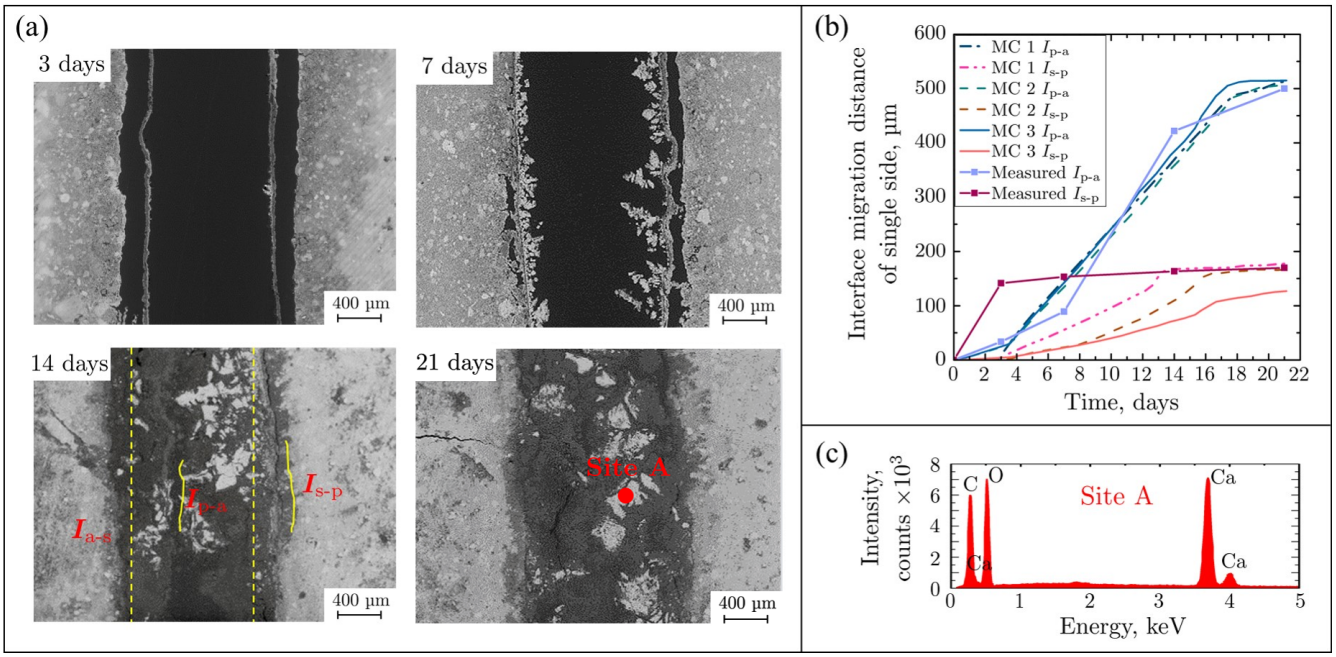

Figure 3.26. Image and data analysis of the interfacial migration of $Ca(OH)_2$ carbonation over time. (a) SEM image after different self-healing exposure times, i.e. 3, 7, 14 and 21 days; (b) comparison of numerical and experimental results of the interface migration distance, Model case is abbreviated as MC; (c) the EDS spectrum of the self-healing product.

The experiment results also showed that $I_{s\text{-}p}$ receded rapidly during the first 7 days of the experiment and moved slowly thereafter. The reason for this phenomenon is that the solute concentration of the exposed solution is zero (initial condition), i.e. the diffusion flux is initially very high. This leads to a rapid retreat of the interface due to the continuous dissolution controlled by L_{sou}. As the precipitation reaction continues on the fracture surface, a structurally dense $CaCO_3$ layer is

formed, which prevents the penetration of CO_3^{2-} ions into $Ca(OH)_2$ matrix on the one hand, and the leaching of Ca^{2+} ions into the solution on the other hand. This rate of interface migration in the PF model may be considered in the future in L_{sou}, where this mobility should vary with time and is fundamentally a function of solute concentration and porosity. However, in this study, L_{sou} is simplified to a constant. The effects of varying L_{sou} (case 1, 2, and 3) on the evolution of $I_{\text{s-p}}$ are compared with the experimental results.

The migration distances of the single side of $I_{\text{p-a}}$ and $I_{\text{s-p}}$ are calculated from the integration lengths of ϕ_{aq} and ϕ_{sou} in the 1D simulation, respectively. The model parameters for case 1 are summarized in Table 3.6.

Table 3.6. Model parameters

Symbol	Value	Unit	Symbol	Value	Unit	Ref.
A_{sou}	2.40×10^{-5}	J/m^3	κ_{pre}	7.24×10^{-9}	J/m	
A_{pre}	2.40×10^{-2}	J/m^3	κ_{aq}	1.76×10^{-9}	J/m	
A_{aq}	2.40×10^{-4}	J/m^3	$\sigma_{\text{s-p}}$	2.11×10^{-4}	J/m^2	[526]
ω_{sou}	27.48	J/m^3	$\sigma_{\text{p-a}}$	1.20×10^{-4}	J/m^2	[526]
ω_{pre}	23.16	J/m^3	$\sigma_{\text{a-s}}$	1.38×10^{-4}	J/m^2	[527]
ω_{aq}	5.64	J/m^3	D_{sou}	1.34×10^{-14}	m$^2/s$	
L_{sou}	7.00×10^{-5}	m$^2/(Js)$	D_{pre}	5.40×10^{-12}	m$^2/s$	[528]
L_{pre}	1.80×10^{-4}	m$^2/(Js)$	D_{aq}	1.34×10^{-9}	m$^2/s$	[529]
L_{aq}	1.80×10^{-4}	m$^2/(Js)$	c^E_{pre}	1.35×10^{4}	mol/m^3	
κ_{sou}	8.59×10^{-9}	J/m	c^E_{aq}	1.40×10^{-1}	mol/m^3	[530]

The parameter A_i is taken to construct the free energy of the cementitious system (Figure 3.23). The interface mobility coefficient L_i is related to the interface velocity and the driving force according to the chemical rate theory. In most of the studies, the values of interface mobility are used as empirical or hypothetical ones [459, 460]. In our study, the interface mobility was determined based on experiment results. For case 2 and case 3, L_{sou} has the value of 5×10^{-5} and 3.5×10^{-5}, respectively. Other parameters are the same as that of case 1. c^E_{aq} is derived from the solubility of $CaCO_3$ at 20°C and 1 atm. c^E_{pre} is the molar concentration of the calcium ion of $CaCO_3$ with a porosity of 47%. C^0_{sou} is calculated by dividing the density of $CaCO_3$ by its average molar mass [471]. The porosity of the diffusion coefficient of the source phase D_{sou} is obtained from the compaction density and the particle density of $Ca(OH)_2$ specimens, i.e. 30%. Based on the relationship between the diffusion coefficient, the open porosity and the pore morphology [17, 531], D_{sou} is set to be 5 orders of magnitude smaller than in its solution. As this is a crack scale model, it operates both with ion diffusivity in pore (crack) solution and effective diffusivity through porous matrix. The value of D_{pre} was determined by choosing the ion diffusion coefficient of a cementitious material with approximate porosity to the precipitated phase.

Figure 3.26(b) shows that the profiles of $I_{\text{p-a}}$ in the three cases were in good agreement with the experimental results, although the measured value on day 7 is slightly lower than that of the simulation where the measured value on day 14 is higher than the simulated values. The results

for the three models cases show a slowdown in the rate of interface migration after day 16, which is consistent with the results of the parametric analysis in Figure 3.27(a) in Sect. 3.3.5.2. For the evolution of $I_{\text{s-p}}$ it can be seen that for an increasing L_{sou}, it is possible to facilitate the $I_{\text{s-p}}$ migration in case 1 (7×10^{-5}) and case 2 (5×10^{-5}) and to make the total distance consistent with the experiments. However, the backward distance of $I_{\text{s-p}}$ grows rapidly during the first 7 days of the experiment, which is not reflected in the model results, which is due to the detachment of the surface layer after soaking of the $Ca(OH)_2$ specimens. However, it should be noted that only the continuous dissolution is considered in this model.

3.3.5.2 Parameter research

An exhaustive series of parametric studies was conducted to identify the effect of each parameter containing an actual physical significance on the model results. Firstly, the effect of the morphology of the crack on the healing effect was analyzed. The cracks are represented by two parallel sine waves. The surface roughness is constructed by adjusting the sinusoidal frequency. The amplitude of four cases is 2 and the frequencies are 1, 5, 10 and 20 respectively. As the surface roughness increases, the precipitation fills first in the areas of greater curvature. Then the interface $I_{\text{p-a}}$ gradually becomes flat. As seen in Figure 3.27(a1), case 4 is the first to be completely healed, while case 1 only reaches 0.8. From Figure 3.27(a3), it can be observed that the growth rate of self-healing ratio keeps increasing until 0.04 s, while it gradually decreases afterwards, which makes the four curves almost parallel after 0.5 s (in Figure 3.27(a2)). This is due to the curved interface which migrates spontaneously toward the center of the curvature. The larger the curvature of the interface, the smaller the radius of the curvature, the faster the interface migration, and the faster the interface will move.

The rate of the interface migration resulting from the thermodynamic driving force of precipitation and dissolution is controlled by L_i. In this model, L^*_{sou} and L^*_{pre} is referring to the normalized interface mobility coefficient of $I_{\text{s-p}}$ and $I_{\text{p-a}}$, respectively. Figure 3.27(b1) shows snapshots of crack simulations with three coefficient ratios ($L^*_{\text{pre}}/L^*_{\text{sou}}$=1, 10 and 100) at $0.3t^*$ and $0.6t^*$. It is obvious that when the coefficient ratio increases from 1 to 100, the self-healing ratio increases (Figure 3.27(b2)) while the residual source phase ratio decreases (Figure 3.27(b3)) significantly.

In order to simulate the physicochemical reactions correctly, the thickness of the interface has to be sufficiently small compared to the mesoscopic structure of the system; however, from a computational point of view, it is expected that the thickness of the interface has to be as large as possible in order to keep the interface from being overly densely meshed, which increases the computational effort. Therefore, for the simulation of crack healing with sinusoidal morphology, we quantitatively evaluated the effect of different interfacial widths (l_{i-j}=1, 2 and 4) on the model behavior. Figure 3.27(c1) shows that the operating state of sinusoidal cracks is sensitive to the interface thickness. It is evident that when the interface thickness is 1, there is a clear boundary between the two phases. And when the interfacial thickness increases to 4, the interface morphology becomes blurred. Figure 3.27(c2) shows the spatial distribution of ϕ_{pre} at $0.25t^*$ along the dashed line. As the interfacial width increases, the value of ϕ_{pre} at the crack location becomes larger, which implies that the cracks can heal faster.

So far, for all simulations the same diffusion coefficient was assumed for each phase. Therefore, the performance of the model will be tested when varying the effective diffusion coefficient of ions in the source phase D_{sou} and that in the precipitation phase D_{pre}. All of them are normalized (D^*_{sou}

$= 5 \times 10^1$, 5×10^2 and 5×10^3; $D^*_{\text{pre}} = 4 \times 10^1$, 4×10^2 and 4×10^3) with $D_{\text{aq}} = 1 \times 10^{-9}$ m^2/s (see Table 3.5, Section 3.3.4.2).

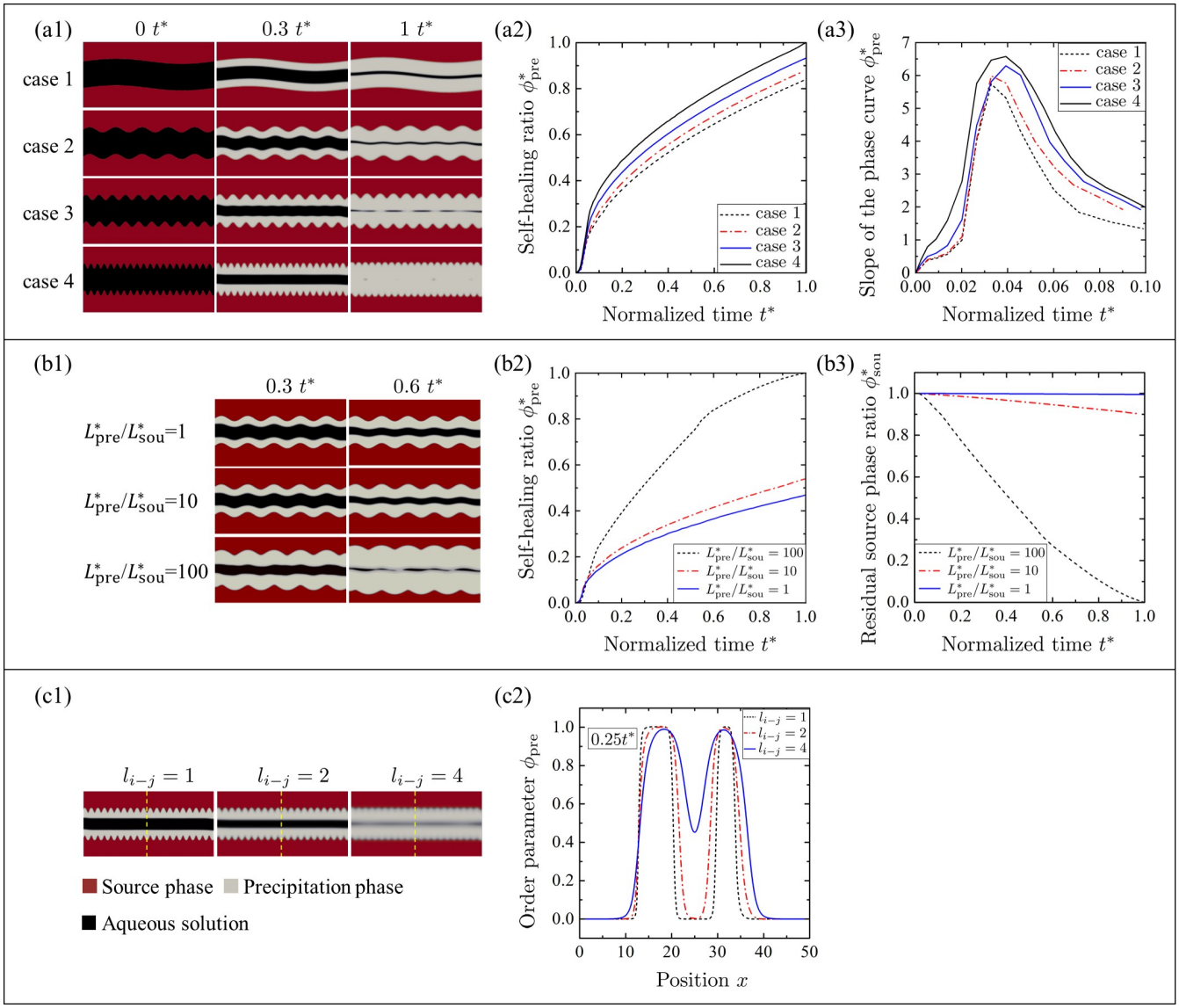

Figure 3.27. The effect PF parameter on profile of OP $\{\phi_i\}$. (a1) Simulation of self-healing with different crack morphologies, (a2) and (a3) the evolution of normalized phase ratio and its slope; (b1) Evolution of self-healing with variation of interface mobility coefficient L_i, (b2) and (b3) normalized phase ratio ϕ^*_{pre} and normalized phase ratio ϕ^*_{sou} as a function of time, respectively; Effect of interfacial width and (c2) phase ϕ_{shp} profile evolution.

Figure 3.28(a2) shows that the concentration profile of $D^*_{\text{sou}} = 5 \times 10^1$ is higher compared to that of $D^*_{\text{sou}} = 5 \times 10^2$ and $D^*_{\text{sou}} = 5 \times 10^3$ at $0.4t^*$ in the ion source phase and clearly decreases from the boundary of the ion source phase to the fracture surface, especially with a low concentration spike at $x = 34$. This is due to the large difference between D^*_{sou} and D^*_{pre}, which drives the ions appearing at the crack surface to diffuse rapidly into the precipitation region forming a concentration depletion zone at the crack surface. At $0.8t^*$ (Figure 3.28(a3)) the concentration spike rises due to more ions

being transported to the fracture surface, thus compensating for the local concentration depletion. Figure 3.28(a4) presents that the high concentration region (c^*=1) widened significantly with increasing D^*_{pre}. Higher D^*_{pre} promotes rapid ion abstraction from the source phase, which causes the concentration to decrease with increasing D^*_{pre} in the ion source phase. Figure 3.28(a5) shows the concentration profiles from $0.2t^*$ to $0.8t^*$ for $D^*_{\text{pre}} = 4 \times 10^3$. Combining Figure 3.28(a5) and (a6), it can be observed that the expansion of the high concentration region (c^*=1) slows down with time which leads to a decrease in the precipitation phase ϕ^*_{pre}. The above results indicate that an increase in the effective diffusivity of ions produces a significant increase in the precipitation width. It is worth emphasizing that in the PF method the order parameter and the concentration field are defined based on the mean field theory, which means that the fluctuated property of the concentration coefficients in the same phase are homogenized and therefore represented by a constant value. For the case where the mass transfer (incl. diffusion and fluid transfer) depending on the local pore structures, an additional conserved order parameter and corresponding fluid dynamics should be implemented [532].

The effect of two boundary conditions (BC1 and BC2) on the self-healing efficiency is discussed next. Under BC1, the effects caused by ion concentrations of 0.5 and 1.0 are compared. The position of the studied profiles is shown in Figure 3.28(a1). Figure 3.28(b) investigates the self-healing ratio ϕ^*_{pre} and normalized concentration profiles c^*_{i} with the above boundary conditions. As shown in Figure 3.28(b1), when the constant concentration c^*_{o} of the boundary (Figure 3.24) is increased from 0.5 to 1.0, the ratio of self-healing increases. As time increases from $0.2t^*$ to $0.8t^*$, there is no change in the concentration profiles in the source phase in case of boundary with a constant concentration. In contrast, the normalized ion concentration in the source phase under BC2 decreases from 0.61 to 0.39 due to further diffusion of calcium ions from the boundary to the crack surface (Figure 3.28(b2) and (b3)).

Since it is not clear whether and how the precipitation reaction term $\Delta_{\text{r}}f$ affects the concentration profiles, the effect of three cases $\Delta_{\text{r}}f$ = 5, 9 and 13 will be discussed now. The results in Figure 3.28(c1) and (c2) indicate a strong dependence of the concentration profiles on $\Delta_{\text{r}}f$. Changing $\Delta_{\text{r}}f$ from 5 to 13 produces a significant decrease of the ion concentration in the source and solution phase, which finally results in a wider precipitation region. From $0.2t^*$ to $0.7t^*$, all depressions in the middle of the curve with OS=13 are replaced by a high concentration, indicating that the crack is completely healed. The driving force contributed by $\Delta_{\text{r}}f$ drives the ions to diffuse from the source phase into the solution eventually accumulating at the crack surface. As a result, the ion concentration in the source phase and solution decreases rapidly, while the high concentration region in the phase with self-healing products increases. The above results show that the precipitation reaction progress can be effectively controlled by adjusting $\Delta_{\text{r}}f$.

3.3.5.3 Modeling Applications

The following two examples (Figure 3.29) demonstrate that the PF model can be used to quantitatively simulate the morphological migrations of self-healing cementitious materials. Example 1 is the autogenous self-healing studied by Lee and Ryou [41], while example 2 is bacteria-based self-healing studied by Erşan et al. [47]. The reasons for choosing these two examples are as follows. First of all, the primary mechanism of the autogenous self-healing is the crystallization of $CaCO_3$ [533].

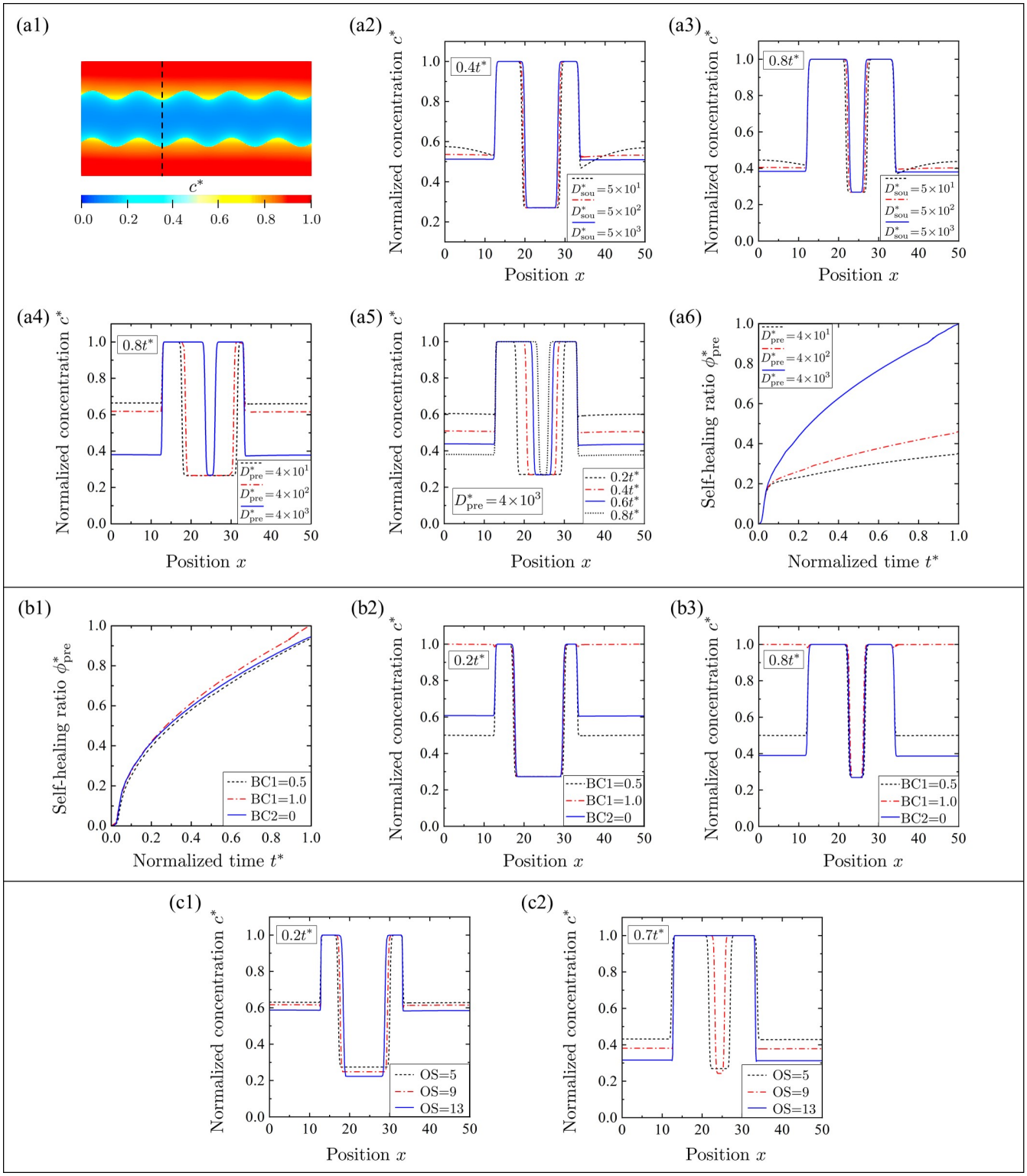

Figure 3.28. The effect PF parameter on profile of concentration c_i. (a1) the position of the studied profiles, (a2) and (a3) the distribution profiles of c^* at $0.4t^*$ and $0.8t^*$ with the variation of D^*_{sou}, respectively, (a4) the distribution profiles of c^* at $0.8t^*$ with the variation of D^*_{pre}, (a5) the distribution profiles of c^* of the case $D^*_{\text{pre}} = 4 \times 10^3$ at four time points, (a6) the evolution of the normalized phase ratio ϕ^*_{pre} with the variation of D^*_{pre}; (b1) Evolution of self-healing ratio ϕ^*_{shp} with different boundary conditions, normalized concentration profile evolution (b2) at $0.2t^*$ and (b3) at $0.8t^*$; Evolution of normalized concentration profile with the different oversaturation terms $\Delta_r f$ at (c1) $0.2t^*$ and (c2) $0.7t^*$.

Secondly, the principle mechanism of bacterial self-healing is that the bacteria act primarily as catalysts, and convert the organic biomineral precursor compound into insoluble inorganic $CaCO_3$ based minerals [72, 74, 237, 238]. When bacteria control the catalytic reaction much faster than diffusion, the self-healing process is mainly controlled by diffusion. In conclusion, these two examples can be numerically treated as a dissolution and precipitation process of solutes, which is time-dependent and controlled by diffusion. Therefore, both can be simulated using the PF model proposed in this study.

The initial widths of examples 1 and 2 are taken from the experimental data, i.e., 174 µm and 318 µm, respectively. The model parameters are the same as that in Table 3.6 except $L_{\text{aq}} = 1 \times 10^{-7}$ $\text{m}^3/(\text{Js})$, $L_{\text{pre}} = 1 \times 10^{-4}$ $\text{m}^3/(\text{Js})$ and $L_{\text{sou}} = 1 \times 10^{-10}$ $\text{m}^3/(\text{Js})$ used for example 1 and $L_{\text{aq}} = 1 \times 10^{-5}$ $\text{m}^3/(\text{Js})$, $L_{\text{pre}} = 1 \times 10^{-4}$ $\text{m}^3/(\text{Js})$ and $L_{\text{sou}} = 1 \times 10^{-10}$ $\text{m}^3/(\text{Js})$ used for example 2, respectively. The precipitation reaction term $\Delta_{\text{r}} f$ is an expression of the free energy density related to the chemical formation of $CaCO_3$ particles (equation 3.48). In this PF model, we simplify the precipitation term to a non-negative constant. Based on the authors' research experience, a reasonable range of values for $\Delta_{\text{r}} f$ is from 1 to 20. In order to focus on the effect of other parameters on the self-healing effect and to avoid the model being subjected to a large $\Delta_{\text{r}} f$ that would lead to too rapid healing, $\Delta_{\text{r}} f$ was taken as 5 in both examples.

Figure 3.29 shows schematically the concentration field c, the phase field ϕ_i and the experimental results for the 2 examples at different times, respectively. At the beginning of cracking, the reactant ion concentration c is highest in the cementitious matrix and nearly 0 in the solution. At 14 days, c at the crack surface reaches 1, while a layer of self-healing products. This indicates that the Ca^{2+} ions in the solution are carbonated and the concentration of $CaCO_3$ reaches the saturation state forming a layer of self-healing products. The concentration in the cementitious matrix is low compared to that on the crack surface. Such a difference is set to numerically reflect a physical meaning, i.e., $CaCO_3$ precipitation is difficult to form in the deep cementitious matrix due to the lack of CO_2. It can be carbonated only when Ca^{2+} ions diffuse to the crack surface. It is one of the innovations of our model that c can reach 1 only near the crack surface, thus allowing the formation of the self-healing products locally. With this strategy, the different phases can be effectively distinguished by their concentrations and tracked by the corresponding order parameters.

It is clear from the experimental results that the morphology of the cracks largely influences their local healing effect. At the same time the morphology of the crack is constantly changing with the healing process. In the depression out of the crack surface, the healing products precipitate faster and more frequently due to the higher concentration of solutes. Therefore, its local boundary moves faster than that of other locations.

The effect of crack width on the self-healing efficiency can also be seen in the simulation results of examples 1 and 2. This effect has also been mentioned in the literature [223, 534]. From the simulation results of example 1, it can be seen that the crack healing rate from 0-15 days is slower than that from 15-23 days. This is due to the slow diffusion process of Ca^{2+} ions from the cement matrix to the crack surface and their gradual accumulation in the early stage of crack appearance. Precipitation occurs only when ions concentration reaches the saturation state. The results from days 0 to 15 reflect the gradual accumulation of reactant concentrations. after 15 days, the crack healing rate is accelerated. This is due to the synergistic effect of Ca^{2+} ions diffusing from both crack sides. However, the width of example 2 is 1.8 times wider than that of example 1, which leads to the fact that the processes of diffusion of Ca^{2+} ions and occurrence of precipitation reactions on

both sides of the crack are independent of each other and have no synergistic effect. Therefore the self-healing rate of example 2 was almost constant until 20 days. The self-healing rates of the two examples slowed down after 23 and 20 days, respectively. This is due to the formation of a $CaCO_3$ layer on the crack surface thereby preventing further diffusion of Ca^{2+} ions outward.

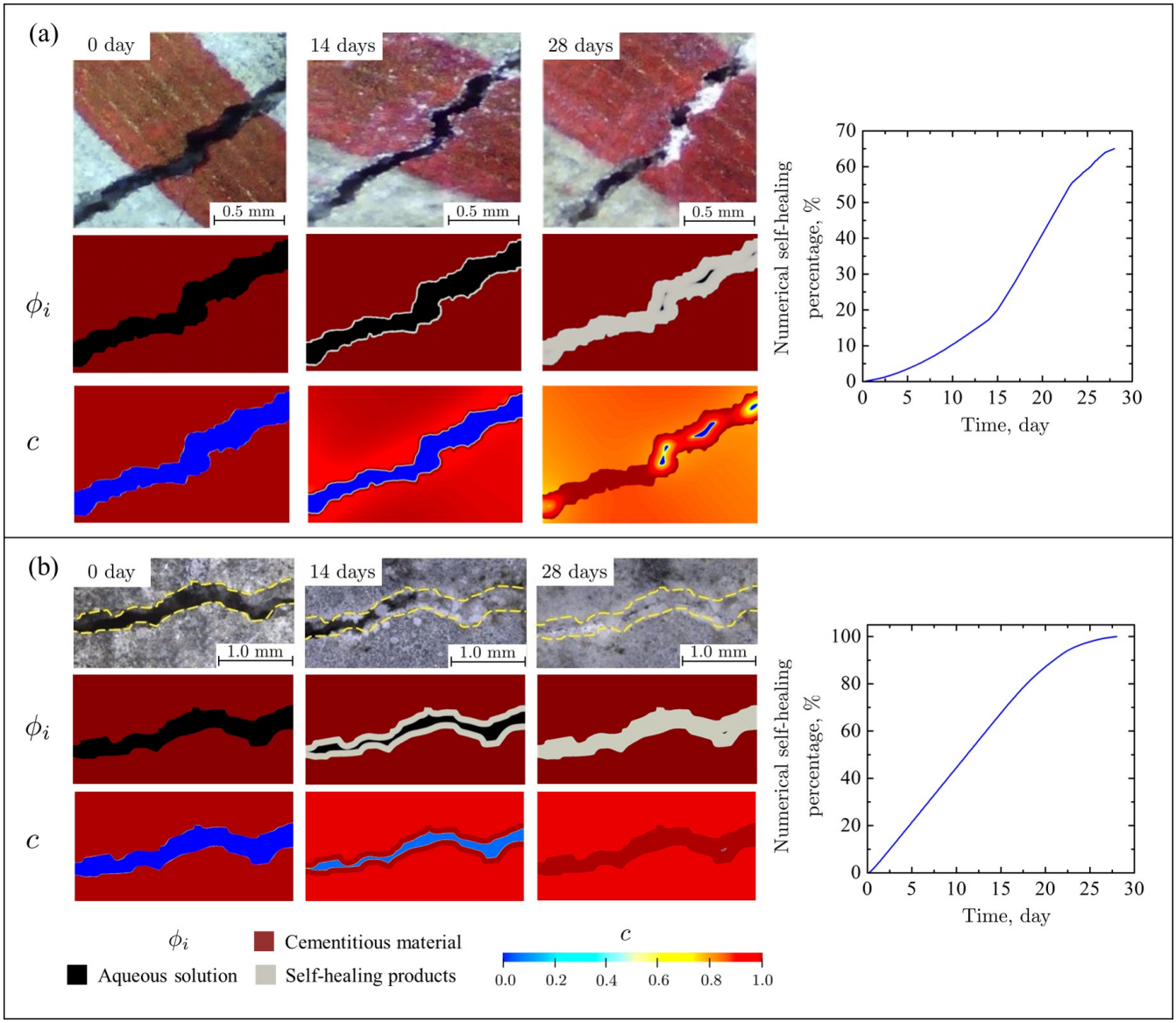

Figure 3.29. Two examples demonstrating the practical application of the PF model. (a) example 1: the autogenous self-healing, reproduced with permission from the authors of [41], copyright 2014, Constr Build Mater, Elsevier; (b) example 2: the bacteria-based self-healing, reproduced with permission from the authors of [47], copyright 2016, Cem Concr Compos, Elsevier.

The above two numerical simulations provides consistent results with experiments, which is encouraging as for the capacity of the present model to predict the morphology and the geometrical details of the interface migration of self-healing processes in cementitious materials. However, we should keep in mind that the comparison between numerical and experimental results is mainly qualitative, since we have focused only on the dissolution-precipitation mechanism, whereas for

cementitious materials containing mineral additives, the corresponding self-healing processes have to be extended to consider more types of reactions (e.g. hydration) and additional physicochemical effects (e.g. swelling and dissolution). In addition, although the empirical relationship between effective diffusivity and porosity (single value) takes into account the effect of w/c ratio, the variation of porosity is not studied in this study. The porosity should be related to the local concentration of ions and the phase in which they are located. The diffusion coefficient could be expressed as an equation related to the porosity and pore structure [531]. This model can be flexibly extend to a multiphase multicomponent form to analyze the effect of real cementitious materials on self-healing, e.g., by adding a order parameter ϕ_{sou_csh} for C-S-H in the phase of ϕ_{sou}. For this, a thermodynamic dissolution-precipitation description should be implemented as well as a change of the homogenized properties. The fluctuated properties should be homogenized and generally represented by a non-constant value, where e.g. the effective diffusion coefficient depends on the pore structure (e.g. using empirical relations [516, 531]).

3.3.6 Conclusion

In this study, a novel PF model for self-healing of cementitious materials is presented. The model can effectively capture the evolution of dissolution and precipitation interfaces controlled by diffusion and the behavior of solute concentration profiles. From the results of this study following conclusion can be drawn:

(1) the free energy of the system, approximated by a set of parabolic functions, varies with solute concentrations and order parameters, which is able to describe the self-healing processing by analyzing the thermodynamic driving force of the solute diffusion and precipitation in a thermodynamic-consistent way and thereby capable in recapitulating the process under various solute conditions, i.e. undersaturation, saturation and oversaturation;

(2) calcium hydroxide-based carbonation measurements confirm that multiple interface evolution occurs during the self-healing process. Using the derived interfacial mobility, the PF numerical simulations show a consistent agreement with the experimental results;

(3) by conducting a series of parametric studies, it was confirmed that model parameters with clear physical meanings can reflect the evolution of multiple interfaces under different conditions;

(4) 2D simulations of the interfacial growth kinetics during the self-healing of cementitious materials were carried out. Comparison with experimental results shows that the PF model is able to provide good qualitative predictions of the morphological and geometric details of interfacial migration during self-healing of cementitious materials in terms of minerals dissolution and precipitation (Figure 3.29). For a further quantitative analysis, additional types of chemical reactions and additional physical factors need to be considered.

In future studies, the free energies and the corresponding thermodynamic parameters of the involved phases will be examined to quantify mechanisms for the formation of the self-healing products, e.g. hydration kinetics, crystallization kinetics and swelling. Due to the dependence on the ion type, ion concentration, capillary pore structure, degree of chemical reaction, etc. an explicit formulation of the diffusion coefficient on relevant factors shall be derived and validated with experiments [535]. The chemistry modeling should be extended with the Ca^{2+} ion diffusion coefficient to be subject to the interaction of porosity and chemical reaction rate. Ion transport and local chemical reactions can be calculated using PHREEQC (a computer program for speciation,

reaction-path, advective transport, and inverse geochemical calculations). The yielded results are then transferred to the PF model for the further phase transformation analysis. The complex evolution of crack healing morphology in physicochemical processes can be accurately evaluated only in a full 3D system. All the above should be considered for further development of a comprehensive self-healing modeling tool for cementitious materials.

4 Conclusion and outlook

4.1 Conclusion

In this thesis, the dissolution of a single mineral particle is analysed from a phase transformation perspective using the PF method. On this basis, a conceptual multiphase-PF model is proposed to simulate the complex microstructural evolution during the self-healing of cementitious materials. The model focuses on the carbonation-based healing mechanism, which is activated by dissolving soluble calcium-containing minerals and precipitating $CaCO_3$. Based on the research presented and the results, the following general conclusions can be drawn:

(1) comparing with analytical methods, it was observed that the dynamic evolution of the solid-liquid boundary induced by diffusion-controlled dissolution, could be accurately reproduced by using the PF method. Taking the NaCl particle as an example, the PF model showned to be successful in modelling the mesoscopic evolution of inorganic non-metallic materials caused by diffusion-controlled dissolution. By adjusting the PF interfacial mobility parameter, the dissolution of the NaCl particle was effectively captured at different stages of the transition from reaction-controlled to diffusion-controlled mechanism;

(2) a novel PF model for self-healing in cementitious materials was applied to simulate the $Ca(OH)_2$ carbonation. The results showed that the PF model based on a thermodynamic basis and proposed energy equations was effective in capturing the evolution of the diffusion-controlled dissolution and precipitation interfaces as well as the behaviour of the solute concentration profiles;

(3) a comparison with experimental results of self-healing of cementitious materials revealed that the PF model was able to provide good qualitative predictions of the morphological and geometric details of interfacial migration during self-healing of cementitious materials in terms of mineral dissolution and precipitation;

(4) by conducting a series of parametric studies, it was confirmed that PF model parameters with a clear physical meaning can reflect the evolution of complex morphology and physical masses under different conditions.

4.2 Outlook

The development and successful application of the PF model has contributed to a deeper understanding of the complex boundary evolution of the self-healing process of cementitious materials

from a thermodynamic and kinetic perspective. However, there are still a large number of unresolved challenges that deserve a more in-depth study. The following potential future steps are identified:

(1) Combining the reaction kinetics of multiple substances

There are many factors that are affecting the chemical kinetics of self-healing, i.e. different ratio of adhesive agents, mineral admixtures and bacteria; fluctuations of carbon dioxide, humidity and temperature in the environment, which are affecting the overall crack healing rate. Therefore, the free energies and corresponding thermodynamic parameters of different substances need to be distinguished and their mechanisms for the formation of self-healing products, i.e. hydration kinetics, crystallization kinetics, polymerization reaction kinetics and swelling kinetics, should be reflected in specific simulations.

(2) Introduction of a dynamic diffusion coefficient

The diffusion coefficient of aqueous species is related to the type, local concentration, capillary pore structure, degree of reaction, etc. An expression for a dynamic diffusion coefficient need to be derived by combining relevant factors and should be validated with experimental data.

(3) Evolution of capillary pore structures

The microscopic structure of capillary pores of the solid phases is in dynamic exchange with the chemical reaction. The precipitation generated in the capillary pores hinders local ion transport while contributing to an altered pore structure, which further affects the diffusion potantial. Therefore, the interplay between the capillary pore structure, thermodynamics, reactant concentration and mass transport should be investigated in more detail.

(4) Development of a three-dimensional model

Although the present study has confirmed that the proposed PF model can effectively simulate the evolution of different fracture morphologies in two dimensions. However, it is worth noting that the interfacial morphology has a strong influence on the kinetics of dissolution and precipitation. In addition, inhomogeneous spatial distribution of aggregates, and the direction of moisture penetration may all affect the evolution of the interface morphology of cementitious materials. Therefore, to significantly enhance the accuracy and predictability of a crack healing process, only a full 3D system with realistic boundary conditions would apply.

Appendix

A1 The Height of the Double Well Potential ω and Gradient Energy Coefficient κ

Using the composition and PF profile at equilibrium, the interface energy σ, and the interface thickness l_0 can be evaluated as:

$$\sigma = \frac{\sqrt{\kappa\omega}}{3\sqrt{2}}, \tag{a1}$$

$$l_0 = 2.94\sqrt{2}\sqrt{\frac{\kappa}{\omega}}. \tag{a2}$$

In general, σ and l_0 can be estimated from the experiment, then the height of the double well potential ω and gradient energy coefficient κ can be easily obtained by the Equations (a1) and (a2):

$$\omega = \frac{6 \times 2.94\sigma}{l_0}, \tag{a3}$$

$$\kappa = \frac{3l_0\sigma}{2.94}. \tag{a4}$$

A2 The Interface Mobility L

The interface velocity V is typically expressed as product of a factor involving the thermodynamic driving force for dissolution and a kinetic factor involving the interface mobility [536], i.e.

$$V = V_0 \left[1 - \exp\left(\frac{\Delta G}{RT}\right)\right], \tag{a5}$$

where the kinetic factor V_0 corresponds to the limiting velocity under infinite driving force (forward reaction rate), ΔG is the Gibbs free energy difference, between the free energy of solid and liquid which is responsible for the interface displacement. The driving force of dissolution ΔF is given by $\Delta F = f^{\mathrm{L}}(c_{\mathrm{L}}^{\mathrm{e}}) - f^{\mathrm{S}}(c_{\mathrm{S}}^{\mathrm{e}}) - (c_{\mathrm{L}}^{\mathrm{e}} - c_{\mathrm{S}}^{\mathrm{e}}) f_{C_{\mathrm{S}}}^{\mathrm{S}}(c_{\mathrm{S}})$, (-$\Delta G$=$\Delta F$). Thus, Equation (a5) is obtained by Taylor series expansion and approximated as:

$$V \cong -V_0 \frac{\Delta G}{RT} = V_0 \frac{\Delta F}{RT}. \tag{a6}$$

Using the derivation in the KKS model, Equation (23) can be expressed in terms of ΔF as follows:

$$\frac{\partial \phi}{\partial t} = -L\left[\nabla\kappa\nabla\phi + h'(\phi)\Delta F\right] - \omega g'(\phi). \tag{a7}$$

Under 1D instantaneous steady state, ϕ is derived for the position as follows:

$$\frac{d\phi}{dt} = -\frac{L}{V}\left[\kappa\frac{d^2\phi}{dx^2} + h'(\phi)\Delta F - \omega g'(\phi)\right]. \tag{a8}$$

Under the thin interface limit condition, Equation (a8) combined with the equilibrium phase expression $dx/d\phi_0 = -\sqrt{\kappa}/\sqrt{2\omega}\,[1/\phi_0(1-\phi_0)]$ and Equation (a1) modifies into:

$$\frac{RT}{V_0} = \frac{\sigma}{L\kappa}. \tag{a9}$$

It should be noted that this equation only holds if the diffusion potential of solute in the interface region is constant. In addition, if the dissolution process is controlled by diffusion, V_0 is usually approximated as D_L/l_0; where D_L is the diffusion coefficient of the solute in solution [448]. In general, the determination of V_0 is very difficult [537]. In summary, L can be derived from Equation (a9):

$$L = \frac{D_\mathrm{L}\sigma}{l_0 RT\kappa}. \tag{a10}$$

A3 The Curvature of the Free Energy Density Function A

The Gibbs free energy ΔG can be obtained through equilibrium constant K:

$$\Delta G = -RT\ln K, \tag{a11}$$

$$\Delta G = -8.314 \times 293.15 \times \ln\left(\frac{0.4}{1.0}\right) = 2233.23\,(J/m^3). \tag{a12}$$

The value of A can be derived from ΔG. Following [459], A makes the free energy of the solid phase is equal to ΔG when c is 0.4 (see Figure a1).

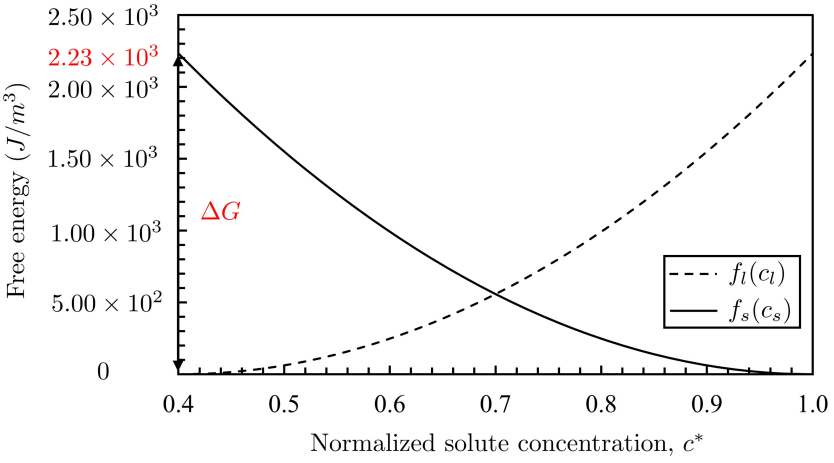

Figure 4.1. Variation of concentration with chemical driving force.

A4 PF Parameters Normalization

In order to ensure the convergence of the model on the mesoscale and improve the calculation efficiency, all variables are normalized. All molar concentrations are normalized by the solid molar concentration c_{S}, and all length scales are normalized by the length of the domain (l). According to the total energy function in Equation 3.24, three equations are proposed as follows:

$$\nabla^* = l_0 \cdot \nabla, \tag{a13}$$

$$F^* = \frac{F}{A}, \tag{a14}$$

$$D_{\mathrm{S}}^* = \frac{D_{\mathrm{S}}}{D_{\mathrm{L}}}. \tag{a15}$$

The normalized variables are presented as follows:

$$A^* = 1, \tag{a16}$$

$$\kappa^* = \frac{\kappa}{A \cdot l_0^2}, \tag{a17}$$

$$\omega^* = \frac{\omega}{A}, \tag{a18}$$

$$L^* = \frac{A \cdot l_0^2 \cdot L}{D_{\mathrm{L}}}, \tag{a19}$$

$$t^* = \frac{D_{\mathrm{L}} \cdot t}{l_0^2}, \tag{a20}$$

$$D_{\mathrm{L}}^* = 1, \tag{a21}$$

$$c_{\mathrm{Se}} = \frac{c_{\mathrm{solid}}}{c_{\mathrm{solid}}} = 1, \tag{a22}$$

$$c_{\mathrm{Le}} = \frac{p}{c_{\mathrm{solid}}}, \tag{a23}$$

where, p is the solubility of sodium chloride at 20 °C and 1 atm, which needs to be converted to units of mol/m^3 in the calculation.

Bibliography

[1] Seong Gyoon Kim, Won Tae Kim, and Toshio Suzuki. Phase-field model for binary alloys. *Physical review e*, 60(6):7186, 1999.

[2] Senot Sangadji. Porous network concrete: A bio-inspired building component to make concrete structures self-healing. 2015.

[3] TC Powers. Freezing effects in concrete. *Special Publication*, 47:1–12, 1975.

[4] Zdenek P Bazant and Folker H Wittmann. Creep and shrinkage in concrete structures. 1982.

[5] Maintenance of supersaturation ii: indomethacin crystal growth kinetics versus degree of supersaturation. *The Strategic Development Council (SDC), Vision 2020. A vision for the concrete repair, protection and strengthening industry*, 2004.

[6] K Van Breugel. Is there a market for self-healing cement-based materials. In *Proceedings of the first international conference on self-healing materials*, pages 1–9, 2007.

[7] E Cailleux and V Pollet. Investigations on the development of self-healing properties in protective coatings for concrete and repair mortars. In *Proceedings of the 2nd international conference on self-healing materials, Chicago, IL, USA*, volume 28, 2009.

[8] Baorong Hou, Xiaogang Li, Xiumin Ma, Cuiwei Du, Dawei Zhang, Meng Zheng, Weichen Xu, Dongzhu Lu, and Fubin Ma. The cost of corrosion in china. *npj Materials Degradation*, 1(1):1–10, 2017.

[9] Hendrik G Van Oss and Amy C Padovani. Cement manufacture and the environment part ii: environmental challenges and opportunities. *Journal of Industrial ecology*, 7(1):93–126, 2003.

[10] Emad Benhelal, Gholamreza Zahedi, Ezzatollah Shamsaei, and Alireza Bahadori. Global strategies and potentials to curb co2 emissions in cement industry. *Journal of cleaner production*, 51:142–161, 2013.

[11] Mineral Commodity Summaries. Mineral commodity summaries 2021: U.s. geological survey. *US Geological Survey: Reston, VA*, page 200, 2021.

[12] Yingzi Yang, Michael D Lepech, En-Hua Yang, and Victor C Li. Autogenous healing of engineered cementitious composites under wet–dry cycles. *Cement and Concrete Research*, 39(5):382–390, 2009.

[13] Nele De Belie, Elke Gruyaert, Abir Al-Tabbaa, Paola Antonaci, Cornelia Baera, Diana Bajare, Aveline Darquennes, Robert Davies, Liberato Ferrara, Tony Jefferson, et al. A review of self-healing concrete for damage management of structures. *Advanced Materials Interfaces*, 5(17):1800074, 2018.

[14] Mario De Rooij, Kim Van Tittelboom, Nele De Belie, and Erik Schlangen. *Self-healing phenomena in cement-Based materials: state-of-the-art report of RILEM technical committee 221-SHC: self-Healing phenomena in cement-Based materials*, volume 11. Springer, 2013.

[15] William J Boettinger, James A Warren, Christoph Beckermann, and Alain Karma. Phase-field simulation of solidification. *Annual review of materials research*, 32(1):163–194, 2002.

[16] Sha Yang, Fadi Aldakheel, Antonio Caggiano, Peter Wriggers, and Eddie Koenders. A review on cementitious self-healing and the potential of phase-field methods for modeling crack-closing and fracture recovery. *Materials*, 13(22):5265, 2020.

[17] Sha Yang, Neven Ukrainczyk, Antonio Caggiano, and Eddie Koenders. Numerical phase-field model validation for dissolution of minerals. *Applied Sciences*, 11(6):2464, 2021.

[18] Sha Yang, Yangyiwei Yang, Antonio Caggiano, Neven Ukrainczyk, and Eddie Koenders. A phase-field approach for portlandite carbonation and application to self-healing cementitious materials. *Materials and Structures*, 55(46):1–19, 2022.

[19] Edward Lansing Cussler and Edward Lansing Cussler. *Diffusion: mass transfer in fluid systems*. Cambridge university press, 2009.

[20] Adolf Fick. Ueber diffusion. *Annalen der Physik*, 170(1):59–86, 1855.

[21] William M Murphy, Eric H Oelkers, and Peter C Lichtner. Surface reaction versus diffusion control of mineral dissolution and growth rates in geochemical processes. *Chemical Geology*, 78(3-4):357–380, 1989.

[22] Arthur A Noyes and Willis R Whitney. The rate of solution of solid substances in their own solutions. *Journal of the American Chemical Society*, 19(12):930–934, 1897.

[23] Antonio C Lasaga. *Kinetic theory in the earth sciences*. Princeton university press, 2014.

[24] Zhijie Xu and Paul Meakin. Phase-field modeling of solute precipitation and dissolution. *The Journal of chemical physics*, 129(1):014705, 2008.

[25] KH Lieser. Steps in precipitation reactions. *Angewandte Chemie International Edition in English*, 8(3):188–202, 1969.

[26] Victor K LaMer and Robert H Dinegar. Theory, production and mechanism of formation of monodispersed hydrosols. *Journal of the American Chemical Society*, 72(11):4847–4854, 1950.

[27] Dhaval D Patel and Bradley D Anderson. Maintenance of supersaturation ii: indomethacin crystal growth kinetics versus degree of supersaturation. *Journal of pharmaceutical sciences*, 102(5):1544–1553, 2013.

[28] Hirozo Mihashi and Tomoya Nishiwaki. Development of engineered self-healing and self-repairing concrete-state-of-the-art report. *Journal of Advanced Concrete Technology*, 10(5):170–184, 2012.

[29] Kim Van Tittelboom, Elke Gruyaert, Hubert Rahier, and Nele De Belie. Influence of mix composition on the extent of autogenous crack healing by continued hydration or calcium carbonate formation. *Construction and Building Materials*, 37:349–359, 2012.

[30] Yingzi Yang, En-Hua Yang, and Victor C Li. Autogenous healing of engineered cementitious composites at early age. *Cement and concrete research*, 41(2):176–183, 2011.

[31] Haoliang Huang, Guang Ye, and Denis Damidot. Characterization and quantification of self-healing behaviors of microcracks due to further hydration in cement paste. *Cement and Concrete Research*, 52:71–81, 2013.

[32] Haoliang Huang and Guang Ye. Simulation of self-healing by further hydration in cementitious materials. *Cement and Concrete Composites*, 34(4):460–467, 2012.

[33] Nynke ter Heide and Erik Schlangen. Self-healing of early age cracks in concrete. In *First international conference on self healing materials*, pages 1–12, 2007.

[34] Carola Edvardsen. Water permeability and autogenous healing of cracks in concrete. *Materials Journal*, 96(4):448–454, 1999.

[35] CA Clear. The effects of autogenous healing upon the leakage of water through cracks in concrete. Technical report, 1985.

[36] Heinz Meichsner. Über die selbstdichtung von trennrissen in beton. *Beton-und Stahlbetonbau*, 87(4):95–99, 1992.

[37] Adam Neville. Autogenous healing—a concrete miracle? *Concrete international*, 24(11):76–82, 2002.

[38] Magdalena Rajczakowska, Karin Habermehl-Cwirzen, Hans Hedlund, and Andrzej Cwirzen. Autogenous self-healing: a better solution for concrete. *Journal of Materials in Civil Engineering*, 31(9):03119001, 2019.

[39] Haoliang Huang, Guang Ye, Chunxiang Qian, and Erik Schlangen. Self-healing in cementitious materials: Materials, methods and service conditions. *Materials & Design*, 92:499–511, 2016.

[40] Haoliang Huang. Thermodynamics of autogenous self-healing in cementitious materials. 2014.

[41] Yong-Soo Lee and Jae-Suk Ryou. Self healing behavior for crack closing of expansive agent via granulation/film coating method. *Construction and building Materials*, 71:188–193, 2014.

[42] TS Qureshi, Antonis Kanellopoulos, and Abir Al-Tabbaa. Encapsulation of expansive powder minerals within a concentric glass capsule system for self-healing concrete. *Construction and Building Materials*, 121:629–643, 2016.

[43] Tae-Ho Ahn and Toshiharu Kishi. Crack self-healing behavior of cementitious composites incorporating various mineral admixtures. *Journal of Advanced Concrete Technology*, 8(2):171–186, 2010.

[44] TH Ahn and T Kishi. The effect of geo-materials on the autogenous healing behavior of cracked concrete. *Concrete Repair, Rehabilitation and Retrofitting II, Cape Town, South Africa*, pages 125–126, 2008.

[45] Abdul Salam Buller, Kwang-Myong Lee, Seung Yup Jang, et al. Mechanical recovery of cracked fiber-reinforced mortar incorporating crystalline admixture, expansive agent, and geomaterial. *Advances in Materials Science and Engineering*, 2019, 2019.

[46] Marta Roig-Flores, S Moscato, P Serna, and Liberato Ferrara. Self-healing capability of concrete with crystalline admixtures in different environments. *Construction and Building Materials*, 86:1–11, 2015.

[47] Yusuf Çağatay Erşan, Emma Hernandez-Sanabria, Nico Boon, and Nele De Belie. Enhanced crack closure performance of microbial mortar through nitrate reduction. *Cement and concrete composites*, 70:159–170, 2016.

[48] Varenyam Achal, Abhijeet Mukerjee, and M Sudhakara Reddy. Biogenic treatment improves the durability and remediates the cracks of concrete structures. *Construction and Building Materials*, 48:1–5, 2013.

[49] JY Wang, Didier Snoeck, Sandra Van Vlierberghe, Willy Verstraete, and Nele De Belie. Application of hydrogel encapsulated carbonate precipitating bacteria for approaching a realistic self-healing in concrete. *Construction and building materials*, 68:110–119, 2014.

[50] Jianyun Wang, Kim Van Tittelboom, Nele De Belie, and Willy Verstraete. Use of silica gel or polyurethane immobilized bacteria for self-healing concrete. *Construction and building materials*, 26(1):532–540, 2012.

[51] Chun Xiang Qian, Mian Luo, Li Fu Ren, Rui Xing Wang, Rui Yang Li, Qing Feng Pan, and Huai Cheng Chen. Self-healing and repairing concrete cracks based on bio-mineralization. In *Key Engineering Materials*, volume 629, pages 494–503. Trans Tech Publ, 2015.

[52] Mohamed Alazhari, Trupti Sharma, Andrew Heath, Richard Cooper, and Kevin Paine. Application of expanded perlite encapsulated bacteria and growth media for self-healing concrete. *Construction and Building Materials*, 160:610–619, 2018.

[53] Zun-Xiang Hu, Xiang-Ming Hu, Wei-Min Cheng, Yan-Yun Zhao, and Ming-Yue Wu. Performance optimization of one-component polyurethane healing agent for self-healing concrete. *Construction and Building Materials*, 179:151–159, 2018.

[54] Carolyn M Dry. Design of self-growing, self-sensing, and self-repairing materials for engineering applications. In *Smart Materials*, volume 4234, pages 23–29. International Society for Optics and Photonics, 2001.

[55] Benoit Hilloulin, Kim Van Tittelboom, Elke Gruyaert, Nele De Belie, and Ahmed Loukili. Design of polymeric capsules for self-healing concrete. *Cement and Concrete Composites*, 55:298–307, 2015.

[56] Biqin Dong, Guohao Fang, Weijian Ding, Yuqing Liu, Jianchao Zhang, Ningxu Han, and Feng Xing. Self-healing features in cementitious material with urea–formaldehyde/epoxy microcapsules. *Construction and Building Materials*, 106:608–617, 2016.

[57] LS Dent Glasser, EE Lachowski, K Mohan, and HFW Taylor. A multi-method study of c3s hydration. *Cement and Concrete Research*, 8(6):733–739, 1978.

[58] K Sisomphon, O Copuroglu, and EAB Koenders. Self-healing of surface cracks in mortars with expansive additive and crystalline additive. *Cement and Concrete Composites*, 34(4):566–574, 2012.

[59] B Lubelli, TG Nijland, and RPJ Van Hees. Self-healing of lime based mortars: microscopy observations on case studies. *Heron, 56 (1/2)*, 2011.

[60] Aline de Souza Oliveira, Jo Dweck, Eduardo de Moraes Rego Fairbairn, Otávio da Fonseca Martins Gomes, and Romildo Dias Toledo Filho. Crystalline admixture effects on crystal formation phenomena during cement pastes' hydration. *Journal of Thermal Analysis and Calorimetry*, 139(6):3361–3375, 2020.

[61] John Johnston and Clinton Grove. The solubility of calcium hydroxide in aqueous salt solutions. *Journal of the American Chemical Society*, 53(11):3976–3991, 1931.

[62] Jean-Yves Gal, Jean-Claude Bollinger, Henri Tolosa, and Nathalie Gache. Calcium carbonate solubility: a reappraisal of scale formation and inhibition. *Talanta*, 43(9):1497–1509, 1996.

[63] Hao Liu, Haoliang Huang, Xintong Wu, Huixin Peng, Zhaoheng Li, Jie Hu, and Qijun Yu. Effects of external multi-ions and wet-dry cycles in a marine environment on autogenous self-healing of cracks in cement paste. *Cement and Concrete Research*, 120:198–206, 2019.

[64] R Alghamri, Antonis Kanellopoulos, and Abir Al-Tabbaa. Impregnation and encapsulation of lightweight aggregates for self-healing concrete. *Construction and Building Materials*, 124:910–921, 2016.

[65] Guohao Fang, Yuqing Liu, Shaofeng Qin, Weijian Ding, Jianchao Zhang, Shuxian Hong, Feng Xing, and Biqin Dong. Visualized tracing of crack self-healing features in cement/microcapsule system with x-ray microcomputed tomography. *Construction and building Materials*, 179:336–347, 2018.

[66] A Telesca, M Marroccoli, ML Pace, M Tomasulo, GL Valenti, and PJM Monteiro. A hydration study of various calcium sulfoaluminate cements. *Cement and Concrete Composites*, 53:224–232, 2014.

[67] L Zhang and FP Glasser. Hydration of calcium sulfoaluminate cement at less than 24 h. *Advances in cement research*, 14(4):141–155, 2002.

[68] Zhengwu Jiang, Wenting Li, and Zhengcheng Yuan. Influence of mineral additives and environmental conditions on the self-healing capabilities of cementitious materials. *Cement and Concrete Composites*, 57:116–127, 2015.

[69] A Ravitheja, T Chandra Sekhara Reddy, and C Sashidhar. Self-healing concrete with crystalline admixture—a review. *Journal of Wuhan University of Technology-Mater. Sci. Ed.*, 34(5):1143–1154, 2019.

[70] Kim Van Tittelboom, Nele De Belie, Willem De Muynck, and Willy Verstraete. Use of bacteria to repair cracks in concrete. *Cement and Concrete Research*, 40(1):157–166, 2010.

[71] Henk M Jonkers, Arjan Thijssen, Gerard Muyzer, Oguzhan Copuroglu, and Erik Schlangen. Application of bacteria as self-healing agent for the development of sustainable concrete. *Ecological engineering*, 36(2):230–235, 2010.

[72] Virginie Wiktor and Henk M Jonkers. Quantification of crack-healing in novel bacteria-based self-healing concrete. *Cement and Concrete Composites*, 33(7):763–770, 2011.

[73] Leon A Van Paassen, Claudia M Daza, Marc Staal, Dimitri Y Sorokin, Willem van der Zon, and Mark CM van Loosdrecht. Potential soil reinforcement by biological denitrification. *Ecological Engineering*, 36(2):168–175, 2010.

[74] Victoria S Whiffin, Leon A Van Paassen, and Marien P Harkes. Microbial carbonate precipitation as a soil improvement technique. *Geomicrobiology Journal*, 24(5):417–423, 2007.

[75] Willem De Muynck, Kathelijn Cox, Nele De Belie, and Willy Verstraete. Bacterial carbonate precipitation as an alternative surface treatment for concrete. *Construction and Building Materials*, 22(5):875–885, 2008.

[76] Henk M Jonkers and Erik Schlangen. Crack repair by concrete-immobilized bacteria. In *Proceedings of the first international conference on self healing materials*, volume 18, page 20, 2007.

[77] JY Wang, H Soens, Willy Verstraete, and Nele De Belie. Self-healing concrete by use of microencapsulated bacterial spores. *Cement and Concrete Research*, 56:139–152, 2014.

[78] Alex YK Ip and Shit F Chew. Ammonia production, excretion, toxicity, and defense in fish: a review. *Frontiers in physiology*, 1:134, 2010.

[79] Gupta Souradeep and Harn Wei Kua. Encapsulation technology and techniques in self-healing concrete. *Journal of Materials in Civil Engineering*, 28(12):04016165, 2016.

[80] Sanghyun Han, Eun Kyung Choi, Woojun Park, Chongku Yi, and Namhyun Chung. Effectiveness of expanded clay as a bacteria carrier for self-healing concrete. *Applied Biological Chemistry*, 62(1):19, 2019.

[81] Zhengxian Yang, John Hollar, Xiaodong He, and Xianming Shi. A self-healing cementitious composite using oil core/silica gel shell microcapsules. *Cement and Concrete Composites*, 33(4):506–512, 2011.

[82] Carolyn Dry. Procedures developed for self-repair of polymer matrix composite materials. *Composite structures*, 35(3):263–269, 1996.

[83] Carolyn Dry. Matrix cracking repair and filling using active and passive modes for smart timed release of chemicals from fibers into cement matrices. *Smart Materials and Structures*, 3(2):118, 1994.

[84] Carolyn Dry and William McMillan. Three-part methylmethacrylate adhesive system as an internal delivery system for smart responsive concrete. *Smart Materials and Structures*, 5(3):297, 1996.

[85] Kim Van Tittelboom. *Self-Healing Concrete through Incorporation of Encapsulated Bacteria-or Polymer-Based Healing Agents ('Zelfhelend beton door incorporatie van ingekapselde bacteri*. PhD thesis, Ghent University, 2012.

[86] Zhong Lv and Huisu Chen. Modeling self-healing efficiency on cracks due to unhydrated cement nuclei in cementitious materials: splitting crack mode. *Science and Engineering of Composite Materials*, 19(1):1–7, 2012.

[87] Giovanni Di Luzio, Liberato Ferrara, and Visar Krelani. A numerical model for the self-healing capacity of cementitious composites. *Proceedings of the Computational Modelling of Concrete Structures, St. Anton am Arlberg, Austria*, pages 24–27, 2014.

[88] Giovanni Di Luzio, Liberato Ferrara, and Visar Krelani. Numerical modeling of mechanical regain due to self-healing in cement based composites. *Cement and Concrete Composites*, 86:190–205, 2018.

[89] Liberato Ferrara, Giovanni DI LUZIO, Visar Krelani, et al. Experimental assessment and numerical modeling of self healing capacity of cement based materials via fracture mechanics concepts. In *FraMCoS 9*, pages 1–12, 2016.

[90] Adriana Silviana Chitez and Anthony Duncan Jefferson. A coupled thermo-hygro-chemical model for characterising autogenous healing in ordinary cementitious materials. *Cement and Concrete Research*, 88:184–197, 2016.

[91] Benoît Hilloulin, Frederic Grondin, Mohammed Matallah, and Ahmed Loukili. Modelling of autogenous healing in ultra high performance concrete. *Cement and Concrete Research*, 61:64–70, 2014.

[92] A Aliko-Benítez, M Doblaré, and JA Sanz-Herrera. Chemical-diffusive modeling of the self-healing behavior in concrete. *International Journal of Solids and Structures*, 69:392–402, 2015.

[93] H Ranaivomanana and N Benkemoun. Numerical modelling of the healing process induced by carbonation of a single crack in concrete structures: Theoretical formulation and embedded finite element method implementation. *Finite Elements in Analysis and Design*, 132:42–51, 2017.

[94] Serguey V Zemskov, Henk M Jonkers, and Fred J Vermolen. A mathematical model for bacterial self-healing of cracks in concrete. *Journal of Intelligent Material Systems and Structures*, 25(1):4–12, 2014.

[95] Brubeck Lee Freeman and Tony Jefferson. The simulation of transport processes in cementitious materials with embedded healing systems. *International Journal for Numerical and Analytical Methods in Geomechanics*, 44(2):293–326, 2020.

[96] Ahmed Ramadan Suleiman and Moncef L Nehdi. Modeling self-healing of concrete using hybrid genetic algorithm–artificial neural network. *Materials*, 10(2):135, 2017.

[97] Hehua Zhu, Shuai Zhou, Zhiguo Yan, Woody Ju, and Qing Chen. A 3d analytical model for the probabilistic characteristics of self-healing model for concrete using spherical microcapsule. *Computers and Concrete*, 15(1):37–54, 2015.

[98] Benoit Hilloulin, Damien Hilloulin, Frederic Grondin, Ahmed Loukili, and Nele De Belie. Mechanical regains due to self-healing in cementitious materials: Experimental measurements and micro-mechanical model. *Cement and Concrete Research*, 80:21–32, 2016.

[99] Robert Davies and Anthony Jefferson. Micromechanical modelling of self-healing cementitious materials. *International Journal of Solids and Structures*, 113:180–191, 2017.

[100] Yiming Zhang and Xiaoying Zhuang. A softening-healing law for self-healing quasi-brittle materials: analyzing with strong discontinuity embedded approach. *Engineering Fracture Mechanics*, 192:290–306, 2018.

[101] Rashid K Abu Al-Rub and Ammar Alsheghri. Cohesive zone damage-healing model for self-healing materials. In *Applied Mechanics and Materials*, volume 784, pages 111–118. Trans Tech Publ, 2015.

[102] B Savija and E Schlangen. Modelling the influence of cracking and healing on modal properties of concrete beams. In *ICSHM 2015: Proceedings of the 5th International Conference on Self-Healing Materials, Durham, USA, 22-24 June 2015*, 2015.

[103] Julia Mergheim and Paul Steinmann. Phenomenological modelling of self-healing polymers based on integrated healing agents. *Computational Mechanics*, 52(3):681–692, 2013.

[104] Ever J Barbero and Kevin J Ford. Characterization of self-healing fiber-reinforced polymer-matrix composite with distributed damage. *JOURNAL OF ADVANCED MATERIALS-COVINA-*, 39(4):20, 2007.

[105] Joris JC Remmers and René de Borst. Numerical modelling of self healing mechanisms. In *Self Healing Materials*, pages 365–380. Springer, 2007.

[106] Shuai Zhou, Hehua Zhu, J Woody Ju, Zhiguo Yan, and Qing Chen. Modeling microcapsule-enabled self-healing cementitious composite materials using discrete element method. *International Journal of Damage Mechanics*, 26(2):340–357, 2017.

[107] FA Gilabert, D Garoz, and Wim Van Paepegem. Macro-and micro-modeling of crack propagation in encapsulation-based self-healing materials: Application of xfem and cohesive surface techniques. *Materials & Design*, 130:459–478, 2017.

[108] Tobias Hazelwood, Anthony Duncan Jefferson, Robert John Lark, and Diane Ruth Gardner. Numerical simulation of the long-term behaviour of a self-healing concrete beam vs standard reinforced concrete. *Engineering Structures*, 102:176–188, 2015.

[109] Shuai Zhou, Hehua Zhu, Zhiguo Yan, J Woody Ju, and Lianyang Zhang. A micromechanical study of the breakage mechanism of microcapsules in concrete using pfc2d. *Construction and Building Materials*, 115:452–463, 2016.

[110] Masoud K Darabi, Rashid K Abu Al-Rub, and Dallas N Little. A continuum damage mechanics framework for modeling micro-damage healing. *International Journal of Solids and Structures*, 49(3-4):492–513, 2012.

[111] Shuke Miao, Ming L Wang, and Howard L Schreyer. Constitutive models for healing of materials with application to compaction of crushed rock salt. *Journal of Engineering Mechanics*, 121(10):1122–1129, 1995.

[112] Ever J Barbero, Fabrizio Greco, and Paolo Lonetti. Continuum damage-healing mechanics with application to self-healing composites. *International Journal of Damage Mechanics*, 14(1):51–81, 2005.

[113] Ammar A Alsheghri and Rashid K Abu Al-Rub. Thermodynamic-based cohesive zone healing model for self-healing materials. *Mechanics Research Communications*, 70:102–113, 2015.

[114] Ammar A Alsheghri and Rashid K Abu Al-Rub. Finite element implementation and application of a cohesive zone damage-healing model for self-healing materials. *Engineering Fracture Mechanics*, 163:1–22, 2016.

[115] Antonio Caggiano, Guillermo Etse, Liberato Ferrara, and Visar Krelani. Zero-thickness interface constitutive theory for concrete self-healing effects. *Computers & Structures*, 186:22–34, 2017.

[116] Josef Stefan. Uber einige probleme der theorie der warmeletung. *Sitzer. Wien. Akad. Math. Naturw.*, 98:473–484, 1889.

[117] Johan Stefan. Über die theorie der eisbildung, insbesondere über die eisbildung im polarmeere. *Annalen der Physik und Chemie*, 42:269–286, 1891.

[118] Marcela Quilaqueo and José Miguel Aguilera. Dissolution of nacl crystals in artificial saliva and water by video-microscopy. *Food Research International*, 69:373–380, 2015.

[119] Ben Q Li. *Discontinuous finite elements in fluid dynamics and heat transfer*. Springer Science & Business Media, 2006.

[120] YF Zhou, LG Tham, RWM Yan, and L Xu. The mechanism of soil failures along cracks subjected to water infiltration. *Computers and Geotechnics*, 55:330–341, 2014.

[121] G Krielaaif, RA Hubert, and Y Houbaerf. Some applications of moving boundary problems in solid state steel metallurgy. *WIT Transactions on Modelling and Simulation*, 18, 1997.

[122] SELÇUK Kutluay, AR Bahadir, and A Özdeş. The numerical solution of one-phase classical stefan problem. *Journal of computational and applied mathematics*, 81(1):135–144, 1997.

[123] Huaqing Ma and Yongzhi Zhao. An approach to distribute the marker points on non-spherical particle/boundary surface within the ibm-lbm framework. *Engineering Analysis with Boundary Elements*, 108:254–266, 2019.

[124] S Chen, B Merriman, Smereka Osher, and P Smereka. A simple level set method for solving stefan problems. *Journal of Computational Physics*, 135(1):8–29, 1997.

[125] Hui Liu, Ye Tian, Hongming Zong, Qingping Ma, Michael Yu Wang, and Liang Zhang. Fully parallel level set method for large-scale structural topology optimization. *Computers & Structures*, 221:13–27, 2019.

[126] Cyril W Hirt and Billy D Nichols. Volume of fluid (vof) method for the dynamics of free boundaries. *Journal of computational physics*, 39(1):201–225, 1981.

[127] V Voller and M Cross. Accurate solutions of moving boundary problems using the enthalpy method. *International journal of heat and mass transfer*, 24(3):545–556, 1981.

[128] Mohamed Zerroukat, Mohamed Zerroukat, and CR Chatwin. *Computational moving boundary problems*, volume 8. * Research Studies Press, 1994.

[129] Wei Shyy, HS Udaykumar, and Madhukar M Rao. *Computational fluid dynamics with moving boundaries*. CRC Press, 1995.

[130] HS Udaykumar, Rajat Mittal, and Wei Shyy. Computation of solid–liquid phase fronts in the sharp interface limit on fixed grids. *Journal of computational physics*, 153(2):535–574, 1999.

[131] Holavanahalli S Udaykumar, Wei Shyy, and Madhukar M Rao. Elafint: a mixed eulerian–lagrangian method for fluid flows with complex and moving boundaries. *International journal for numerical methods in fluids*, 22(8):691–712, 1996.

[132] Mohammad Ali Ansari, Reza Abdi Behnagh, and Alberto Salvadori. Numerical analysis of high-speed water jet spot welding using the arbitrary lagrangian-eulerian (ale) method. *The International Journal of Advanced Manufacturing Technology*, 112(1):491–504, 2021.

[133] Robert F Sekerka. Morphology: from sharp interface to phase field models. *Journal of crystal growth*, 264(4):530–540, 2004.

[134] Nikolas Provatas and Ken Elder. *Phase-field methods in materials science and engineering*. John Wiley & Sons, 2011.

[135] Ingo Steinbach. Phase-field models in materials science. *Modelling and simulation in materials science and engineering*, 17(7):073001, 2009.

[136] Nele Moelans, Bart Blanpain, and Patrick Wollants. An introduction to phase-field modeling of microstructure evolution. *Calphad*, 32(2):268–294, 2008.

[137] Lev Davidovich Landau. *The classical theory of fields*, volume 2. Elsevier, 2013.

[138] Oliver Penrose and Paul C Fife. Thermodynamically consistent models of phase-field type for the kinetic of phase transitions. *Physica D: Nonlinear Phenomena*, 43(1):44–62, 1990.

[139] Alain Karma and Wouter-Jan Rappel. Phase-field method for computationally efficient modeling of solidification with arbitrary interface kinetics. *Physical review E*, 53(4):R3017, 1996.

[140] HM Flower and PJ Gregson. Solid state phase transformations in aluminium alloys containing lithium. *Materials science and technology*, 3(2):81–90, 1987.

[141] Ingo Steinbach and Markus Apel. Multi phase field model for solid state transformation with elastic strain. *Physica D: Nonlinear Phenomena*, 217(2):153–160, 2006.

[142] CE Krill Iii and L-Q Chen. Computer simulation of 3-d grain growth using a phase-field model. *Acta materialia*, 50(12):3059–3075, 2002.

[143] Nele Moelans, Bart Blanpain, and Patrick Wollants. Quantitative analysis of grain boundary properties in a generalized phase field model for grain growth in anisotropic systems. *Physical Review B*, 78(2):024113, 2008.

[144] A Kazaryan, Y Wang, SA Dregia, and Bruce R Patton. Generalized phase-field model for computer simulation of grain growth in anisotropic systems. *Physical Review B*, 61(21):14275, 2000.

[145] Yifei Zeng, Abigail Hunter, Irene Jane Beyerlein, and Marisol Koslowski. A phase field dislocation dynamics model for a bicrystal interface system: An investigation into dislocation slip transmission across cube-on-cube interfaces. *International Journal of Plasticity*, 79:293–313, 2016.

[146] Valery I Levitas and Arunabha M Roy. Multiphase phase field theory for temperature-induced phase transformations: Formulation and application to interfacial phases. *Acta Materialia*, 105:244–257, 2016.

[147] Hamed Ravash, Liesbeth Vanherpe, Jef Vleugels, and Nele Moelans. Three-dimensional phase-field study of grain coarsening and grain shape accommodation in the final stage of liquid-phase sintering. *Journal of the European Ceramic Society*, 37(5):2265–2275, 2017.

[148] Klaus Deckelnick, Charles M Elliott, and Vanessa Styles. Double obstacle phase field approach to an inverse problem for a discontinuous diffusion coefficient. *Inverse Problems*, 32(4):045008, 2016.

[149] Vili Heinonen, CV Achim, JM Kosterlitz, See-Chen Ying, J Lowengrub, and T Ala-Nissila. Consistent hydrodynamics for phase field crystals. *Physical review letters*, 116(2):024303, 2016.

[150] Nan Wang, Kirk H Bevan, and Nikolas Provatas. Phase-field-crystal model for electromigration in metal interconnects. *Physical review letters*, 117(15):155901, 2016.

[151] Christian Miehe, Martina Hofacker, and Fabian Welschinger. A phase field model for rate-independent crack propagation: Robust algorithmic implementation based on operator splits. *Computer Methods in Applied Mechanics and Engineering*, 199(45-48):2765–2778, 2010.

[152] Robert Spatschek, Efim Brener, and Alain Karma. Phase field modeling of crack propagation. *Philosophical Magazine*, 91(1):75–95, 2011.

[153] Robert Spatschek, Miks Hartmann, Efim Brener, Heiner Müller-Krumbhaar, and Klaus Kassner. Phase field modeling of fast crack propagation. *Physical review letters*, 96(1):015502, 2006.

[154] Alain Karma and Alexander E Lobkovsky. Unsteady crack motion and branching in a phase-field model of brittle fracture. *Physical review letters*, 92(24):245510, 2004.

[155] Hervé Henry and Herbert Levine. Dynamic instabilities of fracture under biaxial strain using a phase field model. *Physical review letters*, 93(10):105504, 2004.

[156] Herbert B Callen. Thermodynamics and an introduction to thermostatistics, 1998.

[157] Mark Waldo Zemansky et al. Heat and thermodynamics. 1943.

[158] Martin Z Bazant. Theory of chemical kinetics and charge transfer based on nonequilibrium thermodynamics. *Accounts of chemical research*, 46(5):1144–1160, 2013.

[159] Qing Jiang and Zi Wen. Thermodynamics of phase transitions. In *Thermodynamics of Materials*, pages 157–206. Springer, 2011.

[160] Elias P Gyftopoulos and Gian Paolo Beretta. *Thermodynamics: foundations and applications*. Courier Corporation, 2005.

[161] Ralph Baierlein. The elusive chemical potential. *American Journal of Physics*, 69(4):423–434, 2001.

[162] Masakatsu Hasegawa. Thermodynamic basis for phase diagrams. In *Treatise on Process Metallurgy*, pages 527–556. Elsevier, 2014.

[163] WJ Knapp. Use of free energy data in the construction of phase diagrams. *Journal of the American Ceramic Society*, 36(2):43–47, 1953.

[164] YL Li, SY Hu, ZK Liu, and LQ Chen. Phase-field model of domain structures in ferroelectric thin films. *Applied Physics Letters*, 78(24):3878–3880, 2001.

[165] Long-Qing Chen. Phase-field method of phase transitions/domain structures in ferroelectric thin films: a review. *Journal of the American Ceramic Society*, 91(6):1835–1844, 2008.

[166] Sha Yang, Antonio Caggiano, Min Yi, Neven Ukrainczyk, and E.A.B Koenders. Modelling autogenous self-healing with dissoluble encapsulated particles using a phase field approach. In *Mecánica Computacional*, pages 1457–1467, 2019.

[167] Samuel M Allen and John W Cahn. A microscopic theory for antiphase boundary motion and its application to antiphase domain coarsening. *Acta metallurgica*, 27(6):1085–1095, 1979.

[168] Weijie Mai, Soheil Soghrati, and Rudolph G Buchheit. A phase field model for simulating the pitting corrosion. *Corrosion Science*, 110:157–166, 2016.

[169] BC Han, A Van der Ven, D Morgan, and G Ceder. Electrochemical modeling of intercalation processes with phase field models. *Electrochimica Acta*, 49(26):4691–4699, 2004.

[170] John W Cahn and John E Hilliard. Free energy of a nonuniform system. i. interfacial free energy. *The Journal of chemical physics*, 28(2):258–267, 1958.

[171] YM Jin, Andrei Artemev, and AG Khachaturyan. Three-dimensional phase field model of low-symmetry martensitic transformation in polycrystal: simulation of ζ 2 martensite in aucd alloys. *Acta Materialia*, 49(12):2309–2320, 2001.

[172] RS Qin, ER Wallach, and RC Thomson. A phase-field model for the solidification of multi-component and multiphase alloys. *Journal of crystal growth*, 279(1-2):163–169, 2005.

[173] Britta Nestler, Harald Garcke, and Björn Stinner. Multicomponent alloy solidification: phase-field modeling and simulations. *Physical Review E*, 71(4):041609, 2005.

[174] Junseok Kim. Phase-field models for multi-component fluid flows. *Communications in Computational Physics*, 12(3):613–661, 2012.

[175] Britta Nestler, Frank Wendler, Michael Selzer, Björn Stinner, and Harald Garcke. Phase-field model for multiphase systems with preserved volume fractions. *Physical Review E*, 78(1):011604, 2008.

[176] Ingo Steinbach, Franco Pezzolla, Britta Nestler, Markus Seeßelberg, Robert Prieler, Georg J Schmitz, and Joao LL Rezende. A phase field concept for multiphase systems. *Physica D: Nonlinear Phenomena*, 94(3):135–147, 1996.

[177] Adam A Wheeler, William J Boettinger, and Geoffrey B McFadden. Phase-field model for isothermal phase transitions in binary alloys. *Physical Review A*, 45(10):7424, 1992.

[178] Adam A Wheeler, GB McFadden, and WJ Boettinger. Phase-field model for solidification of a eutectic alloy. *Proceedings of the Royal Society of London. Series A: Mathematical, Physical and Engineering Sciences*, 452(1946):495–525, 1996.

[179] Janin Tiaden, Britta Nestler, Hermann-Josef Diepers, and Ingo Steinbach. The multiphase-field model with an integrated concept for modelling solute diffusion. *Physica D: Nonlinear Phenomena*, 115(1-2):73–86, 1998.

[180] W Losert, DA Stillman, HZ Cummins, P Kopczyński, W-J Rappel, and A Karma. Selection of doublet cellular patterns in directional solidification through spatially periodic perturbations. *Physical Review E*, 58(6):7492, 1998.

[181] James A Warren and William J Boettinger. Prediction of dendritic growth and microsegregation patterns in a binary alloy using the phase-field method. *Acta Metallurgica et Materialia*, 43(2):689–703, 1995.

[182] Weijie Mai and Soheil Soghrati. New phase field model for simulating galvanic and pitting corrosion processes. *Electrochimica Acta*, 260:290–304, 2018.

[183] J Eiken, B Böttger, and I Steinbach. Multiphase-field approach for multicomponent alloys with extrapolation scheme for numerical application. *Physical review E*, 73(6):066122, 2006.

[184] Ricard González-Cinca, Roger Folch, R Benitez, L Ramirez-Piscina, Jaume Casademunt, and A Hernández-Machado. Phase-field models in interfacial pattern formation out of equilibrium. *arXiv preprint cond-mat/0305058*, 2003.

[185] Machiko Ode, Jae Sang Lee, Seong Gyoon Kim, Won Tae Kim, and Toshio Suzuki. Phase-field model for solidification of ternary alloys. *ISIJ international*, 40(9):870–876, 2000.

[186] Seong Gyoon Kim, Won Tae Kim, and Toshio Suzuki. Interfacial compositions of solid and liquid in a phase-field model with finite interface thickness for isothermal solidification in binary alloys. *Physical Review E*, 58(3):3316, 1998.

[187] MS Shetty. Concrete technology, s. *Chand and Company Ltd, New Delhi*, 2005.

[188] Leonid I Perlovsky. Conundrum of combinatorial complexity. *IEEE Transactions on Pattern Analysis and Machine Intelligence*, 20(6):666–670, 1998.

[189] MF Kaplan. Crack propagation and the fracture of concrete. In *Journal Proceedings*, volume 58, pages 591–610, 1961.

[190] Robert J Frosch. Another look at cracking and crack control in reinforced concrete. *Structural Journal*, 96(3):437–442, 1999.

[191] Arne Hillerborg, Mats Modéer, and P-E Petersson. Analysis of crack formation and crack growth in concrete by means of fracture mechanics and finite elements. *Cement and concrete research*, 6(6):773–781, 1976.

[192] JP Roumaldi and Gordon B Batson. Mechanics of crack arrest in concrete. Technical report, 2008.

[193] Liberato Ferrara, Estefania Cuenca Asensio, Francesco Lo Monte, Marta Roig Flores, Mercedes Sanchez Moreno, Didier Snoeck, Tim Van Mullem, and Nele De Belie. Experimental characterization of the self-healing capacity of cement based materials: an overview. In *Multidisciplinary Digital Publishing Institute Proceedings*, volume 2, page 454, 2018.

[194] Liberato Ferrara, Tim Van Mullem, Maria Cruz Alonso, Paola Antonaci, Ruben Paul Borg, Estefania Cuenca, Anthony Jefferson, Pui-Lam Ng, Alva Peled, Marta Roig-Flores, et al. Experimental characterization of the self-healing capacity of cement based materials and its effects on the material performance: A state of the art report by cost action sarcos wg2. *Construction and Building Materials*, 167:115–142, 2018.

[195] Kim Van Tittelboom and Nele De Belie. Self-healing in cementitious materials—a review. *Materials*, 6(6):2182–2217, 2013.

[196] Nataliya Hearn. Self-sealing, autogenous healing and continued hydration: what is the difference? *Materials and structures*, 31(8):563, 1998.

[197] EAB Koenders, N UKRAINCZYK, and A CAGGIANO. Modelling the self-healing potential of dissoluble encapsulated cement.

[198] Haoliang Huang, Guang Ye, and Denis Damidot. Effect of blast furnace slag on self-healing of microcracks in cementitious materials. *Cement and concrete research*, 60:68–82, 2014.

[199] Henk M Jonkers. Self healing concrete: a biological approach. In *Self healing materials*, pages 195–204. Springer, 2007.

[200] Swapan Kumar Ghosh. *Self-healing materials: fundamentals, design strategies, and applications*. Wiley Online Library, 2009.

[201] Victor C Li and En-Hua Yang. Self healing in concrete materials. In *Self healing materials*, pages 161–193. Springer, 2007.

[202] Didier Snoeck and Nele De Belie. Repeated autogenous healing in strain-hardening cementitious composites by using superabsorbent polymers. *Journal of Materials in Civil Engineering*, 28(1):04015086, 2016.

[203] Didier Snoeck and Nele De Belie. From straw in bricks to modern use of microfibers in cementitious composites for improved autogenous healing–a review. *Construction and Building Materials*, 95:774–787, 2015.

[204] Joseph D Rule, Eric N Brown, Nancy R Sottos, Scott R White, and Jeffrey S Moore. Wax-protected catalyst microspheres for efficient self-healing materials. *Advanced Materials*, 17(2):205–208, 2005.

[205] Biqin Dong, Weijian Ding, Shaofeng Qin, Ningxu Han, Guohao Fang, Yuqing Liu, Feng Xing, and Shuxian Hong. Chemical self-healing system with novel microcapsules for corrosion inhibition of rebar in concrete. *Cement and Concrete Composites*, 85:83–91, 2018.

[206] Didier Snoeck, Kim Van Tittelboom, Stijn Steuperaert, Peter Dubruel, and Nele De Belie. Self-healing cementitious materials by the combination of microfibres and superabsorbent polymers. *Journal of Intelligent Material Systems and Structures*, 25(1):13–24, 2014.

[207] Rami Alghamri, Antonios Kanellopoulos, Chrysoula Litina, and Abir Al-Tabbaa. Preparation and polymeric encapsulation of powder mineral pellets for self-healing cement based materials. *Construction and Building Materials*, 186:247–262, 2018.

[208] Marta Roig-Flores, F Pirritano, P Serna, and Liberato Ferrara. Effect of crystalline admixtures on the self-healing capability of early-age concrete studied by means of permeability and crack closing tests. *Construction and Building Materials*, 114:447–457, 2016.

[209] Noel Peter Bengzon Tan, Lok Hang Keung, Wing Ho Choi, Wai Chak Lam, and Hei Nga Leung. Silica-based self-healing microcapsules for self-repair in concrete. *Journal of Applied Polymer Science*, 133(12), 2016.

[210] Serguey V Zemskov, Henk M Jonkers, and Fred J Vermolen. Mathematical models to predict the critical conditions for bacterial self-healing of concrete. In *International Conference on Mathematical Modeling and Computational Physics*, pages 108–121. Springer, 2011.

[211] Long-Qing Chen. Phase-field models for microstructure evolution. *Annual review of materials research*, 32(1):113–140, 2002.

[212] Shiyan Pan and Mingfang Zhu. A three-dimensional sharp interface model for the quantitative simulation of solutal dendritic growth. *Acta Materialia*, 58(1):340–352, 2010.

[213] F Bangert, D Kuhl, and G Meschke. Chemo-hygro-mechanical modelling and numerical simulation of concrete deterioration caused by alkali-silica reaction. *International Journal for Numerical and Analytical Methods in Geomechanics*, 28(7-8):689–714, 2004.

[214] Haifeng Wang, Feng Liu, Haimin Zhai, and Kang Wang. Application of the maximal entropy production principle to rapid solidification: a sharp interface model. *Acta materialia*, 60(4):1444–1454, 2012.

[215] Lina Ma, Rui Chen, Xiaofeng Yang, and Hui Zhang. Numerical approximations for allen-cahn type phase field model of two-phase incompressible fluids with moving contact lines. *Communications in Computational Physics*, 21(3):867–889, 2017.

[216] Héctor Gómez, Victor M Calo, Yuri Bazilevs, and Thomas JR Hughes. Isogeometric analysis of the cahn–hilliard phase-field model. *Computer methods in applied mechanics and engineering*, 197(49-50):4333–4352, 2008.

[217] Amirreza Talaiekhozan, Ali Keyvanfar, Arezo Shafaghat, Ramin Andalib, MA Majid, Mohamad Ali Fulazzaky, Rosli Mohamad Zin, Chew Tin Lee, Mohd Warid Hussin, Norhaliza Hamzah, et al. A review of self-healing concrete research development. *Journal of Environmental Treatment Techniques*, 2(1):1–11, 2014.

[218] Salmabanu Luhar and Suthar Gourav. A review paper on self healing concrete. *Journal of Civil Engineering Research*, 5(3):53–58, 2015.

[219] Kim Van Tittelboom, Nele De Belie, Frank Lehmann, and Christian U Grosse. Acoustic emission analysis for the quantification of autonomous crack healing in concrete. *Construction and Building Materials*, 28(1):333–341, 2012.

[220] Liberato Ferrara, Visar Krelani, and Maddalena Carsana. A "fracture testing" based approach to assess crack healing of concrete with and without crystalline admixtures. *Construction and Building Materials*, 68:535–551, 2014.

[221] HW Reinhardt, H Jonkers, Kim Van Tittelboom, Didier Snoeck, Nele De Belie, Willem De Muynck, Willy Verstraete, Jianyun Wang, and V Mechtcherine. Recovery against environmental action. In *Self-healing phenomena in cement-based materials*, pages 65–117. Springer, 2013.

[222] Tanvir Qureshi, Antonios Kanellopoulos, and Abir Al-Tabbaa. Autogenous self-healing of cement with expansive minerals-i: Impact in early age crack healing. *Construction and Building Materials*, 192:768–784, 2018.

[223] Hans-Wolf Reinhardt and Martin Jooss. Permeability and self-healing of cracked concrete as a function of temperature and crack width. *Cement and concrete research*, 33(7):981–985, 2003.

[224] Tony Jefferson, Etelvina Javierre, Brubeck Freeman, Ali Zaoui, Eddie Koenders, and Liberato Ferrara. Research progress on numerical models for self-healing cementitious materials. *Advanced materials interfaces*, 5(17):1701378, 2018.

[225] Souradeep Gupta, Sze Dai Pang, and Harn Wei Kua. Autonomous healing in concrete by bio-based healing agents–a review. *Construction and Building Materials*, 146:419–428, 2017.

[226] Henk M Jonkers. Bacteria-based self-healing concrete. *Heron, 56 (1/2)*, 2011.

[227] Jian-Ying Wang, Nele De Belie, and Willy Verstraete. Diatomaceous earth as a protective vehicle for bacteria applied for self-healing concrete. *Journal of industrial microbiology & biotechnology*, 39(4):567–577, 2012.

[228] Mian Luo, Chun-xiang Qian, and Rui-yang Li. Factors affecting crack repairing capacity of bacteria-based self-healing concrete. *Construction and building materials*, 87:1–7, 2015.

[229] Jianyun Wang, Arn Mignon, Didier Snoeck, Virginie Wiktor, Sandra Van Vliergerghe, Nico Boon, and Nele De Belie. Application of modified-alginate encapsulated carbonate producing bacteria in concrete: a promising strategy for crack self-healing. *Frontiers in microbiology*, 6:1088, 2015.

[230] Wasim Khaliq and Muhammad Basit Ehsan. Crack healing in concrete using various bio influenced self-healing techniques. *Construction and Building Materials*, 102:349–357, 2016.

[231] Tran Diep Phuoc Thao, Tay Jang Shen Johnson, Quek Ser Tong, and Pang Sze Dai. Implementation of self-healing in concrete–proof of concept. *The IES Journal Part A: Civil & Structural Engineering*, 2(2):116–125, 2009.

[232] Bjorn Van Belleghem, Sylvia Kessler, Philip Van den Heede, Kim Van Tittelboom, and Nele De Belie. Chloride induced reinforcement corrosion behavior in self-healing concrete with encapsulated polyurethane. *Cement and Concrete Research*, 113:130–139, 2018.

[233] Dechkhachorn Jaroenratanapirom and Raktipong Sahamitmongkol. Effects of different mineral additives and cracking ages on self-healing performance of mortar. In *Proceedings of the 6th Annual Concrete Conference, Phetchaburi, Thailand*, pages 551–556, 2010.

[234] Zhengwu Jiang, Wenting Li, Zhengzheng Yuan, and Zhenghong Yang. Self-healing of cracks in concrete with various crystalline mineral additives in underground environment. *Journal of Wuhan University of Technology-Mater. Sci. Ed.*, 29(5):938–944, 2014.

[235] Antonis Kanellopoulos, TS Qureshi, and Abir Al-Tabbaa. Glass encapsulated minerals for self-healing in cement based composites. *Construction and Building Materials*, 98:780–791, 2015.

[236] Sandra S Lucas, Chris Moxham, Eirini Tziviloglou, and Henk Jonkers. Study of self-healing properties in concrete with bacteria encapsulated in expanded clay. *Science and Technology of Materials*, 30:93–98, 2018.

[237] Henk M Jonkers and Erik Schlangen. A two component bacteria-based self-healing concrete. In *Proceedings of the 2nd International Conference on Concrete Repair, Rehabilitation and Retrofitting*, pages 119–120, 2008.

[238] Harn Wei Kua, Souradeep Gupta, Anastasia N Aday, and Wil V Srubar III. Biochar-immobilized bacteria and superabsorbent polymers enable self-healing of fiber-reinforced concrete after multiple damage cycles. *Cement and Concrete Composites*, 100:35–52, 2019.

[239] Mingyue Wu, Xiangming Hu, Qian Zhang, Di Xue, and Yanyun Zhao. Growth environment optimization for inducing bacterial mineralization and its application in concrete healing. *Construction and Building Materials*, 209:631–643, 2019.

[240] Victor C Li and Emily Herbert. Robust self-healing concrete for sustainable infrastructure. *Journal of Advanced Concrete Technology*, 10(6):207–218, 2012.

[241] Yun Suk Lee and Woojun Park. Current challenges and future directions for bacterial self-healing concrete. *Applied microbiology and biotechnology*, 102(7):3059–3070, 2018.

[242] MS Rao, V Srinivasa Reddy, M Hafsa, P Veena, and P Anusha. Bioengineered concrete-a sustainable self-healing construction material. *Research journal of engineering sciences ISSN*, 2278:9472, 2013.

[243] Jing Xu and Wu Yao. Multiscale mechanical quantification of self-healing concrete incorporating non-ureolytic bacteria-based healing agent. *Cement and concrete research*, 64:1–10, 2014.

[244] Mostafa Seifan, Ali Khajeh Samani, and Aydin Berenjian. Bioconcrete: next generation of self-healing concrete. *Applied microbiology and biotechnology*, 100(6):2591–2602, 2016.

[245] Nasiru Zakari Muhammad, Arezou Shafaghat, Ali Keyvanfar, Muhd Zaimi Abd Majid, SK Ghoshal, Seyed Esmaeil Mohammadyan Yasouj, Abideen Adekunle Ganiyu, Mostafa Samadi Kouchaksaraei, Hesam Kamyab, Mohammad Mahdi Taheri, et al. Tests and methods of evaluating the self-healing efficiency of concrete: A review. *Construction and Building Materials*, 112:1123–1132, 2016.

[246] Kim Van Tittelboom, Eleni Tsangouri, Danny Van Hemelrijck, and Nele De Belie. The efficiency of self-healing concrete using alternative manufacturing procedures and more realistic crack patterns. *Cement and concrete composites*, 57:142–152, 2015.

[247] Jody WC Pang and Ian P Bond. A hollow fibre reinforced polymer composite encompassing self-healing and enhanced damage visibility. *Composites Science and Technology*, 65(11-12):1791–1799, 2005.

[248] Yong Zhu, Xiao Ji Ye, Min Zhi Rong, and Ming Qiu Zhang. Self-healing glass fiber/epoxy composites with polypropylene tubes containing self-pressurized epoxy and mercaptan healing agents. *Composites Science and Technology*, 135:146–152, 2016.

[249] Mingxing Huang, He Zhang, and Jinglei Yang. Synthesis of organic silane microcapsules for self-healing corrosion resistant polymer coatings. *Corrosion Science*, 65:561–566, 2012.

[250] Jie Shen, Xiaofeng Yang, and Qi Wang. Mass and volume conservation in phase field models for binary fluids. *Communications in Computational Physics*, 13(4):1045–1065, 2013.

[251] Christian Miehe, Fabian Welschinger, and Martina Hofacker. Thermodynamically consistent phase-field models of fracture: Variational principles and multi-field fe implementations. *International Journal for Numerical Methods in Engineering*, 83(10):1273–1311, 2010.

[252] L Gránásy, T Pusztai, T Börzsönyi, G Tóth, G Tegze, JA Warren, and JF Douglas. Phase field theory of crystal nucleation and polycrystalline growth: A review. *Journal of materials research*, 21(2):309–319, 2006.

[253] Ingo Steinbach. Phase-field model for microstructure evolution at the mesoscopic scale. *Annual Review of Materials Research*, 43:89–107, 2013.

[254] Michael Greenwood, Nikolas Provatas, and Jörg Rottler. Free energy functionals for efficient phase field crystal modeling of structural phase transformations. *Physical review letters*, 105(4):045702, 2010.

[255] Gunduz Caginalp and Paul Fife. Phase-field methods for interfacial boundaries. *Physical Review B*, 33(11):7792, 1986.

[256] Vitaly L Ginzburg and Lev D Landau. On the theory of superconductivity. In *On Superconductivity and Superfluidity*, pages 113–137. Springer, 2009.

[257] Fadi Aldakheel. *Mechanics of nonlocal dissipative solids: gradient plasticity and phase field modeling of ductile fracture*. Stuttgart: Institut für Mechanik (Bauwesen), Lehrstuhl I, Universität Stuttgart, 2016. http://dx.doi.org/10.18419/opus-8803.

[258] Fadi Aldakheel. A microscale model for concrete failure in poro-elasto-plastic media. *Theoretical and Applied Fracture Mechanics*, 107:102517, 2020.

[259] RS Qin and HK Bhadeshia. Phase field method. *Materials science and technology*, 26(7):803–811, 2010.

[260] Alain Karma and Wouter-Jan Rappel. Quantitative phase-field modeling of dendritic growth in two and three dimensions. *Physical review E*, 57(4):4323, 1998.

[261] Alain Karma and Wouter-Jan Rappel. Phase-field model of dendritic sidebranching with thermal noise. *Physical review E*, 60(4):3614, 1999.

[262] Hossein Jafarzadeh, Gholam Hossein Farrahi, and Mahdi Javanbakht. Phase field modeling of crack growth with double-well potential including surface effects. *Continuum Mechanics and Thermodynamics*, 32(3):913–925, 2020.

[263] SY Hu, YL Li, YX Zheng, and LQ Chen. Effect of solutes on dislocation motion—a phase-field simulation. *International Journal of Plasticity*, 20(3):403–425, 2004.

[264] Marisol Koslowski, Alberto M Cuitino, and Michael Ortiz. A phase-field theory of dislocation dynamics, strain hardening and hysteresis in ductile single crystals. *Journal of the Mechanics and Physics of Solids*, 50(12):2597–2635, 2002.

[265] Yan-Mei Yu, Bang-Gui Liu, and Axel Voigt. Phase-field modeling of anomalous spiral step growth on si (001) surface. *Physical Review B*, 79(23):235317, 2009.

[266] Gunduz Caginalp and Weiqing Xie. Phase-field and sharp-interface alloy models. *Physical Review E*, 48(3):1897, 1993.

[267] Joseph B Collins and Herbert Levine. Diffuse interface model of diffusion-limited crystal growth. *Physical Review B*, 31(9):6119, 1985.

[268] Adam A Wheeler, Bruce T Murray, and Robert J Schaefer. Computation of dendrites using a phase field model. *Physica D: Nonlinear Phenomena*, 66(1-2):243–262, 1993.

[269] Shun-Lien Wang and Robert F Sekerka. Computation of the dendritic operating state at large supercoolings by the phase field model. *Physical Review E*, 53(4):3760, 1996.

[270] Christoph Beckermann, H-J Diepers, Ingo Steinbach, Alain Karma, and Xinglin Tong. Modeling melt convection in phase-field simulations of solidification. *Journal of Computational Physics*, 154(2):468–496, 1999.

[271] XQ Ma, SQ Shi, CH Woo, and LQ Chen. The phase field model for hydrogen diffusion and γ-hydride precipitation in zirconium under non-uniformly applied stress. *Mechanics of Materials*, 38(1-2):3–10, 2006.

[272] Z-W Lai. Theory of ordering dynamics for cu 3 au. *Physical Review B*, 41(13):9239, 1990.

[273] G Rubin and AG Khachaturyan. Three-dimensional model of precipitation of ordered intermetallics. *Acta materialia*, 47(7):1995–2002, 1999.

[274] Wanida Pongsaksawad, Adam C Powell, and David Dussault. Phase-field modeling of transport-limited electrolysis in solid and liquid states. *Journal of The Electrochemical Society*, 154(6):F122–F133, 2007.

[275] Tomohiro Takaki. A phase-field topology optimization model using a double-obstacle function. In *ECCOMAS 2012-European congress on computational methods in applied sciences and engineering, e-Book Full Papers*, pages 8761–8768, 2012.

[276] Perry H Leo and WC Johnson. Spinodal decomposition and coarsening of stressed thin films on compliant substrates. *Acta materialia*, 49(10):1771–1787, 2001.

[277] Jing Xu, Xianzhi Wang, and Binbin Wang. Biochemical process of ureolysis-based microbial caco 3 precipitation and its application in self-healing concrete. *Applied microbiology and biotechnology*, 102(7):3121–3132, 2018.

[278] Kunamineni Vijay, Meena Murmu, and Shirish V Deo. Bacteria based self healing concrete–a review. *Construction and Building Materials*, 152:1008–1014, 2017.

[279] Md Shahriar Quayum, Xiaoying Zhuang, and Timon Rabczuk. Computational model generation and rve design of self-healing concrete. *Frontiers of Structural and Civil Engineering*, 9(4):383–396, 2015.

[280] Alfons Mersmann, Martin Angerhöfer, and Jürgen Franke. Controlled precipitation. *Chemical Engineering & Technology: Industrial Chemistry-Plant Equipment-Process Engineering-Biotechnology*, 17(1):1–9, 1994.

[281] Blas Echebarria, Roger Folch, Alain Karma, and Mathis Plapp. Quantitative phase-field model of alloy solidification. *Physical review E*, 70(6):061604, 2004.

[282] Alain Karma, David A Kessler, and Herbert Levine. Phase-field model of mode iii dynamic fracture. *Physical Review Letters*, 87(4):045501, 2001.

[283] Alain Karma and Wouter-Jan Rappel. Numerical simulation of three-dimensional dendritic growth. *Physical Review Letters*, 77(19):4050, 1996.

[284] James A Warren, Ryo Kobayashi, Alexander E Lobkovsky, and W Craig Carter. Extending phase field models of solidification to polycrystalline materials. *Acta Materialia*, 51(20):6035–6058, 2003.

[285] Qing Chen, Ning Ma, Kaisheng Wu, and Yunzhi Wang. Quantitative phase field modeling of diffusion-controlled precipitate growth and dissolution in ti–al–v. *Scripta Materialia*, 50(4):471–476, 2004.

[286] Y Wang, L-Q Chen, and AG Khachaturyan. Kinetics of strain-induced morphological transformation in cubic alloys with a miscibility gap. *Acta Metallurgica et Materialia*, 41(1):279–296, 1993.

[287] TL Van Noorden and Christof Eck. Phase field approximation of a kinetic moving-boundary problem modelling dissolution and precipitation. *Interfaces and Free Boundaries*, 13(1):29–55, 2011.

[288] Long-Qing Chen and Wei Yang. Computer simulation of the domain dynamics of a quenched system with a large number of nonconserved order parameters: The grain-growth kinetics. *Physical Review B*, 50(21):15752, 1994.

[289] JZ Zhu, T Wang, AJ Ardell, SH Zhou, ZK Liu, and LQ Chen. Three-dimensional phase-field simulations of coarsening kinetics of r particles in binary ni–al alloys. *Acta materialia*, 52(9):2837–2845, 2004.

[290] John S Lowengrub, Andreas Rätz, and Axel Voigt. Phase-field modeling of the dynamics of multicomponent vesicles: Spinodal decomposition, coarsening, budding, and fission. *Physical Review E*, 79(3):031926, 2009.

[291] SY Hu and LQ Chen. Solute segregation and coherent nucleation and growth near a dislocation—a phase-field model integrating defect and phase microstructures. *Acta materialia*, 49(3):463–472, 2001.

[292] D Rodney, Y Le Bouar, and A Finel. Phase field methods and dislocations. *Acta materialia*, 51(1):17–30, 2003.

[293] Klaus Kassner, Chaouqi Misbah, Judith Müller, Jens Kappey, and Peter Kohlert. Phase-field modeling of stress-induced instabilities. *Physical Review E*, 63(3):036117, 2001.

[294] K Kassner and C Misbah. A phase-field approach for stress-induced instabilities. *EPL (Europhysics Letters)*, 46(2):217, 1999.

[295] Qiang Du, Chun Liu, and Xiaoqiang Wang. Simulating the deformation of vesicle membranes under elastic bending energy in three dimensions. *Journal of Computational Physics*, 212(2):757–777, 2006.

[296] Thierry Biben, Klaus Kassner, and Chaouqi Misbah. Phase-field approach to three-dimensional vesicle dynamics. *Physical Review E*, 72(4):041921, 2005.

[297] François Léonard and Rashmi C Desai. Alloy decomposition and surface instabilities in thin films. *Physical Review B*, 57(8):4805, 1998.

[298] You-Hai Wen, Long-Qing Chen, and Jeffrey A Hawk. Phase-field modeling of corrosion kinetics under dual-oxidants. *Modelling and Simulation in Materials Science and Engineering*, 20(3):035013, 2012.

[299] Yasushi Shibuta, Yoshinao Okajima, and Toshio Suzuki. A phase-field simulation of bridge formation process in a nanometer-scale switch. *Scripta materialia*, 55(12):1095–1098, 2006.

[300] Yasushi Shibuta, Yoshinao Okajima, and Toshio Suzuki. Phase-field modeling for electrodeposition process. *Science and Technology of Advanced Materials*, 8(6):511, 2007.

[301] Jonathan E Guyer, William J Boettinger, James A Warren, and Geoffrey B McFadden. Phase field modeling of electrochemistry. i. equilibrium. *Physical Review E*, 69(2):021603, 2004.

[302] Abhik Choudhury and Britta Nestler. Grand-potential formulation for multicomponent phase transformations combined with thin-interface asymptotics of the double-obstacle potential. *Physical Review E*, 85(2):021602, 2012.

[303] B Böttger, J Eiken, and I Steinbach. Phase field simulation of equiaxed solidification in technical alloys. *Acta materialia*, 54(10):2697–2704, 2006.

[304] Yoshitsugu Oono and Sanjay Puri. Study of phase-separation dynamics by use of cell dynamical systems. i. modeling. *Physical Review A*, 38(1):434, 1988.

[305] JF Blowey and CM Elliott. A phase-field model with double obstacle potential,"motions by mean curvature and related topics", g. buttazzo and a. visintin eds, 1994.

[306] Deepali N Bhate, Ashish Kumar, and Allan F Bower. Diffuse interface model for electromigration and stress voiding. *Journal of Applied Physics*, 87(4):1712–1721, 2000.

[307] John W Barrett, Harald Garcke, and Robert Nürnberg. A phase field model for the electromigration of intergranular voids. *Interfaces and Free Boundaries*, 9(2):171–210, 2007.

[308] YU Wang, YM Jin, AM Cuitino, and AG Khachaturyan. Phase field microelasticity theory and modeling of multiple dislocation dynamics. *Applied Physics Letters*, 78(16):2324–2326, 2001.

[309] Yu U Wang, YM Jin, AM Cuitino, and AG Khachaturyan. Nanoscale phase field microelasticity theory of dislocations: model and 3d simulations. *Acta Materialia*, 49(10):1847–1857, 2001.

[310] Alain Karma and Mathis Plapp. Spiral surface growth without desorption. *Physical Review Letters*, 81(20):4444, 1998.

[311] RJ Braun, JW Cahn, GB McFadden, HE Rushmeier, and AA Wheeler. Theory of anisotropic growth rates in the ordering of an fcc alloy. *Acta materialia*, 46(1):1–12, 1998.

[312] Y Wang, D Banerjee, CC Su, and AG Khachaturyan. Field kinetic model and computer simulation of precipitation of l12 ordered intermetallics from fcc solid solution. *Acta materialia*, 46(9):2983–3001, 1998.

[313] Ryo Kobayashi. Modeling and numerical simulations of dendritic crystal growth. *Physica D: Nonlinear Phenomena*, 63(3-4):410–423, 1993.

[314] S-L Wang, RF Sekerka, AA Wheeler, BT Murray, SR Coriell, RJea Braun, and GB McFadden. Thermodynamically-consistent phase-field models for solidification. *Physica D: Nonlinear Phenomena*, 69(1-2):189–200, 1993.

[315] Yu U Wang. Computer modeling and simulation of solid-state sintering: A phase field approach. *Acta materialia*, 54(4):953–961, 2006.

[316] Y Wang and AG Khachaturyan. Three-dimensional field model and computer modeling of martensitic transformations. *Acta materialia*, 45(2):759–773, 1997.

[317] I Münch and M Krauß. An enhanced finite element technique for diffuse phase transition. *Computational Mechanics*, 56(4):691–708, 2015.

[318] Hamid Assadi. Phase-field modelling of electro-deoxidation in molten salt. *Modelling and Simulation in Materials Science and Engineering*, 14(6):963, 2006.

[319] YL Li, SY Hu, ZK Liu, and LQ Chen. Effect of substrate constraint on the stability and evolution of ferroelectric domain structures in thin films. *Acta materialia*, 50(2):395–411, 2002.

[320] YL Li and LQ Chen. Temperature-strain phase diagram for ba ti o 3 thin films. *Applied physics letters*, 88(7):072905, 2006.

[321] Luthfi Muhammad Mauludin and Chahmi Oucif. Modeling of self-healing concrete: A review. *Journal of Applied and Computational Mechanics*, 5(Special Issue: Computational Methods for Material Failure):526–539, 2019.

[322] Zhijie Xu, Hai Huang, Xiaoyi Li, and Paul Meakin. Phase field and level set methods for modeling solute precipitation and/or dissolution. *Computer Physics Communications*, 183(1):15–19, 2012.

[323] Magnus Redeker, Christian Rohde, and Iuliu Sorin Pop. Upscaling of a tri-phase phase-field model for precipitation in porous media. *IMA Journal of Applied Mathematics*, 81(5):898–939, 2016.

[324] Christian Rohde and Lars von Wolff. A ternary cahn-hilliard navier-stokes model for two phase flow with precipitation and dissolution. *arXiv preprint arXiv:1912.09181*, 2019.

[325] Carina Bringedal, Lars von Wolff, and Iuliu Sorin Pop. Phase field modeling of precipitation and dissolution processes in porous media: Upscaling and numerical experiments. *Multiscale Modeling & Simulation*, 18(2):1076–1112, 2020.

[326] Christian Schwarze, Ankit Gupta, Tilmann Hickel, and R Darvishi Kamachali. Phase-field study of ripening and rearrangement of precipitates under chemomechanical coupling. *Physical Review B*, 95(17):174101, 2017.

[327] S Müller, C Wolverton, L-W Wang, and A Zunger. Predicting the size-and temperature-dependent shapes of precipitates in al–zn alloys. *Acta materialia*, 48(16):4007–4020, 2000.

[328] Rongpei Shi and Yunzhi Wang. Variant selection during α precipitation in ti–6al–4v under the influence of local stress–a simulation study. *Acta materialia*, 61(16):6006–6024, 2013.

[329] Martin Silberberg. *Principles of general chemistry*. McGraw-Hill Education, 2012.

[330] HOBART H Willard. Separation by precipitation from homogeneous solution. *Analytical Chemistry*, 22(11):1372–1374, 1950.

[331] PFS Cartwright, EJ Newman, and DW Wilson. Precipitation from homogeneous solution. a review. *Analyst*, 92(1100):663–679, 1967.

[332] Edward Collings. *Physics of solid solution strengthening*. Springer Science & Business Media, 2012.

[333] Ilya M Lifshitz and Vitaly V Slyozov. The kinetics of precipitation from supersaturated solid solutions. *Journal of physics and chemistry of solids*, 19(1-2):35–50, 1961.

[334] Iqra Zubair Awan and Abdul Qadeer Khan. Precipitation from solid solutions. *Journal of the Chemical Society of Pakistan*, 39(3), 2017.

[335] William D Callister et al. *Fundamentals of materials science and engineering*, volume 471660817. Wiley London, 2000.

[336] Hua Hou, Yuhong Zhao, and Yuhui Zhao. Simulation of the precipitation process of ordered intermetallic compounds in binary and ternary ni–al-based alloys by the phase-field model. *Materials Science and Engineering: A*, 499(1-2):204–207, 2009.

[337] YH Wen, JV Lill, SL Chen, and JP Simmons. A ternary phase-field model incorporating commercial calphad software and its application to precipitation in superalloys. *Acta materialia*, 58(3):875–885, 2010.

[338] FH Wittmann. Structure of concrete with respect to crack formation. *Fracture mechanics of concrete*, 43(5):6, 1983.

[339] Jacky Mazars and Gilles Pijaudier-Cabot. Continuum damage theory—application to concrete. *Journal of engineering mechanics*, 115(2):345–365, 1989.

[340] E Schlangen and JGM Van Mier. Micromechanical analysis of fracture of concrete. *International Journal of Damage Mechanics*, 1(4):435–454, 1992.

[341] Jean Lemaitre and Jean-Louis Chaboche. *Mechanics of solid materials*. Cambridge university press, 1994.

[342] Günther Meschke, Roman Lackner, and Herbert A Mang. An anisotropic elastoplastic-damage model for plain concrete. *International journal for numerical methods in engineering*, 42(4):703–727, 1998.

[343] Peter Wriggers and SO Moftah. Mesoscale models for concrete: Homogenisation and damage behaviour. *Finite elements in analysis and design*, 42(7):623–636, 2006.

[344] Meinhard Kuna. *Numerische Beanspruchungsanalyse von Rissen*, volume 2. Springer, 2008.

[345] Konstantin Sobolev and SP Shah. *Nanotechnology of concrete: recent developments and future perspectives*. ACI, 2008.

[346] RR Pedersen, A Simone, and LJ Sluys. An analysis of dynamic fracture in concrete with a continuum visco-elastic visco-plastic damage model. *Engineering fracture mechanics*, 75(13):3782–3805, 2008.

[347] M Hain and P Wriggers. Numerical homogenization of hardened cement paste. *Computational Mechanics*, 42(2):197–212, 2008.

[348] Sun-Myung Kim and Rashid K Abu Al-Rub. Meso-scale computational modeling of the plastic-damage response of cementitious composites. *Cement and Concrete Research*, 41(3):339–358, 2011.

[349] Jörg F Unger, Stefan Eckardt, and C Kooenke. A mesoscale model for concrete to simulate mechanical failure. *Computers & Concrete*, 8(4):401–423, 2011.

[350] Ludger Lohaus, Nadja Oneschkow, and Maik Wefer. Design model for the fatigue behaviour of normal-strength, high-strength and ultra-high-strength concrete. *Structural Concrete*, 13(3):182–192, 2012.

[351] Ted L Anderson. *Fracture mechanics: fundamentals and applications*. CRC press, 2017.

[352] Imadeddin Zreid and Michael Kaliske. A gradient enhanced plasticity–damage microplane model for concrete. *Computational Mechanics*, 62(5):1239–1257, 2018.

[353] Niklas Schäfer, Vladislav Gudžulić, Jithender J Timothy, Rolf Breitenbücher, and Günther Meschke. Fatigue behavior of hpc and frc under cyclic tensile loading: Experiments and modeling. *Structural Concrete*, 20(4):1265–1278, 2019.

[354] Gregor Gebuhr, Mangesh Pise, Mohammad Sarhil, Steffen Anders, Dominik Brands, and Jörg Schröder. Analysis and evaluation of the pull-out behavior of hooked steel fibers embedded in high and ultra-high performance concrete for calibration of numerical models. *Structural Concrete*, 20:1254–1264, 06 2019.

[355] Nicolas Moës and Ted Belytschko. Extended finite element method for cohesive crack growth. *Engineering fracture mechanics*, 69(7):813–833, 2002.

[356] S Loehnert, DS Mueller-Hoeppe, and P Wriggers. 3d corrected xfem approach and extension to finite deformation theory. *International Journal for Numerical Methods in Engineering*, 86(4-5):431–452, 2011.

[357] Blaise Bourdin, Gilles A Francfort, and Jean-Jacques Marigo. The variational approach to fracture. *Journal of elasticity*, 91(1-3):5–148, 2008.

[358] Charlotte Kuhn and Ralf Müller. A continuum phase field model for fracture. *Engineering Fracture Mechanics*, 77(18):3625–3634, 2010.

[359] Michael J Borden, Clemens V Verhoosel, Michael A Scott, Thomas JR Hughes, and Chad M Landis. A phase-field description of dynamic brittle fracture. *Computer Methods in Applied Mechanics and Engineering*, 217:77–95, 2012.

[360] Christian Hesch and Kerstin Weinberg. Thermodynamically consistent algorithms for a finite-deformation phase-field approach to fracture. *International Journal for Numerical Methods in Engineering*, 99(12):906–924, 2014.

[361] Christian Miehe, Lisa-Marie Schaenzel, and Heike Ulmer. Phase field modeling of fracture in multi-physics problems. part i. balance of crack surface and failure criteria for brittle crack propagation in thermo-elastic solids. *Computer Methods in Applied Mechanics and Engineering*, 294:449–485, 2015.

[362] Timo Heister, Mary F Wheeler, and Thomas Wick. A primal-dual active set method and predictor-corrector mesh adaptivity for computing fracture propagation using a phase-field approach. *Computer Methods in Applied Mechanics and Engineering*, 290:466–495, 2015.

[363] Y Heider and B Markert. A phase-field modeling approach of hydraulic fracture in saturated porous media. *Mechanics Research Communications*, 80:38–46, 2017.

[364] Marco Paggi and José Reinoso. Revisiting the problem of a crack impinging on an interface: a modeling framework for the interaction between the phase field approach for brittle fracture and the interface cohesive zone model. *Computer Methods in Applied Mechanics and Engineering*, 321:145–172, 2017.

[365] Udit Pillai, Yousef Heider, and Bernd Markert. A diffusive dynamic brittle fracture model for heterogeneous solids and porous materials with implementation using a user-element subroutine. *Computational Materials Science*, 153:36–47, 2018.

[366] Fadi Aldakheel, Blaž Hudobivnik, Ali Hussein, and Peter Wriggers. Phase-field modeling of brittle fracture using an efficient virtual element scheme. *Computer Methods in Applied Mechanics and Engineering*, 341:443–466, 2018.

[367] Karlo Seleš, Ante Jurčević, Zdenko Tonković, and Jurica Sorić. Crack propagation prediction in heterogeneous microstructure using an efficient phase-field algorithm. *Theoretical and Applied Fracture Mechanics*, 100:289–297, 2019.

[368] Nima Noii, Fadi Aldakheel, Thomas Wick, and Peter Wriggers. An adaptive global–local approach for phase-field modeling of anisotropic brittle fracture. *Computer Methods in Applied Mechanics and Engineering*, 361:112744, 2020.

[369] Yousef Heider and WaiChing Sun. A phase field framework for capillary-induced fracture in unsaturated porous media: Drying-induced vs. hydraulic cracking. *Computer Methods in Applied Mechanics and Engineering*, 359:112647, 2020.

[370] Fadi Aldakheel, Christoph Tomann, Ludger Lohaus, and Peter Wriggers. Water-induced failure mechanics for concrete. *PAMM*, 19(1):e201900140, 2019.

[371] Christian Miehe, HÜSNÜ Dal, L-M Schänzel, and A Raina. A phase-field model for chemo-mechanical induced fracture in lithium-ion battery electrode particles. *International Journal for Numerical Methods in Engineering*, 106(9):683–711, 2016.

[372] Marreddy Ambati, Tymofiy Gerasimov, and Laura De Lorenzis. A review on phase-field models of brittle fracture and a new fast hybrid formulation. *Computational Mechanics*, 55(2):383–405, 2015.

[373] C Tomann, L Lohaus, F Aldakheel, and P Wriggers. Influence of water-induced damage mechanisms on the fatigue deterioration of high-strength concrete. In *Proceedings of 6th International fib Congress: Concrete–innovations in materials, design and structures*, 2019.

[374] Valerio Carollo, Marco Paggi, and José Reinoso. The steady-state archard adhesive wear problem revisited based on the phase field approach to fracture. *International Journal of Fracture*, 215(1-2):39–48, 2019.

[375] Christian Steinke and Michael Kaliske. A phase-field crack model based on directional stress decomposition. *Computational Mechanics*, 63(5):1019–1046, 2019.

[376] P Carrara, M Ambati, R Alessi, and L De Lorenzis. A framework to model the fatigue behavior of brittle materials based on a variational phase-field approach. *Computer Methods in Applied Mechanics and Engineering*, 361:112731, 2020.

[377] Yousef Heider, Sönke Reiche, Philipp Siebert, and Bernd Markert. Modeling of hydraulic fracturing using a porous-media phase-field approach with reference to experimental data. *Engineering Fracture Mechanics*, 202:116–134, 2018.

[378] Francesca Fantoni, Andrea Bacigalupo, Marco Paggi, and Josè Reinoso. A phase field approach for damage propagation in periodic microstructured materials. *International Journal of Fracture*, pages 1–24, 2019.

[379] Fadi Aldakheel, Nima Noii, Thomas Wick, and Peter Wriggers. A global-local approach for hydraulic phase-field fracture in poroelastic media. *Computers & Mathematics with Applications*, 2020. https://doi.org/10.1016/j.camwa.2020.07.013.

[380] Bo Yin and Michael Kaliske. An anisotropic phase-field model based on the equivalent crack surface energy density at finite strain. *Computer Methods in Applied Mechanics and Engineering*, 369:113202, 2020.

[381] Amirreza Khodadadian, Nima Noii, Maryam Parvizi, Mostafa Abbaszadeh, Thomas Wick, and Clemens Heitzinger. A bayesian estimation method for variational phase-field fracture problems. *Computational Mechanics*, pages 1–23, 2020.

[382] S Teichtmeister, D Kienle, F Aldakheel, and M-A Keip. Phase field modeling of fracture in anisotropic brittle solids. *International Journal of Non-Linear Mechanics*, 97:1–21, 2017.

[383] Carola Bilgen, Stefanie Homberger, and Kerstin Weinberg. Phase-field fracture simulations of the brazilian splitting test. *International Journal of Fracture*, 220(1):85–98, 2019.

[384] Resam Makvandi, Sascha Duczek, and Daniel Juhre. A phase-field fracture model based on strain gradient elasticity. *Engineering Fracture Mechanics*, 220:106648, 2019.

[385] P Wriggers, F Aldakheel, L Lohaus, and M Heist. Water-induced damage mechanisms of cyclically loaded high-performance concretes. *Bauingenieur*, 95(4):126–132, 2020.

[386] Funda Aksu Denli, Osman Gültekin, Gerhard A Holzapfel, and Hüsnü Dal. A phase-field model for fracture of unidirectional fiber-reinforced polymer matrix composites. *Computational Mechanics*, pages 1–18, 2020.

[387] Christoph Schreiber, Charlotte Kuhn, Ralf Müller, and Tarek Zohdi. A phase field modeling approach of cyclic fatigue crack growth. *International Journal of Fracture*, 225(1):89–100, 2020.

[388] Xiaoying Zhuang, Shuwei Zhou, Mao Sheng, and Gengsheng Li. On the hydraulic fracturing in naturally-layered porous media using the phase field method. *Engineering Geology*, 266:105306, 2020.

[389] M Dittmann, M Krüger, F Schmidt, S Schuß, and C Hesch. Variational modeling of thermomechanical fracture and anisotropic frictional mortar contact problems with adhesion. *Computational Mechanics*, 63(3):571–591, 2019.

[390] A Hussein, P Wriggers, B Hudobivnik, F Aldakheel, P-A Guidault, and O Allix. Treatment of brittle fracture in solids with the virtual element method. In *Virtual Design and Validation*, pages 201–228. Springer, 2020.

[391] Thomas Wick. *Multiphysics Phase-Field Fracture: Modeling, Adaptive Discretizations, and Solvers*, volume 28. Walter de Gruyter GmbH & Co KG, 2020.

[392] Rudy Geelen, Julia Plews, Michael Tupek, and John Dolbow. An extended/generalized phase-field finite element method for crack growth with global-local enrichment. *International Journal for Numerical Methods in Engineering*, 121(11):2534–2557, 2020.

[393] Ran Ma and WaiChing Sun. Fft-based solver for higher-order and multi-phase-field fracture models applied to strongly anisotropic brittle materials. *Computer Methods in Applied Mechanics and Engineering*, 362:112781, 2020.

[394] Preetam Tarafder, Saikat Dan, and Somnath Ghosh. Finite deformation cohesive zone phase field model for crack propagation in multi-phase microstructures. *Computational Mechanics*, 66(3):723–743, 2020.

[395] Laura De Lorenzis and Tymofiy Gerasimov. Numerical implementation of phase-field models of brittle fracture. In *Modeling in Engineering Using Innovative Numerical Methods for Solids and Fluids*, pages 75–101. Springer, 2020.

[396] Christian Miehe, M Hofacker, L-M Schänzel, and Fadi Aldakheel. Phase field modeling of fracture in multi-physics problems. part ii. coupled brittle-to-ductile failure criteria and crack propagation in thermo-elastic–plastic solids. *Computer Methods in Applied Mechanics and Engineering*, 294:486–522, 2015.

[397] Pengfei Li, Julien Yvonnet, and Christelle Combescure. An extension of the phase field method to model interactions between interfacial damage and brittle fracture in elastoplastic composites. *International Journal of Mechanical Sciences*, page 105633, 2020.

[398] Marreddy Ambati, Roland Kruse, and Laura De Lorenzis. A phase-field model for ductile fracture at finite strains and its experimental verification. *Computational Mechanics*, 57(1):149–167, 2016.

[399] Oliver Barfusz, Tim Brepols, Tim van der Velden, Jan Frischkorn, and Stefanie Reese. A single gauss point continuum finite element formulation for gradient-extended damage at large deformations. *Computer Methods in Applied Mechanics and Engineering*, 373:113440.

[400] Martin Diehl, Marcel Wicke, Pratheek Shanthraj, Franz Roters, Angelika Brueckner-Foit, and Dierk Raabe. Coupled crystal plasticity–phase field fracture simulation study on damage evolution around a void: pore shape versus crystallographic orientation. *Jom*, 69(5):872–878, 2017.

[401] Christian Miehe, Fadi Aldakheel, and Stephan Teichtmeister. Phase-field modeling of ductile fracture at finite strains: A robust variational-based numerical implementation of a gradient-extended theory by micromorphic regularization. *International Journal for Numerical Methods in Engineering*, 111(9):816–863, 2017.

[402] Michael J Borden, Thomas JR Hughes, Chad M Landis, Amin Anvari, and Isaac J Lee. A phase-field formulation for fracture in ductile materials: Finite deformation balance law derivation, plastic degradation, and stress triaxiality effects. *Computer Methods in Applied Mechanics and Engineering*, 312:130–166, 2016.

[403] Christian Miehe, Fadi Aldakheel, and Arun Raina. Phase field modeling of ductile fracture at finite strains: A variational gradient-extended plasticity-damage theory. *International Journal of Plasticity*, 84:1–32, 2016.

[404] Roberto Alessi, Jean-Jacques Marigo, Corrado Maurini, and Stefano Vidoli. Coupling damage and plasticity for a phase-field regularisation of brittle, cohesive and ductile fracture: one-dimensional examples. *International Journal of Mechanical Sciences*, 149:559–576, 2018.

[405] Fadi Aldakheel, Steffen Mauthe, and Christian Miehe. Towards phase field modeling of ductile fracture in gradient-extended elastic-plastic solids. *PAMM*, 14(1):411–412, 2014.

[406] Hojjat Badnava, Elahe Etemadi, and Mohammed A Msekh. A phase field model for rate-dependent ductile fracture. *Metals*, 7(5):180, 2017.

[407] M Dittmann, F Aldakheel, J Schulte, F Schmidt, M Krüger, P Wriggers, and C Hesch. Phase-field modeling of porous-ductile fracture in non-linear thermo-elasto-plastic solids. *Computer Methods in Applied Mechanics and Engineering*, 361:112730, 2020.

[408] Jinhyun Choo and WaiChing Sun. Coupled phase-field and plasticity modeling of geological materials: From brittle fracture to ductile flow. *Computer Methods in Applied Mechanics and Engineering*, 330:1–32, 2018.

[409] Martha Seiler, Thomas Linse, Peter Hantschke, and Markus Kästner. An efficient phase-field model for fatigue fracture in ductile materials. *Engineering Fracture Mechanics*, 224:106807, 2020.

[410] M Dittmann, F Aldakheel, J Schulte, P Wriggers, and C Hesch. Variational phase-field formulation of non-linear ductile fracture. *Computer Methods in Applied Mechanics and Engineering*, 342:71–94, 2018.

[411] Bo Yin and Michael Kaliske. A ductile phase-field model based on degrading the fracture toughness: Theory and implementation at small strain. *Computer Methods in Applied Mechanics and Engineering*, 366:113068, 2020.

[412] Fadi Aldakheel, Blaž Hudobivnik, and Peter Wriggers. Virtual element formulation for phase-field modeling of ductile fracture. *International Journal for Multiscale Computational Engineering*, 17(2), 2019.

[413] Charlotte Kuhn, Timo Noll, and Ralf Müller. On phase field modeling of ductile fracture. *GAMM-Mitteilungen*, 39(1):35–54, 2016.

[414] Christian Miehe, Daniel Kienle, Fadi Aldakheel, and Stephan Teichtmeister. Phase field modeling of fracture in porous plasticity: A variational gradient-extended eulerian framework for the macroscopic analysis of ductile failure. *Computer Methods in Applied Mechanics and Engineering*, 312:3–50, 2016.

[415] Jianguang Fang, Chengqing Wu, Jun Li, Qiang Liu, Chi Wu, Guangyong Sun, and Qing Li. Phase field fracture in elasto-plastic solids: Variational formulation for multi-surface plasticity and effects of plastic yield surfaces and hardening. *International Journal of Mechanical Sciences*, 156:382–396, 2019.

[416] M Krüger, M Dittmann, F Aldakheel, A Härtel, P Wriggers, and C Hesch. Porous-ductile fracture in thermo-elasto-plastic solids with contact applications. *Computational Mechanics*, pages 1–26, 2019. https://doi.org/10.1007/s00466-019-01802-3.

[417] Lam H Nguyen and Dominik Schillinger. The multiscale finite element method for nonlinear continuum localization problems at full fine-scale fidelity, illustrated through phase-field fracture and plasticity. *Journal of Computational Physics*, 396:129–160, 2019.

[418] Erfan Azinpour, Jose Cesar de Sa, and Abel Dias dos Santos. Micromechanically-motivated phase field approach to ductile fracture. *International Journal of Damage Mechanics*, page 1056789520948933, 2020.

[419] Fadi Aldakheel, Peter Wriggers, and Christian Miehe. A modified gurson-type plasticity model at finite strains: formulation, numerical analysis and phase-field coupling. *Computational Mechanics*, 62(4):815–833, 2018.

[420] Tim Brepols, Stephan Wulfinghoff, and Stefanie Reese. A gradient-extended two-surface damage-plasticity model for large deformations. *International Journal of Plasticity*, 129:102635, 2020.

[421] A Dean, J Reinoso, NK Jha, E Mahdi, and R Rolfes. A phase field approach for ductile fracture of short fibre reinforced composites. *Theoretical and Applied Fracture Mechanics*, page 102495, 2020. https://doi.org/10.1016/j.tafmec.2020.102495.

[422] Daniel Kienle, Fadi Aldakheel, and Marc-André Keip. A finite-strain phase-field approach to ductile failure of frictional materials. *International Journal of Solids and Structures*, 172:147–162, 2019.

[423] Waseem Amin, Muhammad Adil Ali, Napat Vajragupta, and Alexander Hartmaier. Studying grain boundary strengthening by dislocation-based strain gradient crystal plasticity coupled with a multi-phase-field model. *Materials*, 12(18):2977, 2019.

[424] Elber Wolf. Fatigue crack closure under cyclic tension. *Engineering fracture mechanics*, 2(1):37–45, 1970.

[425] Wolf Elber. The significance of fatigue crack closure. In *Damage tolerance in aircraft structures*. ASTM International, 1971.

[426] AK Vasudeven, K Sadananda, and N Louat. A review of crack closure, fatigue crack threshold and related phenomena. *Materials Science and Engineering: A*, 188(1-2):1–22, 1994.

[427] Ronald Krueger. Virtual crack closure technique: history, approach, and applications. *Appl. Mech. Rev.*, 57(2):109–143, 2004.

[428] Reinhard Pippan and Anton Hohenwarter. Fatigue crack closure: a review of the physical phenomena. *Fatigue & fracture of engineering materials & structures*, 40(4):471–495, 2017.

[429] Fadi Aldakheel, Blaz Hudobivnik, Edoardo Artioli, L Beirao da Veiga, and Peter Wriggers. Curvilinear virtual elements for contact mechanics. *Accepted in Computer Methods in Applied Mechanics and Engineering*, 2020.

[430] Gilles A Francfort and J-J Marigo. Revisiting brittle fracture as an energy minimization problem. *Journal of the Mechanics and Physics of Solids*, 46(8):1319–1342, 1998.

[431] David Bryant Mumford and Jayant Shah. Optimal approximations by piecewise smooth functions and associated variational problems. *Communications on pure and applied mathematics*, 1989.

[432] Erich J Weissbart and J Donald Rimstidt. Wollastonite: Incongruent dissolution and leached layer formation. *Geochimica et Cosmochimica Acta*, 64(23):4007–4016, 2000.

[433] Marie-Claude Bluteau and George P Demopoulos. The incongruent dissolution of scorodite—solubility, kinetics and mechanism. *Hydrometallurgy*, 87(3-4):163–177, 2007.

[434] Howard B Aaron, Dora Fainstein, and Gerald R Kotler. Diffusion-limited phase transformations: a comparison and critical evaluation of the mathematical approximations. *Journal of applied physics*, 41(11):4404–4410, 1970.

[435] Bernhard Wehrli. Monte carlo simulations of surface morphologies during mineral dissolution. *Journal of Colloid and Interface Science*, 132(1):230–242, 1989.

[436] Xin Yang, Xinrong Liu, Junbao Wang, Zhenwei Zhao, and Hujun Lei. Analytical solution of a mathematical model for rock salt dissolution in still water. *Arabian Journal of Geosciences*, 11(23):1–10, 2018.

[437] Boris Shekunov and Eda Ross Montgomery. Theoretical analysis of drug dissolution: I. solubility and intrinsic dissolution rate. *Journal of pharmaceutical sciences*, 105(9):2685–2697, 2016.

[438] J Siepmann and F Siepmann. Mathematical modeling of drug dissolution. *International journal of pharmaceutics*, 453(1):12–24, 2013.

[439] Yanxing Wang, Bertil Abrahamsson, Lennart Lindfors, and James G Brasseur. Comparison and analysis of theoretical models for diffusion-controlled dissolution. *Molecular pharmaceutics*, 9(5):1052–1066, 2012.

[440] Xiaoling Guo, Jilt Sietsma, Yongxiang Yang, Zhi Sun, and Muxing Guo. Diffusion-limited dissolution of spherical particles: A critical evaluation and applications of approximate solutions. *AIChE Journal*, 63(7):2926–2934, 2017.

[441] D Samaha, R Shehayeb, and S Kyriacos. Modeling and comparison of dissolution profiles of diltiazem modified-release formulations. *Dissolution Technol*, 16(2):41–6, 2009.

[442] Jianzhuo Wang and Douglas R Flanagan. General solution for diffusion-controlled dissolution of spherical particles. 2. evaluation of experimental data. *Journal of pharmaceutical sciences*, 91(2):534–542, 2002.

[443] Hitoshi Matsubara and Tomonori Yamada. Mathematical and numerical modelling of limestone dissolution. *Environmental Geotechnics*, 40(XXXX):1–12, 2019.

[444] Luc Nicoleau and Maria Alice Bertolim. Analytical model for the alite (c3s) dissolution topography. *Journal of the American Ceramic Society*, 99(3):773–786, 2016.

[445] Shinji Nambu and Djuniadi A Sagala. Domain formation and elastic long-range interaction in ferroelectric perovskites. *Physical Review B*, 50(9):5838, 1994.

[446] Seong Gyoon Kim, Dong Ik Kim, Won Tae Kim, and Yong Bum Park. Computer simulations of two-dimensional and three-dimensional ideal grain growth. *Physical Review E*, 74(6):061605, 2006.

[447] Ryo Kobayashi, James A Warren, and W Craig Carter. Vector-valued phase field model for crystallization and grain boundary formation. *Physica D: Nonlinear Phenomena*, 119(3-4):415–423, 1998.

[448] P-R Cha, D-H Yeon, and J-K Yoon. A phase field model for isothermal solidification of multicomponent alloys. *Acta materialia*, 49(16):3295–3307, 2001.

[449] Toshio Suzuki, Machiko Ode, Seong Gyoon Kim, and Won Tae Kim. Phase-field model of dendritic growth. *Journal of Crystal Growth*, 237:125–131, 2002.

[450] Vittorio E Badalassi, Hector D Ceniceros, and Sanjoy Banerjee. Computation of multiphase systems with phase field models. *Journal of computational physics*, 190(2):371–397, 2003.

[451] Thomas Petersen, Pierre-Louis Valdenaire, Roland Pellenq, and Franz-Josef Ulm. A reaction model for cement solidification: Evolving the c–s–h packing density at the micrometer-scale. *Journal of the Mechanics and Physics of Solids*, 118:58–73, 2018.

[452] Ingo Steinbach, Lijun Zhang, and Mathis Plapp. Phase-field model with finite interface dissipation. *Acta Materialia*, 60(6-7):2689–2701, 2012.

[453] Yoshihiro Tonegawa. Phase field model with a variable chemical potential. *Proceedings. Section A, Mathematics-The Royal Society of Edinburgh*, 132(4):993, 2002.

[454] Lei Chen, Feifei Fan, Liang Hong, James Chen, Yanzhou Z Ji, SL Zhang, T Zhu, and LQ Chen. A phase-field model coupled with large elasto-plastic deformation: application to lithiated silicon electrodes. *Journal of The Electrochemical Society*, 161(11):F3164, 2014.

[455] Chen Lin and Haihui Ruan. Multi-phase-field modeling of localized corrosion involving galvanic pitting and mechano-electrochemical coupling. *Corrosion Science*, 177:108900, 2020.

[456] Mark EJ Newman and Michelle Girvan. Finding and evaluating community structure in networks. *Physical review E*, 69(2):026113, 2004.

[457] Adam A Wheeler, William J Boettinger, and Geoffrey B McFadden. Phase-field model of solute trapping during solidification. *Physical Review E*, 47(3):1893, 1993.

[458] Pil-Ryung Cha, Dong-Hee Yeon, and Jong-Kyu Yoon. Phase-field model for multicomponent alloy solidification. *Journal of crystal growth*, 274(1-2):281–293, 2005.

[459] Abba Abdulhamid Abubakar, Syed Sohail Akhtar, and Abul Fazal M Arif. Phase field modeling of v2o5 hot corrosion kinetics in thermal barrier coatings. *Computational Materials Science*, 99:105–116, 2015.

[460] U Grafe, B Böttger, J Tiaden, and SG Fries. Coupling of multicomponent thermodynamic databases to a phase field model: application to solidification and solid state transformations of superalloys. *Scripta Materialia*, 42(12):1179–1186, 2000.

[461] Talha Qasim Ansari, Zhihua Xiao, Shenyang Hu, Yulan Li, Jing-Li Luo, and San-Qiang Shi. Phase-field model of pitting corrosion kinetics in metallic materials. *npj Computational Materials*, 4(1):1–9, 2018.

[462] Weijie Mai and Soheil Soghrati. A phase field model for simulating the stress corrosion cracking initiated from pits. *Corrosion Science*, 125:87–98, 2017.

[463] Zhihua Xiao, Yafeng Wang, Shenyang Hu, Yulan Li, and San-Qiang Shi. A quantitative phase-field model of gas bubble evolution in uo2. *Computational Materials Science*, 184:109867, 2020.

[464] Ruijie Zhang, Tao Jing, Wanqi Jie, and Baicheng Liu. Phase-field simulation of solidification in multicomponent alloys coupled with thermodynamic and diffusion mobility databases. *Acta materialia*, 54(8):2235–2239, 2006.

[465] Hiroki Kobayashi, Machiko Ode, Seong Gyoon Kim, Won Tae Kim, and Toshio Suzuki. Phase-field model for solidification of ternary alloys coupled with thermodynamic database. *Scripta materialia*, 48(6):689–694, 2003.

[466] JB Clark, JW Hastie, LHE Kihlborg, R Metselaar, and MM Thackeray. Definitions of terms relating to phase transitions of the solid state. *Int. Pure Appl. Chem*, 66:577–594, 1994.

[467] Max R McGillen and Ian J Fairchild. An experimental study of incongruent dissolution of caco3 under analogue glacial conditions. *Journal of Glaciology*, 51(174):383–390, 2005.

[468] B Simon. Dissolution rates of nacl and kcl in aqueous solution. *Journal of Crystal Growth*, 52:789–794, 1981.

[469] Angelo Antignano and Craig E Manning. Rutile solubility in h2o, h2o–sio2, and h2o–naalsi3o8 fluids at 0.7–2.0 gpa and 700–1000 c: implications for mobility of nominally insoluble elements. *Chemical Geology*, 255(1-2):283–293, 2008.

[470] Zhixin Xie and John V Walther. Incongruent dissolution and surface area of kaolinite. *Geochimica et Cosmochimica Acta*, 56(9):3357–3363, 1992.

[471] Stefan Scheiner and Christian Hellmich. Stable pitting corrosion of stainless steel as diffusion-controlled dissolution process with a sharp moving electrode boundary. *Corrosion science*, 49(2):319–346, 2007.

[472] Chao Yang, Shilei Li, Xitao Wang, Junsheng Wang, and Houbing Huang. Phase-field simulation of multi-phase interactions in fe-c peritectic solidification. *Computational Materials Science*, 171:109220, 2020.

[473] Seong Gyoon Kim, Won Tae Kim, Toshio Suzuki, and Machiko Ode. Phase-field modeling of eutectic solidification. *Journal of crystal growth*, 261(1):135–158, 2004.

[474] Yanxing Wang, Bertil Abrahamsson, Lennart Lindfors, and James G Brasseur. Analysis of diffusion-controlled dissolution from polydisperse collections of drug particles with an assessed mathematical model. *Journal of pharmaceutical sciences*, 104(9):2998–3017, 2015.

[475] Helen M Burt and AG Mitchell. Crystal defects and dissolution. *International Journal of Pharmaceutics*, 9(2):137–152, 1981.

[476] JUN Wang, Tim C Keener, Guang Li, and SOON-JAI KHANG. The dissolution rate of ca (oh) 2 in aqueous solutions. *Chemical Engineering Communications*, 169(1):167–184, 1998.

[477] David A Vermilyea. The dissolution of mgo and mg (oh) 2 in aqueous solutions. *Journal of the Electrochemical Society*, 116(9):1179, 1969.

[478] K Johannsen and S Rademacher. Modelling the kinetics of calcium hydroxide dissolution in water. *Acta hydrochimica et hydrobiologica*, 27(2):72–78, 1999.

[479] DE Giles, IM Ritchie, and B-A Xu. The kinetics of dissolution of slaked lime. *Hydrometallurgy*, 32(1):119–128, 1993.

[480] Gabriele Lanaro and GN Patey. Molecular dynamics simulation of nacl dissolution. *The Journal of Physical Chemistry B*, 119(11):4275–4283, 2015.

[481] Yong Yang, Sheng Meng, LF Xu, EG Wang, and Shiwu Gao. Dissolution dynamics of nacl nanocrystal in liquid water. *Physical Review E*, 72(1):012602, 2005.

[482] J Garcia, J Hernandez, and J Rubio. Dissolution of in monocrystalline sodium chloride. *Physical Review B*, 21(11), 1980.

[483] H Ohtaki, N Fukushima, Ei Hayakawa, and I Okada. Dissolution process of sodium chloride crystal in water. *Pure and Applied Chemistry*, 60(8):1321–1324, 1988.

[484] Marina Langlet, Frederic Nadaud, Mohammed Benali, Isabelle Pezron, Khashayar Saleh, Pierre Guigon, and Léa Metlas-Komunjer. Kinetics of dissolution and recrystallization of sodium chloride at controlled relative humidity. *KONA Powder and Particle Journal*, 29:168–179, 2011.

[485] Anders Utoft, Koji Kinoshita, Deborah L Bitterfield, and David Needham. Manipulating single microdroplets of nacl solutions: Solvent dissolution, microcrystallization, and crystal morphology. *Langmuir*, 34(12):3626–3641, 2018.

[486] Nico Holmberg, Jian-Cheng Chen, Adam S Foster, and Kari Laasonen. Dissolution of nacl nanocrystals: an ab initio molecular dynamics study. *Physical Chemistry Chemical Physics*, 16(33):17437–17446, 2014.

[487] Yong Yang, Sheng Meng, and EG Wang. A molecular dynamics study of hydration and dissolution of nacl nanocrystal in liquid water. *Journal of Physics: Condensed Matter*, 18(45):10165, 2006.

[488] Hitoshi Ohtaki and Nobuhiro Fukushima. Dissolution of an nacl crystal with the (111) and (-1-1-1) faces. *Pure and Applied Chemistry*, 61(2):179–185, 1989.

[489] Jorge R Espinosa, Carlos Vega, Chantal Valeriani, and Eduardo Sanz. The crystal-fluid interfacial free energy and nucleation rate of nacl from different simulation methods. *The Journal of chemical physics*, 142(19):194709, 2015.

[490] Tomasz Plewa, Timur Linde, V Gregory Weirs, et al. Adaptive mesh refinement-theory and applications. 2005.

[491] Mitra Mosharraf and Christer Nyström. The effect of particle size and shape on the surface specific dissolution rate of microsized practically insoluble drugs. *International journal of pharmaceutics*, 122(1-2):35–47, 1995.

[492] Juan Liu, Deborah M Aruguete, Joerg R Jinschek, J Donald Rimstidt, and Michael F Hochella Jr. The non-oxidative dissolution of galena nanocrystals: Insights into mineral dissolution rates as a function of grain size, shape, and aggregation state. *Geochimica et Cosmochimica Acta*, 72(24):5984–5996, 2008.

[493] WI Higuchi, EL Rowe, and EN Hiestand. Dissolution rates of finely divided drug powders ii: Micronized methylprednisolone. *Journal of pharmaceutical sciences*, 52(2):162–164, 1963.

[494] Luís Pereira De Almeida, Sérgio Simões, Paulo Brito, António Portugal, and Margarida Figueiredo. Modeling dissolution of sparingly soluble multisized powders. *Journal of pharmaceutical sciences*, 86(6):726–732, 1997.

[495] WI Higuchi and EN Hiestand. Dissolution rates of finely divided drug powders i. effect of a distribution of particle sizes in a diffusion-controlled process. *Journal of pharmaceutical sciences*, 52(1):67–71, 1963.

[496] P Kumar Mehta and Richard W Burrows. Building durable structures in the 21st century. *Concrete international*, 23(3):57–63, 2001.

[497] Sheng Wen Tang, Yan Yao, Carmen Andrade, and ZJ Li. Recent durability studies on concrete structure. *Cement and Concrete Research*, 78:143–154, 2015.

[498] Mitsuru Saito, Minoru Ohta, and Hiroshi Ishimori. Chloride permeability of concrete subjected to freeze-thaw damage. *Cement and Concrete Composites*, 16(4):233–239, 1994.

[499] H Hilsdorf and Jörg Kropp. *Performance criteria for concrete durability*. CRC Press, 1995.

[500] Ha-Won Song, Seung-Jun Kwon, Keun-Joo Byun, and Chan-Kyu Park. Predicting carbonation in early-aged cracked concrete. *Cement and Concrete Research*, 36(5):979–989, 2006.

[501] Cheng-Feng Chang and Jing-Wen Chen. The experimental investigation of concrete carbonation depth. *Cement and Concrete Research*, 36(9):1760–1767, 2006.

[502] Mostafa Seifan and Aydin Berenjian. Application of microbially induced calcium carbonate precipitation in designing bio self-healing concrete. *World Journal of Microbiology and Biotechnology*, 34(11):1–15, 2018.

[503] Huan He, Zhan-Qi Guo, Piet Stroeven, Jing Hu, and Martijn Stroeven. Computer simulation study of concrete's self-healing capacity due to unhydrated cement nuclei in interfacial transition zones. In *Proc 1st Int Conf Self-healing materials. Noordwijk aan Zee, The Netherlands*, volume 51, 2007.

[504] Huan He, Zhanqi Guo, Piet Stroeven, Martijn Stroeven, and Lambertus Johannes Sluys. Self-healing capacity of concrete-computer simulation study of unhydrated cement structure. *Image Analysis & Stereology*, 26(3):137–143, 2007.

[505] Zhong Lv and Huisu Chen. Analytical models for determining the dosage of capsules embedded in self-healing materials. *Computational materials science*, 68:81–89, 2013.

[506] Haoliang Huang and Guang Ye. Numerical studies of the effects of water capsules on self-healing efficiency and mechanical properties in cementitious materials. *Advances in Materials Science and Engineering*, 2016, 2016.

[507] Ying Yang and Marek W Urban. Self-healing polymeric materials. *Chemical Society Reviews*, 42(17):7446–7467, 2013.

[508] Jiayi Chen and Guang Ye. A lattice boltzmann single component model for simulation of the autogenous self-healing caused by further hydration in cementitious material at mesoscale. *Cement and Concrete Research*, 123:105782, 2019.

[509] Adrian Muntean. *A moving-boundary problem: modeling, analysis and simulation of concrete carbonation*. Cuvillier Verlag, 2006.

[510] Adrian Muntean, M Böhm, and J Kropp. Moving carbonation fronts in concrete: a moving-sharp-interface approach. *Chemical engineering science*, 66(3):538–547, 2011.

[511] Minling Zheng, Fawang Liu, Qingxia Liu, Kevin Burrage, and Matthew J Simpson. Numerical solution of the time fractional reaction–diffusion equation with a moving boundary. *Journal of Computational Physics*, 338:493–510, 2017.

[512] Malte A Peter, Adrian Muntean, Sebastian A Meier, and Michael Böhm. Competition of several carbonation reactions in concrete: A parametric study. *Cement and concrete research*, 38(12):1385–1393, 2008.

[513] Yangyiwei Yang, Patrick Kühn, Min Yi, Herbet Egger, and Bai-Xiang Xu. Non-isothermal phase-field modeling of heat–melt–microstructure-coupled processes during powder bed fusion. *JOM*, 72(4):1719–1733, 2020.

[514] P Sulapha, SF Wong, TH Wee, and S Swaddiwudhipong. Carbonation of concrete containing mineral admixtures. *Journal of materials in civil engineering*, 15(2):134–143, 2003.

[515] Yu Zhu, Yingzi Yang, and Yan Yao. Autogenous self-healing of engineered cementitious composites under freeze–thaw cycles. *Construction and Building Materials*, 34:522–530, 2012.

[516] Quoc Tri Phung, Norbert Maes, Diederik Jacques, Geert De Schutter, Guang Ye, and Janez Perko. Modelling the carbonation of cement pastes under a co2 pressure gradient considering both diffusive and convective transport. *Construction and Building Materials*, 114:333–351, 2016.

[517] C Allain, M Cloitre, and M Wafra. Aggregation and sedimentation in colloidal suspensions. *Physical review letters*, 74(8):1478, 1995.

[518] Peter J Lu, Emanuela Zaccarelli, Fabio Ciulla, Andrew B Schofield, Francesco Sciortino, and David A Weitz. Gelation of particles with short-range attraction. *Nature*, 453(7194):499–503, 2008.

[519] Daniel Schwen, Larry K Aagesen, John W Peterson, and Michael R Tonks. Rapid multiphase-field model development using a modular free energy based approach with automatic differentiation in moose/marmot. *Computational Materials Science*, 132:36–45, 2017.

[520] Gyula I Tóth, Tamás Pusztai, and László Gránásy. Consistent multiphase-field theory for interface driven multidomain dynamics. *Physical Review B*, 92(18):184105, 2015.

[521] Derek Gaston, Chris Newman, Glen Hansen, and Damien Lebrun-Grandie. Moose: A parallel computational framework for coupled systems of nonlinear equations. *Nuclear Engineering and Design*, 239(10):1768–1778, 2009.

[522] Hongzhi Cui, Waiching Tang, Wei Liu, Zhijun Dong, and Feng Xing. Experimental study on effects of co2 concentrations on concrete carbonation and diffusion mechanisms. *Construction and Building Materials*, 93:522–527, 2015.

[523] YH Loo, MS Chin, CT Tam, and KCG Ong. A carbonation prediction model for accelerated carbonation testing of concrete. *Magazine of Concrete Research*, 46(168):191–200, 1994.

[524] Wei Liu, Yong-Qiang Li, Lu-Ping Tang, and Zhi-Jun Dong. Xrd and 29si mas nmr study on carbonated cement paste under accelerated carbonation using different concentration of co2. *Materials Today Communications*, 19:464–470, 2019.

[525] Eva Loste, Eva Díaz-Martí, Ali Zarbakhsh, and Fiona C Meldrum. Study of calcium carbonate precipitation under a series of fatty acid langmuir monolayers using brewster angle microscopy. *Langmuir*, 19(7):2830–2837, 2003.

[526] Alejandro Fernandez-Martinez, Yandi Hu, Byeongdu Lee, Young-Shin Jun, and Glenn A Waychunas. In situ determination of interfacial energies between heterogeneously nucleated caco3 and quartz substrates: thermodynamics of co2 mineral trapping. *Environmental science & technology*, 47(1):102–109, 2013.

[527] Biqin Dong, Lve Yang, Qingyun Yuan, Yuqing Liu, Jianchao Zhang, Guohao Fang, Yanshuai Wang, Yinghuan Yan, and Feng Xing. Characterization and evaluation of the surface free energy for cementitious materials. *Construction and Building Materials*, 110:163–168, 2016.

[528] Sabine Caré and E Hervé. Application of an-phase model to the diffusion coefficient of chloride in mortar. *Transport in Porous Media*, 56(2):119–135, 2004.

[529] Ana CF Ribeiro, Marisa CF Barros, Ana SN Teles, Artur JM Valente, Victor MM Lobo, Abílio JFN Sobral, and MA Esteso. Diffusion coefficients and electrical conductivities for calcium chloride aqueous solutions at 298.15 k and 310.15 k. *Electrochimica Acta*, 54(2):192–196, 2008.

[530] Baudilio Coto, C Martos, José L Peña, Rosalía Rodríguez, and Gabriel Pastor. Effects in the solubility of caco3: Experimental study and model description. *Fluid Phase Equilibria*, 324:1–7, 2012.

[531] Neven Ukrainczyk and EAB Koenders. Representative elementary volumes for 3d modeling of mass transport in cementitious materials. *Modelling and simulation in materials science and engineering*, 22(3):035001, 2014.

[532] Yangyiwei Yang, Olav Ragnvaldsen, Yang Bai, Min Yi, and Bai-Xiang Xu. 3d non-isothermal phase-field simulation of microstructure evolution during selective laser sintering. *npj Computational Materials*, 5(1):1–12, 2019.

[533] Min Wu, Björn Johannesson, and Mette Geiker. A review: Self-healing in cementitious materials and engineered cementitious composite as a self-healing material. *Construction and Building Materials*, 28(1):571–583, 2012.

[534] Chung-Chan Hung, Yen-Fang Su, and Hsuan-Hui Hung. Impact of natural weathering on medium-term self-healing performance of fiber reinforced cementitious composites with intrinsic crack-width control capability. *Cement and Concrete Composites*, 80:200–209, 2017.

[535] Anna V Saetta and Renato V Vitaliani. Experimental investigation and numerical modeling of carbonation process in reinforced concrete structures: Part i: Theoretical formulation. *Cement and concrete research*, 34(4):571–579, 2004.

[536] Andreas Ludwig. The interface response-functions in multi-componental alloy solidification. *Physica D: Nonlinear Phenomena*, 124(1-3):271–284, 1998.

[537] M J Aziz and WJ Boettinger. On the transition from short-range diffusion-limited to collision-limited growth in alloy solidification. *Acta metallurgica et materialia*, 42(2):527–537, 1994.